Investigating the effect of materials processing on ZnO nanorod properties and device performance

Sabina Hatch

Degree of Doctor of Philosophy

School of Engineering and Material Science

Supervisor: Dr Steve Dunn

1st May 2013

Abstract

This project explores the effect of materials processing on the optical, morphological, and electrical properties of ZnO nanorods synthesised using the low-temperature (90˚C) aqueous chemical technique. A highly-alkaline (pH 11) growth solution fabricated nanorods that exhibit morphological sensitivity to the anneal atmosphere used. This was attributed to unreacted precursors trapped throughout the nanorod bulk and near the surface. A significant increase in the c-axis peak intensity post-annealing and evidence of nitrogen-doping in all annealed nanorods, confirmed the precursors were present prior to the annealing process. In addition, intense green photoluminescence was observed under UV excitation and was shown to be dependent on the anneal atmosphere. The origin of this emission was related to zinc vacancy defects that were energetically favoured during the oxygen-rich synthesis and anneal conditions according to first principle calculations.

To better study the electrical properties of the ZnO nanorods they were incorporated into p-n heterostructures using p-type CuSCN. An alternative spray-coating method was developed for depositing CuSCN that was a significant improvement over previous methods as demonstrated by the high hole mobility 70 cm^2/V.s. The current popularity of conductive polymers led to the comparison of hybrid inorganic-organic (ZnO-PEDOT:PSS) and purely inorganic (ZnO-CuSCN) devices. These were tested as UV photodetectors and differences in device structure were shown to have a significant impact on the device response time and responsivity. A rectification ratio of 21500 at ±3 V was achieved for these ZnO-CuSCN devices.

The inorganic ZnO-CuSCN device exhibited photovoltaic behaviour at zero-bias, which highlighted it as a suitable choice for self-powered UV photodetection. The effect of processing on the photodetector performance was investigated for two sets of nanorods; pH 6 and pH 11. Consequently, a maximum photocurrent response of 30 µA (for 6 mW cm^{-2} irradiance) was achieved for nitrogen-annealed pH 11-nanorods with a rise time of 25 ns. The high response was assigned to fewer zinc vacancies acting as electron trap states and the introduction of N-related donor defects.

Acknowledgements

Firstly, my sincere gratitude goes to my supervisor, Dr Steve Dunn, for giving me this opportunity, and for showing me that I must consider all aspects of a theory if I am to give well-structured argument.

Secondly, my appreciation goes to Dr Joe Briscoe, for listening to my ideas and concerns, and providing me with the training and knowledge that formed the foundation of my PhD.

Thanks to the staff at the B18 Diamond Light Source for setting up and calibrating the equipment, and the Renishaw group for performing additional Raman scans for analysis.

Without access to the equipment provided by Prof William Gillin and Dr Andrei Sapelkin, I would not have been able to conduct a significant portion of my characterisation and analysis. My thanks go to them for their training, understanding, and patience.

I would also like to thank the following staff; Dr Zofia Luklinska, Dr Rory Wilson, Jim Kirkland, Jun Ma, Danny Neighbour, Chris Mole, Dennis Ife, Ken Scott, and Chris Straw for their assistance and support. Their patience and swift response to my requests ensured my project was always moving forward

Thanks to the EPRSC for funding this research project.

Finally, thanks to my mother for the many hours she pushed me, supported me and prayed for me during my times of difficulty. I would not have achieved so much without her encouragement and belief.

Disseminations

Journal papers

- "Self-powered ZnO-nanorod/CuSCN UV photodetector exhibiting rapid nanosecond response". S.M. Hatch, J. Briscoe, and S. Dunn, Advanced Materials, **2013**, *25*, 867–871.
- "Improved CuSCN-ZnO diode performance with spray deposited CuSCN". S.M. Hatch, J. Briscoe, and S. Dunn, Thin Solid Films, **2013**, *531*, 404-407.
- "Enhanced quantum dot deposition on ZnO nanorods for photovoltaics through layer-by-layer processing". J. Briscoe, D. E. Gallardo, S.M. Hatch, V. Lesnyak, N. Gaponik, and S. Dunn, Journal of Materials Chemistry, **2011**, *21*, 2517-2523.
- "Influence of anneal atmosphere on ZnO-nanorod properties and self-powered photodetector performance". Journal of Applied Physics, April 2013 Accepted

Submitted

- "Extended X-ray absorption fine structure (EXAFS) analysis of ZnO-nanorods using optically-detected XEOL". Journal of Applied Physics, April 2013

Conference proceedings

- "ZnO Nanostructured diodes: The influence of synthesis conditions and p-type material on device performance". S.M. Hatch, and S. Dunn, MRS Proceedings, **2012**, *1439*.

Presentations

- Materials Research Society, spring conference 2012, San Francisco, USA - Oral communication: "ZnO Nanostructured diodes: The influence of synthesis conditions and p-type material on device performance".
- Technology World 2010 Excel Centre, London, UK - Poster communication "Influence of hole transport layer of ZnO-nanorod diode performance".

Table of Contents

List of Figures

List of Tables

1 Introduction

1.1 Background

Practical developments in areas involving electronics, mechanics, and architecture among others, arise from extensive research conducted in the field of material science. ‘Nanotechnology’ has become a well-known term outside the field of material science due to its incorporation in a wide-range of every-day applications such as mobile/smart phones, self-cleaning windows/fabrics, cosmetics and light-weight sports equipment. The list continues with applications that are less well-known to the general public, for example: drug delivery, tissue engineering, filtration, construction, memory storage, quantum computing, catalysis, sensors and energy-harvesting devices. Materials on a nano-scale possess a significantly increased surface-to-volume ratio that leads to additional properties unseen on the bulk-scale. This includes quantum confinement in semiconductors, surface plasmon resonance in certain metallic particles, and superparamagnetism in magnetic materials.

This thesis adopts the benefits provided by nano-scale semiconductors to enhance the performance of optoelectronic devices, specifically photodetectors. Photodetectors are used in biological and chemical analysis, optical communications, astronomical studies and flame detection. The demand for nanoscale devices in these fields requires the removal of the bulky power sources used to operate them. A solution to this would be to use the photovoltaic effect at zero applied bias to obtain a photocurrent response. The challenge was therefore finding materials capable of generating a significant photovoltage at zero-bias. Furthermore, the photodetector would benefit from materials that are chemically robust, possess radiation hardness, and exhibit long-term stability. For UV photodetectors wide-bandgap materials are often used as they provide a natural filter against lower energy photons, which allows them to operate at room temperature. Zinc oxide (ZnO) is a wide-bandgap n-type semiconductor suitable for UV photodetection. It exhibits good photoconductivity under UV illumination, which is enhanced by the nanostructured morphology and the photo-desorption of oxygen ions. However, operating at zero-bias relies solely on the induced photovoltage and the drift of charge carriers to lower field potentials. The weak drift current does not aid in charge separation, and so overcoming charge carrier recombination within ZnO is an important factor. Flexible photodetectors would be an added benefit and so the ability to synthesise

nanostructures at low-temperatures on is another advantage ZnO has over its competitors. The bottom-up growth that occurs with low-temperature processing often means defects are unavoidable. Although ZnO has been investigated extensively for more than a century, fundamental questions remain surrounding the defects that give rise to unintentional n-type behaviour and deep-level photoluminescence. The morphological, optical, and conductive properties influenced by the incorporated defects may serve to enhance or diminish the device performance. The impact of surface-related defects on performance is especially important when considering the high surface-to-volume ratio of nanostructures.

1.2 Aims and objectives

Identification of defects present in the ZnO lattice was one of the major challenges faced during this project. Although methods exists to identify the presence of elements near the surface (e.g. X-ray photoelectron spectroscopy, Raman, Fourier Transform Infra-red spectroscopy), as of yet there is no direct method to definitively identify the defect present in the lattice. Consequently, defect analysis often involves theoretical first-principle calculations of defect formation energies with respect to Fermi level constraints. This is related to indirect methods such as photoluminescence, positron annihilation spectroscopy, and extended x-ray absorption fine structure (EXAFS) analysis to infer likely defect sources.

High-quality EXAFS data has not previously been obtained in optically-detected mode (OM), which selectively collects structural information surrounding the emission source. Consequently, it has not previously been used to identify the atomic structure or bond lengths in the ZnO lattice. The challenge of obtaining high-quality data in OM relies on the material possessing intense visible spectral emission. In addition, as a surface sensitive technique, the EXAFS intensity could be improved by analysing nanostructured morphology.

In this thesis ZnO nanorods were used as the n-type semiconductor and the effect of aqueous chemical processing on the nanorod properties was investigated. To complete the inorganic n-p heterostructure, p-type semiconductor copper (I) thiocyanate (CuSCN) was used. The main difficulty faced when using this material was that of deposition. The electrical failure of initial devices was caused by shorts between the top and bottom electrodes. This was due to cracks forming in the CuSCN layer post-deposition and is a common occurrence with this material. Hence, it was important to establish an alternative method to deposit CuSCN that would improve the p-type layer.

Hybrid devices that combine inorganic and organic semiconductors have been used for optoelectronic, piezoelectric, and memory writing devices. Here, PEDOT:PSS will be used to create a hybrid heterostructure with ZnO and tested as a photodetector. As a polymer, PEDOT:PSS will be well suited to flexible devices, but its longevity and stability is comparably less than its inorganic counterparts.

Spectral sensitivity, responsivity, and response times are all critical parameters used to analyse photodetector performance. It is typically observed that as one parameter is improved, another is negatively affected due to unwarranted side-effects. In particular the recovery time of ZnO-based photodetectors is influenced by the adsorbed oxygen; and is magnified by the high-surface area of the nanorods. Consequently, the challenge was to improve the above parameters whilst minimising negative side-effects.

The aims of the thesis are as follows:

- Investigate the influence processing and thermal annealing on the morphological, optical, and conductive properties of ZnO nanorods.
- Perform EXAFS analysis on ZnO nanorods in attempt to obtain high-quality spectra in optically-detected mode for defect analysis.
- Develop an alternative method for the deposition of CuSCN p-type material onto nanostructured surfaces.
- Compare the performance of purely-inorganic and hybrid (inorganic-organic) ZnO-based photodiodes using p-type CuSCN and PEDOT:PSS.
- Test the ZnO-CuSCN photodiodes as self-powered photodetectors at zero-applied bias, and investigate how ZnO defects incorporated during low-temperature synthesis can impact the device performance.

1.3 Thesis structure

Chapter 2 of the thesis provides a detailed background of the materials used during this project as well as the recent developments in photodetector fabrication. The experimental section in Chapter 3 describes the aqueous chemical synthesis of ZnO nanorods, deposition of p-type hole collectors, and device completion for electrical testing. In addition, the chapter provides a detailed account of the characterisation techniques used to analyse the morphology, crystallography, optical properties, and electrical characteristics. Chapter 4 is the first of three experimental chapters, and begins the investigation with the processing of

ZnO nanorods. The aqueous synthesis procedure was primarily examined for two different growth mediums: a weakly-acidic (pH 6) and a high-alkali (pH 11) solution. Post-synthesis, the pH 11 grown nanorods were annealed in various atmospheres. The effect of annealing on the nanorod morphology, crystallography and optical properties is presented and the analysis focuses on the defects present. Chapter 5 is the second experimental chapter and begins with the development of CuSCN deposition. It continues with a comparison between the fully-inorganic (ZnO-CuSCN) and the hybrid inorganic-organic (ZnO-PEDOT:PSS) devices. The final experimental chapter, Chapter 6, applies the knowledge gained from the previous chapters to fabricate self-powered ZnO-CuSCN photodetectors. The pH 6 and pH 11 grown nanorods are used to demonstrate the effect of processing on device performance using photovoltage, current vs. time, responsivity, and photosensitivity measurements. The concluding Chapter 7 summaries the major accomplishments achieved over the three experimental chapters. Furthermore it highlights areas that would benefit from further work and proposes additional experimental procedures that would improve or support the reported findings.

2 Literature Review

2.1 Zinc Oxide (ZnO)

2.1.1 Background and properties

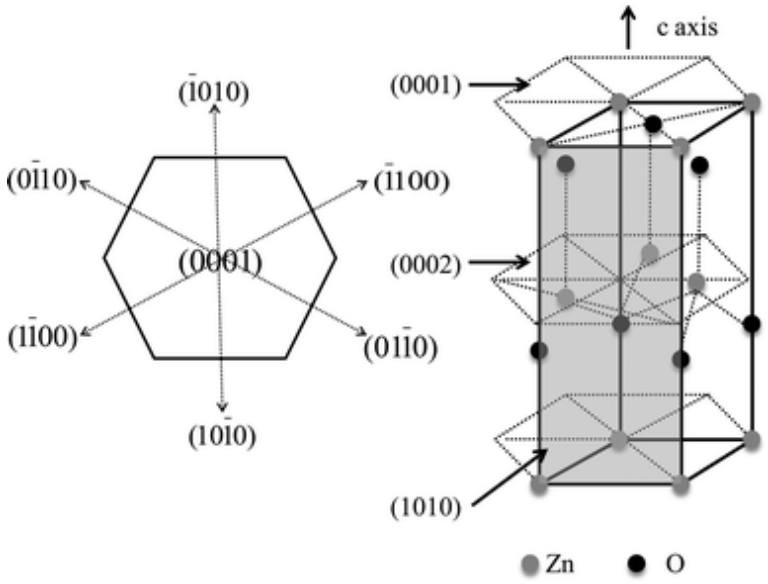

Figure 2.1 The wurtzite crystal structure of ZnO, ref. [1]

ZnO typically forms a wide band-gap n-type semiconductor, which commonly adopts a wurtzite structure. The unit cell of ZnO is indicated by the bold lines in Figure 2.1. Four oxygen atoms have a tetrahedral co-ordination to a Zn atom and the bonding between atoms is considered to be ionic. The wurtzite structure results in opposing polar surfaces, i.e. Zn^{2+} on the (0001) plane and O^{2-} on the $(000\bar{1})$ plane. This asymmetric structure assists in forming temporary polarisation of the surface under stressed conditions, which makes it suitable for piezoelectric applications. The ZnO surface is hydrophilic and adsorbs water from the atmosphere as well as oxygen. Photo-desorption of oxygen molecules from the surface contribute to the photoconductive properties that will be discussed later in this section.

ZnO has a high exciton binding energy of 60 meV at room temperature (RT) and optical transparency to visible wavelengths. This makes it suitable for exciton-based devices operating at RT, such as: solar cells [2], UV laser diodes [3–5], photodetectors [6–8],

optical switches [9], and light emitting diodes [10–12]. ZnO is non-toxic, chemically stable and a relatively abundant material, which give the advantages of being environmentally friendly and inexpensive. Lastly, ZnO is a popular semiconducting material because of the numerous techniques that can be applied to synthesise ZnO, most of which can be used to form nanostructured morphologies.

Nanostructures provide a high-surface area that improves photon capture through the increased quantity of dye that can be adsorbed onto the surface and additional photon scattering. Gas sensors also benefit from the high surface areas due to the significantly increased surface interactions that take place [13–16]. This permits the gas sensors to operate at RT, whereas thin film ZnO typically requires elevated temperatures [17]. Nanowires/nanorods can provide a direct pathway for charge carriers to the contact electrode, thus assisting in carrier mobility and charge separation at the junction/interface.

These diverse and numerous properties demonstrate why thousands of publications exist on ZnO and why hundreds more continue to be published each year. This short review on ZnO does not aim to cover the entire scope but provides a concise overview that focuses on ZnO properties relevant to this thesis.

2.1.2 Growth techniques

One advantage of ZnO over similar semiconductors such as GaN is the variety of techniques available to synthesise nanostructures. This section will focus on techniques used to produce nanostructures rather than thin films. The surface of a semiconducting material is critical in establishing certain characteristics, such as energy band-bending at the surface. This is dependent on dangling-bonds formed at the crystal lattice edge that may lead to surface defects, such as adsorption of oxygen or atmospheric water molecules in the case of ZnO. Due to the high surface-to-volume ratio provided by the nanostructure morphology, ZnO properties are strongly influenced by the surface. Growth techniques that use high temperatures, high pressures or vacuums, typically produce fewer defects in the ZnO lattice. However, these extreme conditions come with drawbacks: scalability limitations, substrate restrictions, and where metal catalysts are used to facilitate growth it may lead to unintentional impurity doping. The following techniques are some of the most well-known methods of ZnO-nanostructure production.

2.1.2.1 Vapour-phase growth

2.1.2.1.1 Chemical vapour deposition (CVD)

This is one of the most common and earliest reported routes for creating nanowires, nanobelts, nanosprings and nanorings. Zinc and oxygen vapour is guided over a substrate surface that has been coated with Au nanoparticles to act as a seed [4,18]. Here the vapour-liquid-solid (VLS) method typically applies, whereby the Au particles become enriched with the metal vapour until it is saturated and begins to grow outward from the catalyst forming ZnO [19]. In some cases, the gold nanoparticle remains on the nanowire tip [20] and in others, gold was detected at the nanowire interface [21]. This leads to unintentional defect levels in the energy bandgap of the nanowire. Temperatures up to 925˚C were used to deposit a 1:1 ZnO and carbon mixture onto the substrate surface under an argon atmosphere. The elevated temperature decomposes the water and carbon oxides while zinc vapour diffuses into the gold nanoparticle forming a eutectic material. This eutectic particle behaves as a liquid phase epitaxy that controls the position and size of the nanowires [22]. Large scale arrays have been produced using this method [23,24]. Growth parameters were shown to be influenced by the oxygen partial pressure, chamber pressure [25,26] and seed layer thickness of the catalyst [18].

2.1.2.1.2 Metal Organic Chemical vapour deposition (MOCVD)

MOCVD of ZnO nanowires is conducted in a similar manner to CVD, but removes the need of a metal catalyst. Instead a metal-organic precursor is used containing the required elements, such as diethyl zinc and oxygen with argon as a carrier gas [27]. This is a significant advantage for device applications as metal impurities are no longer left behind in, or on, the nanowires. The low reaction temperatures of 400-500˚C opened the gateway for various substrates that were previously unsuited to the synthesis such as GaAs [28] and Si/fused silica [29]. Dimensions of the nanowires can be controlled by changing the growth time but were also affected by the temperature and pressure. TEM, EDX, and PL analysis have shown nanowires grown via MOCVD produce almost perfect defect-free single crystals [30,31].

2.1.2.1.3 Pulsed-laser deposition (PLD)

This technique employs a laser pulse to form a plasma plume of the base material (Zn) in the gas-phase to create ZnO nanowires. For ZnO, oxygen serves as a residual reactor gas.

This requires high pressures of up to 5 Torr and temperatures of ~700˚C [32]. Nanowire diameters are controlled by varying the distance between the target and the source [33]. This technique has the advantage of conducting surface analysis during growth. However, a disadvantage of the high energy particles that occur in the plasma plume may affect the surface morphology and introduce defects.

2.1.2.1.4 Thermal evaporation

Thermal evaporation of ZnO powders mixed with graphite have been used to fabricate various nanostructures [34,35]. Temperature was a critical parameter in dictating the various nanostructure morphologies that could be fabricated and would range from 500-1250˚C. Nanocombs for example were grown using this method and the growth time was shown to influence the dimensions of the combs and the shape of the nanowire 'teeth' [36].

2.1.2.2 Liquid-phase growth

2.1.2.2.1 Electrodeposition

This technique can be performed at low temperatures (< 90˚C) to fabricate ZnO columns. Varying the electrodeposition parameters such as current density, deposition time, and bath temperature are shown to dictate the morphology of the nanowires [37,38]. The technique involves using a three-electrode reactor operating at ~80˚C with solutions typically consisting of 5 mM $ZnCl_2$ and 0.1 M KCl [39,40]. A potential of -1 V versus saturated calomel electrode was applied while oxygen is bubbled through the solution. This produces a thin film after 20 minutes. As the concentration of Zn^{2+} ions decreases, the nanorods begin to form from the thin film. The band-gap of electrodeposited ZnO was found to increase with increasing potential across the electrodes; however, this was secondary to the influence of grain size, lattice strain, and defect states [41]. The substrate was also shown to influence the nucleation of the nanorods and this was attributed to the presence of native surface oxide that would assist growth [42]. Electrodeposition provides a solution process that operates at low temperatures with atmospheric pressures, and as such it has the potential of epitaxial growth for mass production.

2.1.2.2.2 Chemical bath deposition (CBD)

Aqueous chemical growth was first reported in 1990 by Vergés *et al*.[43] This was later modified by Vayssieres et al. to grow nanorods on TCO-coated glass and Si substrates [44]. This method requires a pre-deposited seed layer to initiate ZnO growth. The seed layer, as with the catalyst in CVD, can influence the size, density and orientation of the nanorods [45,46]. Chemical bath depositions use a zinc salt (e.g $Zn(NO_3)_2$, $ZnCl_2$) with an alkaline solution (e.g. hexamethylenetetramine [HMT/$(CH_2)_6N_4$], NaOH or NH_3(aq)) heated to temperatures <100˚C at atmospheric pressures.

The chemical reactions for ZnO growth are typically given as follows [47]:

$$(CH_2)_6N_4 + 6H_2O \leftrightarrow 6HCHO + 4NH_3 \quad (1)$$

$$NH_3 + H_2O \leftrightarrow NH_4^+ + OH^- \quad (2)$$

$$2OH^- + Zn^{2+} \rightarrow ZnO(s) + H_2O \quad (3)$$

$$\mathrm{Zn(NH_3)_4^{2+} + 2OH^- \leftrightarrow ZnO + 4NH_3 + H_2O} \quad (4)$$

Primarily, HMT decomposes into formaldehyde and ammonia and acts as a pH buffer (eq.1). Ammonia supplies hydroxyl ions (eq.2), which react with free Zn^{2+} cations to form ZnO (eq. 3) [48], or alternatively forms a Zn(II)-amine complex (eq. 4). HMT was also reported to act as a capping agent that preferentially attaches to non-polar ZnO faces [49,50]. Thus promoting growth in the (0001) c-axis direction by restricting the availability of growth sites on the non-polar faces [51]. It has since been established using Fourier transform infrared (FTIR) spectroscopy *in situ* with the growth, that HMT does not act as a capping agent [52].

Strom *et al*. [53] found the rate at which HMT decomposes into its constituents decreases with increasing pH. Above pH 7.4 no HMT degradation was detected after 6 h at 35˚C. Consequently, for aqueous solutions with pH > 7.4 an elevated temperature is required in order to degrade HMT into its constituents. This demonstrates the critical role temperature plays in the production of hydroxyl ions and the rate of ZnO growth.

To increase the nanorod length the solutions were refreshed in order to replenish the precursors that reacted homogenously and precipitated out. Consequently, CBD can take up to 6 h with three repeat synthesis to grow nanorods of 5.5 µm in length [54]. A number

of factors have been investigated in attempt to speed up the process or manipulate the ZnO properties. Precursor concentration, pH, doping, temperature, capping agents, and synthesis duration have all demonstrated a strong influence on ZnO properties and morphology [55–59]. The polar wurtzite-structure of ZnO means that the semiconductor is highly anisotropic and gives rise to higher surface energy at the positive polar surface (0001). The rate of reactions for the remaining planes is given as: $(\bar{1}01\bar{1}) > (\bar{1}010) > (\bar{1}011) > (000\bar{1})$.

The term, *hydrothermal growth* has been applied to these conditions; however this term should technically only refer to situations where additional pressure is applied to the solution. The CBD fabrication method provides inexpensive, environmentally friendly growth at low-temperatures (<100˚C). Consequently, as-grown nanorods typically exhibit weak UV photoluminescence and prominent defect concentrations under UV excitation at RT [60–63].

2.1.2.2.3 Rapid microwave synthesis

Microwave heating has been tested as a replacement for the conventional oven used in CBD synthesis methods and was first reported in 1986 by Gedye *et al*.[64] Since then, its usage has increased to fabricate ZnO nanostructures with aqueous solutions consisting of the same precursors used in CBD [65,66]. When the precursors are exhausted the solution is refreshed so that nanorod growth may continue. Ghafoori-far *et al.* [67] recently showed that by increasing the pH with NH_3 and adding a capping agent (polyethylenimine) to restrict homogeneous growth, they obtained nanorods 6 μm in length after 12 minutes at 850 W applied power . Although this may speed up the ZnO growth significantly, it is not an easily scalable process.

2.1.3 ZnO native defects and impurities

Synthesising high-quality single-crystal ZnO with no impurities or native defects presents a significant challenge. This is because impurities are extremely difficult to exclude from most synthesis environments, and when the formation energies of native defects are favoured their presence is unavoidable. The formation energies of native defects are dictated by the environmental conditions during growth and post-processing, often this is expressed as oxygen-rich or zinc-rich conditions (see Figure 2.2).

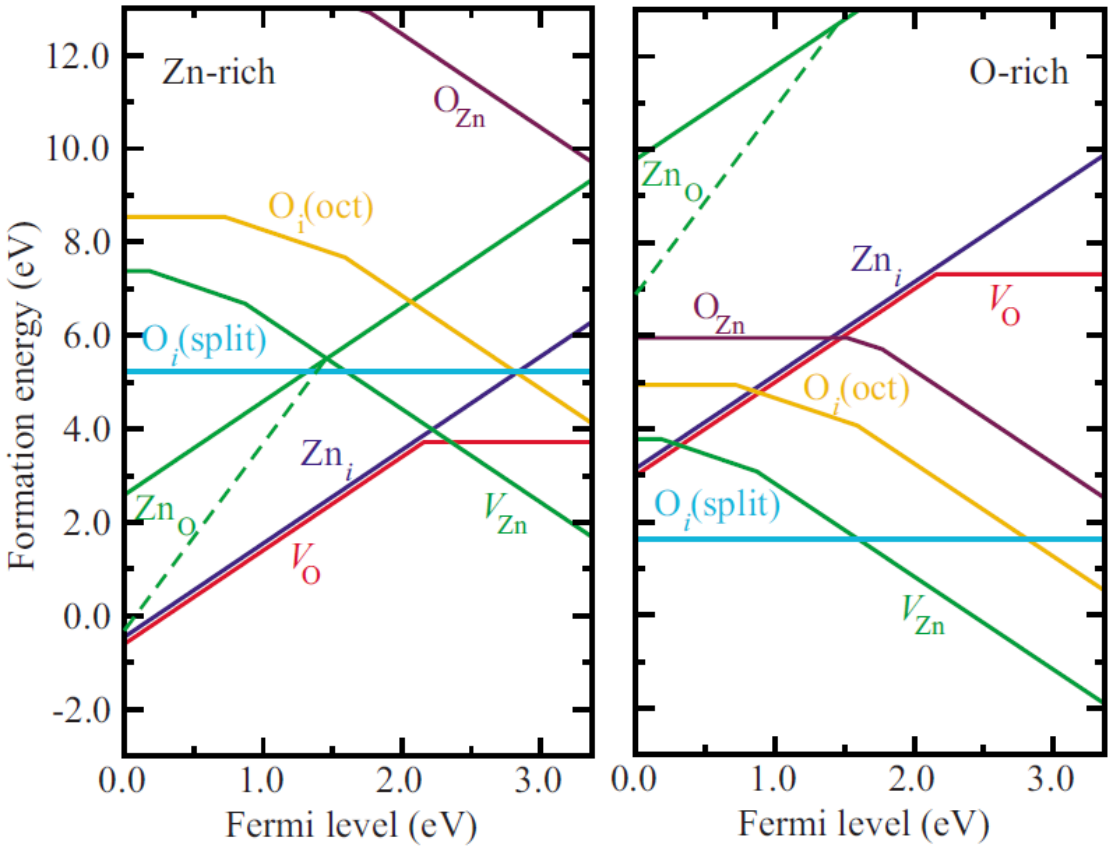

Figure 2.2 Formation energies calculated by Van de Walle et al. as a function of Fermi-level position for native point defects in ZnO for Zn-rich and O-rich conditions. The zero of Fermi-level corresponds to the valence band maximum. Only segments corresponding to the lowest energy states are shown. Kinks in the curves indicate transitions between different charge states. Ref. [68]

The low formation energies of native defects in ZnO contribute to the lack of control over their incorporation. Consequently, there is a need to understand how each defect influences the various physical, optical and electronic properties of ZnO. The major challenge this presents is defect identification, and establishing where the defect charge state is situated within the energy bandgap. This is often inferred from experimental techniques such as: electron paramagnetic resonance (EPR) [69–71], cathode luminescence (CL) [72,73], deep-level transient spectroscopy [74–76], or positron annihilation spectroscopy (PAS) [77–80]. Alternatively, theoretical first-principle calculations use density-functional theory (DFT) in the local-density approximation (LDA) to find solutions to the Schrodinger equation. The lack of systematic corrections for deficiencies in the LDA or generalised gradient approximations (GGA) to DFT, and spurious energy contributions due to the finite-supercell formalism, explain why a large spread in the predictions for ZnO exist [81].

The concentration of defects in the ZnO sample can be calculated by:

$$C_d = N_{sites} e^{-\Delta G_f / k_B T},$$

where N_{sites} is the number of sites the defect can occur, ΔG_f is the difference in Gibbs free energy and is expressed as:

$$\Delta G_f = \Delta E_f - T\Delta S_f + P\Delta V_f .$$

This is the total change in formation energy minus the vibrational entropy plus the change in lattice volume. The main contribution is the formation energy (as the last two terms are orders of magnitude smaller) and is defined by the external chemical potential for Zn and O, and the Fermi energy (if the defect is charged):

$$\Delta E_f = E(N_{Zn}, N_O) - N_{Zn}\mu_{Zn} - N_O\mu_O + q\varepsilon_F$$

The chemical potentials of the O and Zn determine the off stoichiometry of the system and depend on the partial pressure/growth conditions [82]. This explains why it is necessary to consider two systems for formation energies: O-rich and Zn-rich, when determining the most favourable defect states.

The following section focuses on reviewing ZnO native defects and extrinsic impurities that are relevant to this thesis.

2.1.3.1 Native defects

2.1.3.1.1 Oxygen vacancies (V_O)

For many years it was believed that the V_O was the source of the intrinsic n-type characteristics of ZnO. It has since been established through first-principle calculations that V_O are in fact deep level donors with the ε(0/2+) level situated 0.5-0.8 eV above the VBM [83–85]. In p-type conditions they are predicted to form readily in the V_O^{2+} state and so pose a particular challenge in the formation of *p*-type ZnO due to their role as compensating centers [86]. For n-type conditions the V_O^0 defect state is most energetically stable, but it has high formation energy for O-rich conditions so it is unlikely to form even under high temperatures. The consensus is that V_O^+ is an unstable charge state and so gives rise to a negative-U centre for the formation energy vs. Fermi-level plot [87]. This means that only the ε(0/2+) V_O transition state is likely to exist in ZnO.

2.1.3.1.2 Zinc vacancies (V_{Zn})

The formation energy of acceptor-type defects is shown to decrease with increasing Fermi level (see Figure 2.2). This allows V_{Zn}^{2-} to form easily in n-type materials but becomes increasingly scarce in p-type materials as the formation energy increases rapidly for both O and Zn-rich conditions. The transition levels ε(0/1-) and ε(1-/2-) for V_{Zn} are reported as 0.1-0.2 and 0.9-1.2 eV above the VBM, respectively [68,82]. In the same article Van de Walle *et al*. predicts the migration barrier of V_{Zn} to be 1.4 eV, which suggest the defects will be mobile above ~250˚C. Various experimental techniques have been used to link green photoluminescence that is often observed in ZnO with V_{Zn}. The controversy surrounding this topic and its relevance to this thesis requires a detailed review on the photoluminescence properties of ZnO; this will be given in Section 2.1.4.1.

2.1.3.1.3 Zinc interstitials (Zn_i)

Zn_i have high formation energies in n-type ZnO and a very low migration barrier of 0.57 eV, which implies Zn_i are highly mobile even at RT [88]. First-principle calculations show that the Zn_i defect introduces two electrons to the conduction-band states, which stabilizes the Zn_i^{2+} charge state and results in Zn_i always acting as a shallow donor [68]. As such it was previously thought Zn_i were responsible for n-type behaviour in ZnO [84,86], however the high formation energies and instability at RT make it an unlikely candidate.

2.1.3.2 Extrinsic impurities

2.1.3.2.1 Hydrogen

Hydrogen impurities are extremely difficult to prevent during the synthesis of ZnO due to their small particle size and ubiquitous nature. This allows hydrogen to easily diffuse into low-density materials and its strong bond with oxygen serves to enhance its incorporation into the ZnO lattice during growth. The first major developments with regard to hydrogen-doping in ZnO was reported in the 1950s [89,90] and picked up again more recently by Van de Walle who found only H^+ is the stable charge state in ZnO, and so exclusively acts as a donor [91,92]. This behaviour was linked to the strong O-H bond that drives the formation energy of H^+ down in ZnO (see Figure 2.3).

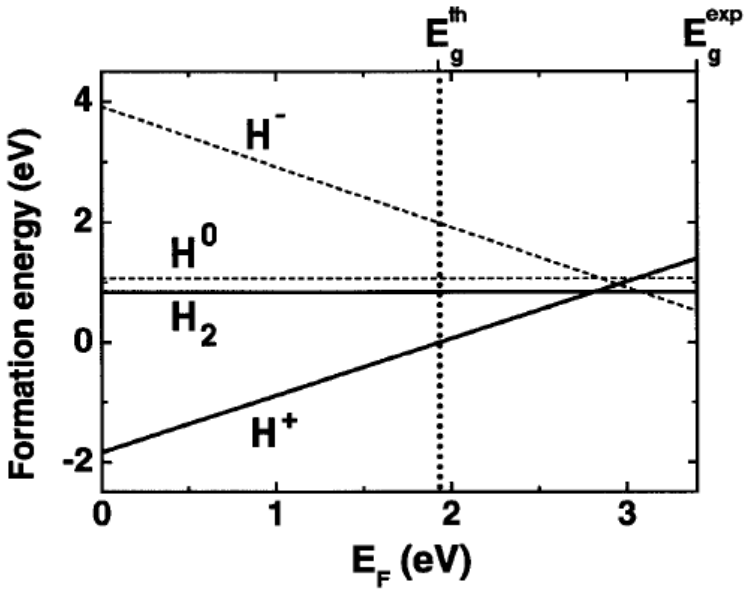

Figure 2.3 Formation energies of interstitial hydrogen in ZnO, as a function of Fermi level, obtained from DFT-LDA calculations and referenced to the energy of a free H_2 molecule. (See ref. [91])

The often observed n-type conductivity of ZnO has been attributed to the formation of hydrogen substituted on oxygen sites (H_O) equally bonded to the four 4s-dangling bonds of Zn that act as shallow donors [93]. The n-type conductivity was shown to have a relation to the oxygen partial pressure during annealing [94] and so was previously thought that oxygen vacancies (V_O) were the source of n-type conductivity. The formation energy of the H_O is dependent on the oxygen partial pressure, which determines the concentration and was shown to affect the conductivity of ZnO by several orders of magnitude [95,96]. Hence, it is now believed that hydrogen-doping plays the major role in dictating the n-type behaviour of ZnO.

Hydrogen interstitials (H_i) are unstable at high temperatures, favouring H_O as the dominant species in annealed samples [97]. These findings were supported by Hall Effect measurements, which revealed n-type carrier concentration and conductivity of ZnO films decreased as the annealing temperature increased. Resistivity, ρ, of 0.73 Ωcm and electron carrier concentration (n) of 6.66 x 10^{17} cm^{-3} was recorded for the seed layer (pH 8), ρ increased to 62.70 Ωcm and n decreased to 1.10 x 10^{16} cm^{-3} after being annealed at 700˚C. The ZnO film grown at pH 10.9 had n = 1.79 x 10^{19} cm^{-3} and very low ρ of 0.025 Ωcm [98].

Zhang *et al*. used Time of Flight Secondary Ion Mass Spectrometry (TOF-SIMS) to bombard the surface of ZnO films with particles to reveal that O-H species are not only a surface adsorbed species but are present in the lattice throughout the film thickness. This technique was also used to investigate influence of pH on concentration of H incorporated in the film; a 66% reduction of H incorporation was reported as the pH decreased from 10.9 to 8 [98].

Thermal stability of hydrogen shallow donors in ZnO was investigated by Shi *et al*.[99] and shown to follow two stages; firstly, an 80% reduction of free carriers near 150˚C, and secondly, the remaining 20% eliminated around 500˚C. The first stage was linked to the removal of shallow donors related to O-H bonds. This was evidenced by IR-absorption data that showed O-H related peak intensities at local vibrational mode (LVM) lines 3611 cm^{-1} and 3326 cm^{-1} rapidly decrease at 150˚C. Upon annealing at 150˚C, it was predicted that the hydrogen interstitials are not removed from the sample, but diffuse to form H_2 defects. These act as an electrically inactive species that accounts for the decrease in carrier concentration at this stage. As the temperature nears 400˚C, dissociation of H_2 occurs, which allows liberated hydrogen to once again form the electrically active O-H species. However, prolonged heating or increased anneal temperatures completely diffuses the liberated hydrogen out of the sample. Therefore only by quenching the sample at 400˚C will the O-H defects be stabilised. The second stage of elimination above 500˚C was assigned to the more thermally stable H-species (H_O) associated with a bound-exciton luminescence line known as I_4 [99–101]. Finally, it should be noted that O-H species are unstable at room temperature, as shown by an exponential decrease in both carrier concentration and IR absorbance peak area over a period of weeks [96].

2.1.3.2.2 Nitrogen

Nitrogen-doping (N-doping) of ZnO has been investigated as a possible method for converting n-type ZnO to p-type by the introduction of shallow acceptor states [103,104]. However, N-doping can exist in many forms, these are determined by the N-source (NH_3, N_2O or N_2 plasma) and the technique used. Numerous techniques have been reported for N-doping such as: molecular beam epitaxy (MBE) [105], radio frequency (RF) magnetron sputtering [106,107], solution processing [103,108,109], spray pyrolysis [110], annealing in nitrogen [111] and N^+ ion implantation [112,113]. Although these articles report p-type

behaviour of ZnO, there remains a lack of evidence of electrically tested p-type ZnO devices.

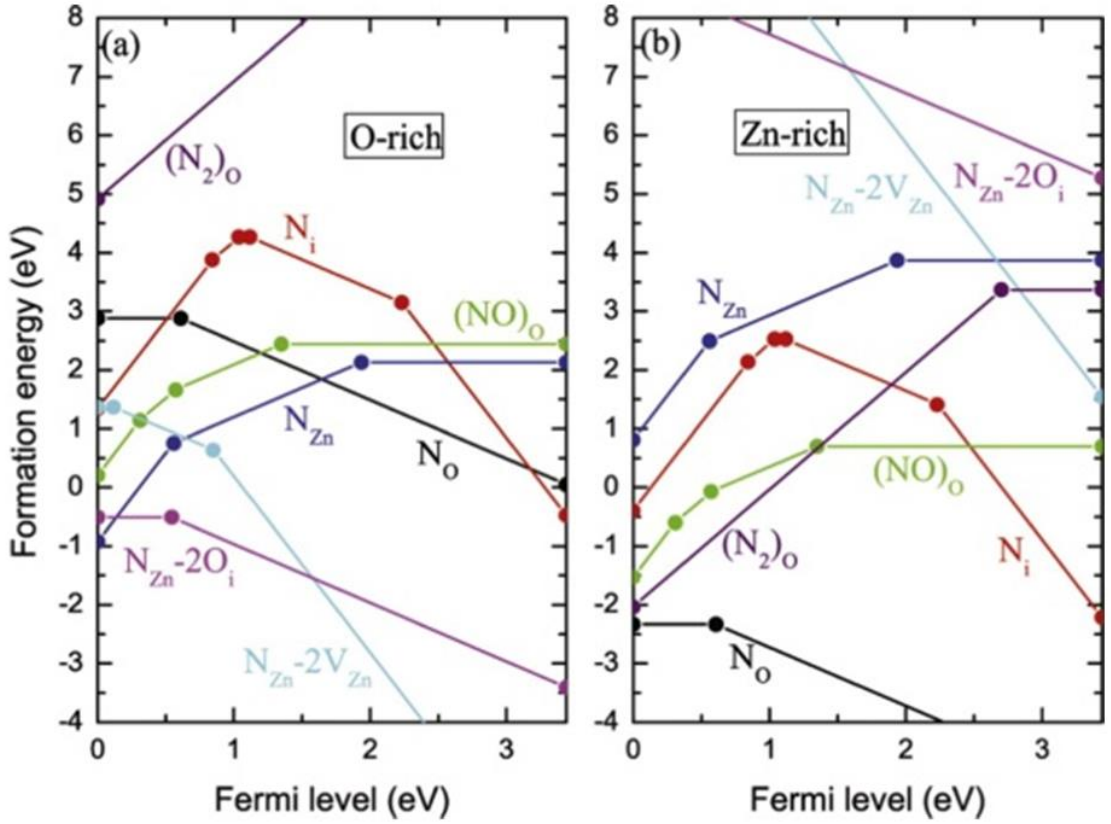

Figure 2.4 Defect formation energies in (a) O-rich and (b) Zn-rich conditions when using N_2O as the nitrogen source. The kinks in the plot indicate thermal transition levels, ref. [114].

This lack of evidence of p-type behaviour from N-doping has been attributed to the compensation mechanisms from other N-defect states [114,115]. Of the many forms of N-doping: N_O, N_O^-, $(N_2)_O^{2+}$, $(N_O - V_O)^+$, $(N_O - Zn_i)^+$, $(N_O - Zn_O)^+$, $(N_O - O_i)^+$ and $[N_O - (N_2)_O]^+$, only N_O^- is an acceptor, while the others are donors [116]. Nitrogen interstitials (N_i) behaves as an amphoteric impurity such that in p-type ZnO it acts as a donor and n-type ZnO it acts as an acceptor, always counteracting the prevailing conductivity [114]. To emphasise this point, although Iwata et al. [105] detected high concentrations of N (~10^{19}) the ZnO exhibited n-type conductivity. The defect formation energies of N-defects in ZnO are shown in Figure 2.4 for O-rich and Zn-rich conditions.

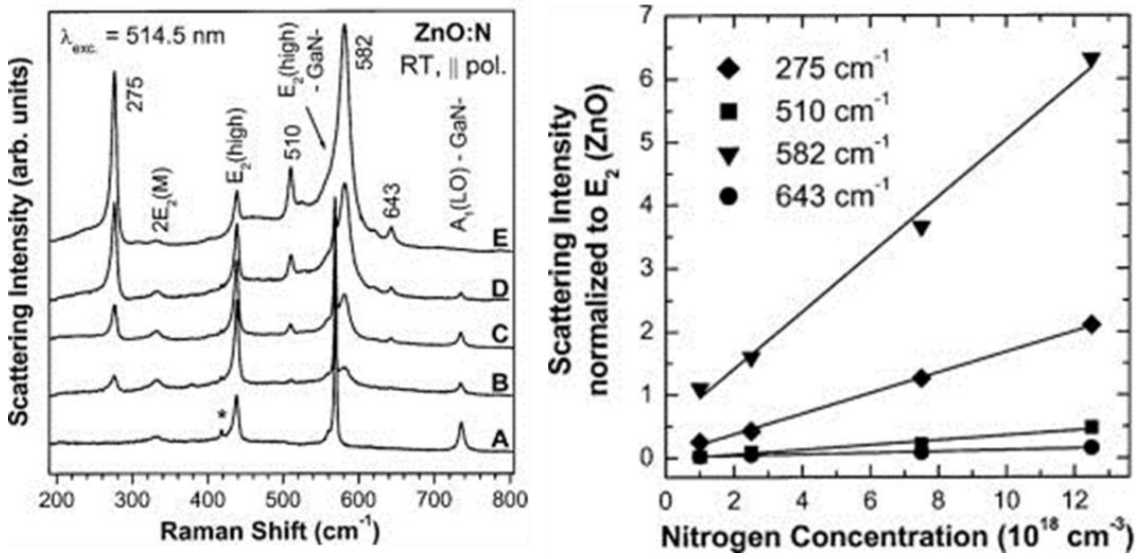

Figure 2.5 A) Room temperature Raman spectra of five ZnO samples. The nitrogen concentration increases from sample A to E. The peak marked by an asterisk originates from the sapphire substrate. B) Normalized intensity of the LVMs as function of the nitrogen concentration. The lines represent linear fits. Taken from figure 2 and 4 in Ref [117].

Raman spectroscopy is often used to prove the presence of nitrogen in N-doped ZnO. The Raman peaks at 275, 510, 582, 643, and 856 cm^{-1} that do not belong to the first- or second-order structure of ZnO are assigned to N-related defects [117]. This was proven using samples with increasing nitrogen concentrations and observing an increase in the relative Raman peak intensities (see Figure 2.5).

2.1.4 Influence of defects on ZnO properties

Annealing ZnO has a significant impact on the defects present in the material, which give rise to various optical, crystallographic, morphological, and electrical properties. Part of this thesis concentrates on the influence of defects on ZnO properties. Therefore, the following section provides a background into areas that are well-established and others that remain controversial.

2.1.4.1 Photoluminescence (PL)

This technique is often used to identify the quality of ZnO as it can easily establish when defects are present. PL employs laser illumination greater than the bandgap of ZnO to excite electrons from the valence band to the conduction band. When the excitons relax to lower energy levels they release photons or phonons depending on the energy difference. For ZnO there are two PL regions typically referred to as near band-edge emission (NBE)

and deep-level emission (DLE). The first corresponds to the bandgap energy of ZnO in the UV region ~3.3 eV and is typically a narrow, intense peak for highly-crystalline samples. The latter DLE exists in the visible part of the spectra and corresponds to defect levels positioned between the valence and conduction band. Although the transition energy gives evidence of the defects presence, the identity of defect-levels remains controversial. Figure 2.6 in co-ordination with Table 2-1 represents a compilation of predicted defect energy levels in the ZnO band structure.

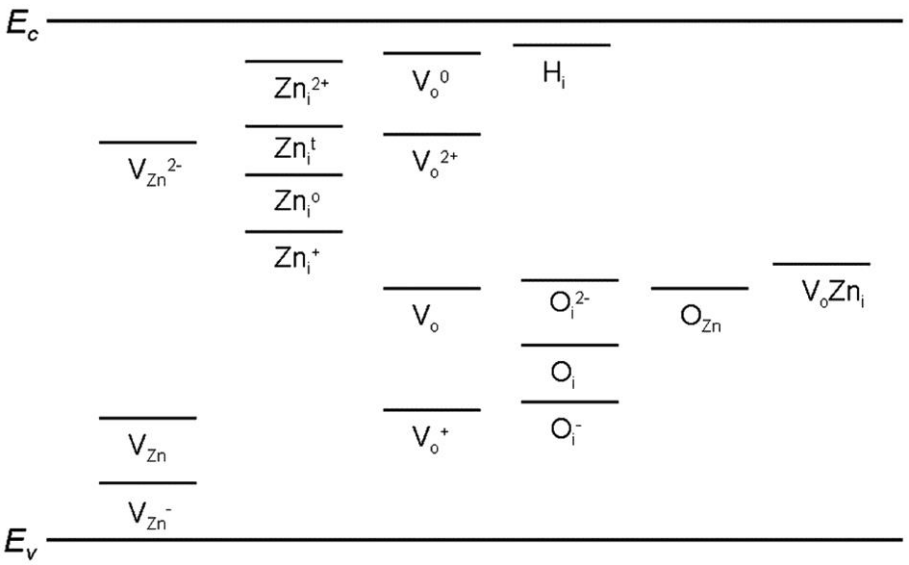

Figure 2.6 ZnO energy band structure showing the calculated defect energy levels obtained from different studies. V_{Zn}, V_{Zn}^- and V_{Zn}^{2-} denote neutral, singly charged, and doubly charged zinc vacancy respectively. Zn_i^o and Zn_i^t indicate neutral octahedral zinc interstitial and neutral tetrahedral zinc interstitial while Zn_i^+ and Zn_i^{2+} indicate singly charged and doubly charged zinc interstitial. V_o^0 and V_o denote neutral oxygen vacancy while V_o^+ and V_o^{2+} denote singly charged and doubly charged oxygen vacancy. H_i and O_i represent oxygen and hydrogen interstitial respectively while O_{Zn} indicates antisite oxygen and V_oZn_i denotes a complex of oxygen vacancy and zinc interstitial. Obtained from ref. [118].

Table 2-1 Defect energy levels calculated from the conduction band minimum correspond to the defect levels shown in Figure 2.6.

Defect	Energy level (eV)	Refs.
V_{Zn}	1.72, 1.93, 2.2, 3.06	[119–122]
V_{Zn}^{-}	2.11, 2.6, 2.66, 2.95, 3.14	[121–123]
V_{Zn}^{2-}	0.56, 3.05	[121,123]
Zn_i^{0}	0.05, 0.061, 1.03	[121,123–125]
Zn_i^{t}	0.031, 0.1, 0.46	[119,120,124,125]
Zn_i^{+}	0.2, 0.25, 0.5, 0.99	[121–123]
Zn_i^{2+}	0.08, 0.15	[121,126]
V_o^{o}	0.05	[123]
V_o	1.62, 2.3, 2.56, 3.0	[119–122,124]
V_o^{+}	0.84, 2.0, 2.36, 3.1	[121–123]
V_o^{2+}	0.25, 0.61, 1.2	[121,124,126]
H_i	0.03–0.05	[122]
O_i	0.73, 2.28, 2.96	[119–121]
O_i^{-}	1.83, 3.02	[121]
O_i^{2-}	2.41, 2.61	[121]
O_{Zn}	2.38	[119,120]
V_oZn_i	2.16	[120]

The source of green PL (~2.4 eV) has been debated for over 30 years [127–129]. Initially it was unambiguously linked to Cu impurities [130–134]; however, it was then associated with oxygen vacancies (V_O) due to an EPR peak at g~1.96. It has since been shown that this EPR peak actually belongs to shallow donors [70,135–137]. Oxygen interstitials on zinc sites (O_{Zn}) [119,138–140] and zinc vacancies (V_{Zn}) [68,141] have also been suggested as sources of green PL. Over recent years, there has been a growing consensus towards V_{Zn} as the most energetically favourable source due to its low energy of formation and stability at RT in n-type ZnO [82,142–144]. However, point defects are typically annealed out above 600˚C, and yet evidence of green emission exists post-annealing at temperatures up to 1200˚C [145]. This suggests a defect-complex involving V_{Zn} could be the cause, as it would be significantly less mobile than single point defects. A recent assessment of ZnO after being annealed in oxygen and zinc atmospheres and analysed using EPR, PL, and PAS techniques has shown that Cu impurities can be substituted on Zn-sites (Cu_{Zn}) to form a defect-complex [137,146]. This would fit both the low energy of formation as well as the reduced mobility at higher anneal temperatures. In addition, it was

reported that V_O may act as compensators to the Cu_{Zn}, quenching the green emission for reducing atmospheres.

Yellow emission (~2.2 eV) has been linked to oxygen interstitials [147,148] but more commonly associated with extrinsic Li impurity as observed with GaN [63,149]. Red emission (~1.75 eV) is often assigned to surface-related defects such as adsorbed O-H groups [150], however it is observed to have several peak positions. This suggests multiple defects may be responsible. It has also been reported that red emission intensity is usually visible for as-grown ZnO and is often sacrificed during annealing to give rise to green emission [151]. This indicates competition between the two different defect states for the same charge carriers.

2.1.4.2 Colouration

As a thermochromic material, ZnO typically changes from grey-white to yellow at temperatures above 300˚C. This behaviour is linked to the removal of minute amounts of oxygen from the surface that lowers the Gibbs energy of the system and forms an alternate non-stoichiometric $Zn_{1+x}O$, where X is dependent on the anneal temperature and atmosphere. Upon cooling the coloration reverts back to its original state as a result of oxygen from the atmosphere re-adsorbing onto the crystal surface.

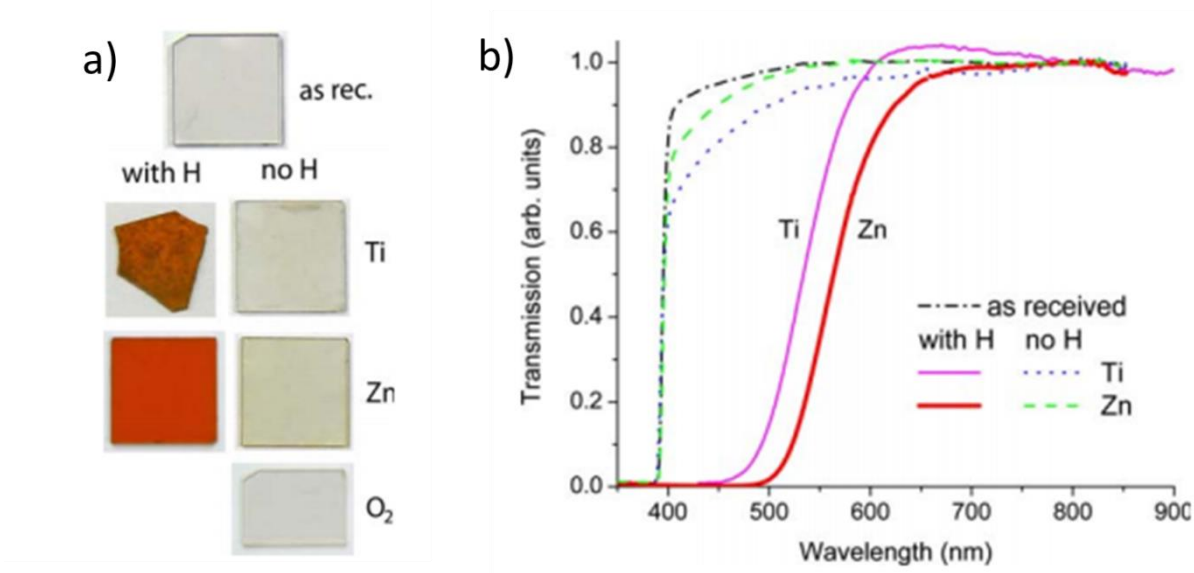

Figure 2.7 a) Photographs of as-received ZnO (top) and after annealing with or without hydrogen present (columns) and in the presence of Ti or Zn (rows). The bottom photograph shows ZnO after two anneals of first Ti (no H) followed by annealing in oxygen. The plot in b) shows the transmission spectra of ZnO samples in a). Ref. [152].

Numerous reports however show that ZnO can permanently change colour upon annealing [71,78,152]. Weber *et al.* annealed a ZnO single crystal in Zn vapour at 1100˚C (for 30 minutes) that resulted in the ZnO sample turning red (see Figure 2.7). Furthermore, these authors reported an increase in electrical conductivity [152]. The significance of annealing on point defects in the crystal lattice has been investigated using various atmospheres. When a previously transparent ZnO sample was annealed in Zn vapour (at ~1100˚C for 30mins), visible colour transitions had occurred and the sample became yellow, orange, red, or brown dependant on specific conditions [153]. This thermochromic process was attributed to the formation of V_O at the ZnO surface that gradually diffuses into the bulk. As oxygen ions migrate to the surface they bond with Zn vapour to form a new layer of ZnO on the surface. This altered the proportion of Zn to O in the ZnO crystal so that purportedly significant amounts of V_O can exist. These act as optical traps and gives rise to the visible discolouration. Annealing in the presence of phosphorous or titanium rather than Zn vapour resulted in the same red colouration, further supporting the presence of V_O rather than Zn_i [71,80]. However, single point defects would anneal out at these elevated temperatures. Instead it was shown that the presence of hydrogen was critical to the decolouration of ZnO. The most stable H_O defect was used to explain the red colouration and red-shift in optical transmission (Figure 2.7b). As discussed previously, H_O acts as a shallow donor and so the increase in conductivity measured by Hall Effect measurements was used to supports this. However, previous studies have shown high anneal temperatures or prolonged anneals would remove hydrogen from the ZnO (see section 2.1.3.2.1). Hence, the cause of ZnO decolouration remains in question.

The effects of annealing is often discussed for single-crystal ZnO or ZnO films, however in the case of nanostructures the diffusion length out of the sample is greatly reduced. It would suggest that for nanostructures a lower temperature or shorter duration would be sufficient to achieve a similar effect.

2.1.4.3 Morphology and crystallography

The crystal structure of ZnO undergoes irreversible morphological changes when it is submitted to thermal treatment and a critical temperature is reached. The necessity for thermal treatment arises from low-temperature synthesis routes that construct

nanostructures from the bottom-up, where intrinsic and extrinsic defects are easily incorporated into the crystal lattice.

In these cases, the low Gibbs-free energy of formation prevents diffusion of atoms into the more stable energy states and results in unaligned crystalline regions or multiple crystal phases. Upon heating in oxidising conditions, the faceted surface is refined due to reconstruction and relaxation of surface atoms. ZnO possesses ionic-bonding and so allows both the metal and the oxygen atoms to relax inward providing greater degrees of stability [154]. However, reducing atmospheres (e.g. forming gas) can lead to surface damage and thinning of ZnO nanorods [129]. Degradation of the surface was also found to occur in arsenic vapour and was shown to be non-reversible [153].

2.1.4.4 Photoconductivity

Thermal annealing improves ZnO conductivity by refining the crystal structure and removing point defects that serve as recombination sites. However, surface defects play a major role in influencing the photoconductive behaviour of ZnO.

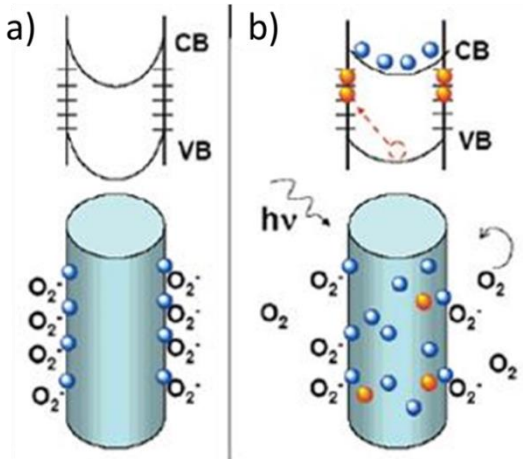

Figure 2.8 Schematic of ZnO nanowires showing the trapping and photoconduction mechanism. The energy band diagrams a) represent the situation in darkness and b) under UV illumination. Ref. [8].

Post-processing, atmospheric oxygen and water molecules readily adsorb onto the hydrophilic ZnO surface. Oxygen molecules adsorbed on the surface act as trap states that capture free electrons in the n-type semiconductor [$O_2(g) + e^- \rightarrow O_2^-(ad)$]. This gives rise to upward band-bending near the surface and corresponds to a depletion region (see Figure 2.8). Upon illumination ($h\nu > 3.3$ eV), photo-excited electron-hole pairs are generated [$h\nu \rightarrow e^- + h^+$] in the ZnO nanorod. Due to the upward band-bending near the surface,

holes migrate toward the depletion region. Here, the holes discharge negatively-charged oxygen ions, which consequently desorb from the surface [O_2^-(ad) + $h^+ \rightarrow O_2$(g)] (see Figure 2.8). The unpaired photoexcited electrons contribute to the charge carrier density and migrate to the anode [8]. The photoconductive effect is also influenced by the atmospheric conditions, which can determine the rate of photo-desorption/adsorption [155]. In the case of nanostructured ZnO the increased surface area dramatically enhances the photoconductivity and is a dominant factor behind its use in optical applications.

2.1.5 Extended X-ray absorption fine structure (EXAFS) analysis

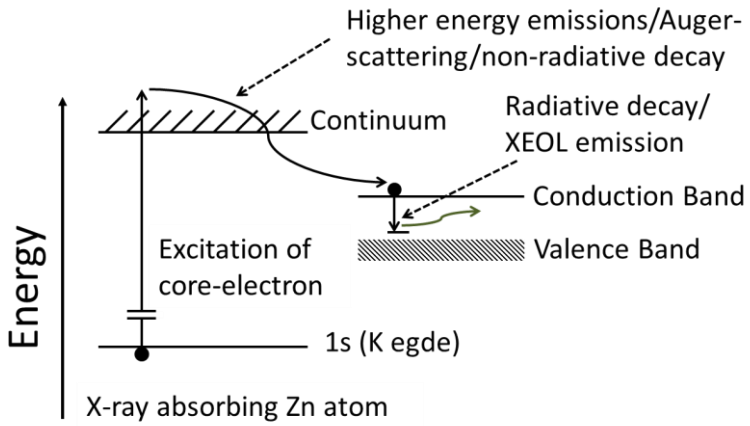

Figure 2.9 Schematic showing the X-ray excitation of a core-electron from the ZnO K edge and its decay pathway that leads to an optically detected photon (XEOL) emission.

Extended x-ray absorption fine structure (EXAFS) is a technique that obtains local structural information surrounding an absorbing element. This is achieved by measuring x-ray absorption that corresponds to excitation of the core electrons. X-ray excited optical luminescence (XEOL) is a variation of EXAFS that utilises visible emission (see Figure 2.9). This provides local atomic structural information relating to the light emitting region around the x-ray absorbing element [156]. This energy is known as the absorption edge, and for the Zn *K* edge it is ~9659 eV. As the electrons relax from the continuum they undergo both radiative and non-radiative decay paths. The radiative emissions that are optically-detected are referred to as XEOL (and otherwise known as photoluminescence yield). The XEOL is typically collected for a specific wavelength range using a photodiode detector connected to a spectrometer.

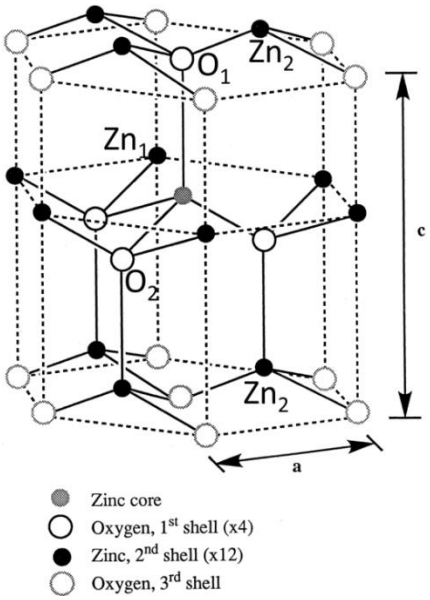

Figure 2.10 Atomic structure of wurtzite ZnO adapted from ref. [157] to show the atomic positions surrounding the central Zn atom.

Fourier transforms (FT) of the EXAFS absorption spectra provide a convenient picture of inter-atomic distances surrounding the central absorbing atom (Zn) where the emission originates. Hence, in optically-detected mode it is believed this technique can uniquely identify the structural environment responsible for particular emission wavelengths. As the distance from the central Zn atom increases so too does electron scattering and so typically limits the range to the first few atomic shells around a central atom. These shells are related to the atomic-bonds: Zn-O_1, Zn-O_2, Zn-Zn_1, and Zn-Zn_2 with coordination numbers (N) 1, 3, 6, and 6, respectively (Figure 2.10). EXAFS collected in transmission mode (TM) does not identify specific regions responsible for the emission, but probes the average bulk atomic structure of a material.

Fluorescence, transmission, and time-resolved XEOL are EXAFS techniques previously used to study doped-ZnO. They successfully showed dopant atoms (Fe [158], N [159], Eu [160] and Cu [161]) displacing the oxygen and zinc atoms to fit the wurtzite structure. Rosenberg et al. [162] used XEOL analysis at the O *K* edge to show that orbital directionality has a strong influence on the optical luminescence for wurtzite ZnO nanostructures. They assigned 2.4 eV emission to surface defects and excluded V_O as a possible source but did not provide structural information about the lattice. S. Lacheri et al. [163] collected XEOL in fluorescence and optically-detected modes for the first time from ZnO thin films in 2005 and studied the x-ray absorption near-edge spectra (XANES).

They successfully distinguished between the defected electronic structures using the XANES intensity and shift in absorption. However, the absence of an EXAFS signal indicates the quality of data was not sufficient to provide structural information about the shells surrounding the absorbing Zn atom. Hence, until a high-quality EXAFS signal is obtained in optically-detected mode, it is in question whether this technique can be used for structural analysis.

2.2 Hole Collectors

2.2.1 Copper thiocyanate (CuSCN)

Numerous solid state hole conductors exist such as $CuAlO_2$ [164], NiO [165,166], CuI [167,168], and CuSCN [169–172]. Of these mentioned, NiO is poisonous and exhibits low open-circuit voltages in TiO_2-based DSSCs, whereas CuI initially leads to high efficiencies in DSSCs but poor long-term stability due to the photo-oxidation of Cu(I) to Cu(II). The Cu(I) in CuSCN however is stable during illumination and so is of particular interest due to its unique chemical robustness associated with its polymeric structure. The multiple deposition techniques available to CuSCN provide another advantage, however there remains the question of which processing method provides optimal coverage and performance for nanostructured surfaces. In addition, researchers have successfully improved the conductivity of CuSCN through doping [170,173]. This section reviews the CuSCN structure and properties, and deposition techniques currently used.

2.2.1.1 Properties

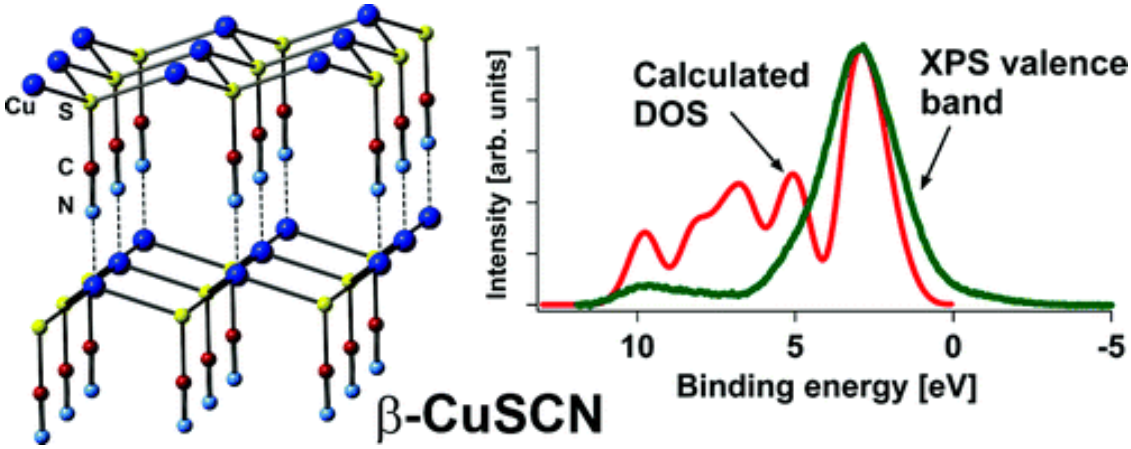

Figure 2.11 The hexagonal-CuSCN molecular structure of a 3 x 3 x 1 supercell (left) and the corresponding calculated density of states (right). Ref. [174].

Two structures are known for CuSCN, the hexagonal/rhombohedral β-phase [175,176], (see Figure 2.11) and the orthorhombic α-phase [177]. Hexagonal β-CuSCN is typically used as a hole collector in solid-state devices. The SCN^- molecular ion is monovalent, accepting only one electron from the Cu cation. This is due to a covalent single bond between sulphur and carbon $(S{-}C{\equiv}N)^{-1}$. Hence, there is a shared electron pair that enables both S and C to attain closed shells with two fewer transferred electrons required than if separated into sulphide and cyanide. The nitrogen forms a triple bond with carbon and also has lone pair of electrons that is not shared covalently but forms a weak dipolar bond with copper. The intrinsic holes in CuSCN are associated with Cu deficiency. Consequently, p-type conductivity is predicted to be enhanced through the formation of Cu vacancies, as well as the formation of C-N vacancies [174].

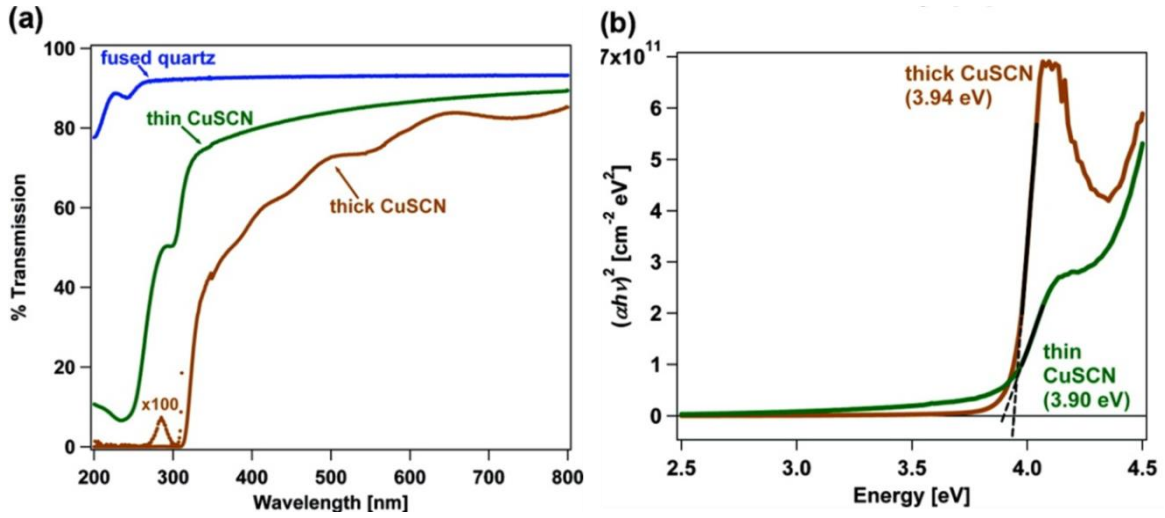

Figure 2.12 a) Transmission spectra of thick and thin CuSCN deposited on a fused quartz substrate and b) the corresponding Tauc plot with the band-gap values determined by extrapolated linear fits, ref. [174].

CuSCN is an inorganic wide-bandgap (3.6 eV) p-type semiconductor [178] that exhibits good optical transparency to the visible spectrum (see Figure 2.12). This is ideal for optical applications that require a visible-blind window as a hole collector. However, as can be seen from Figure 2.12, the thickness of the CuSCN can have a significant impact on the optical absorption and bandgap energy. The aforementioned chemically stability of CuSCN lends itself to long term stability and robustness that is expected of solid-state devices. The suitability of CuSCN for device applications is also significantly dependant on the electrical properties; the measured hole conductivity of 1.4 Sm^{-1} and hole mobility of 1.08 $cm^2/V.s$ after doping affirm its suitability [179]. However, this is far from ideal.

Consequently, the thickness of the CuSCN layer will play a major role in determining the series resistance of the material, and so controlling this parameter would be highly advantageous.

2.2.1.2 CuSCN deposition techniques

The high porosity and fragile nature of nanostructured surfaces make it a challenging task to fully saturate the pores without damaging the delicate structure. A number of deposition techniques have been performed in attempt to achieve this: electrochemical deposition [180–183], impregnation (or drop-coating) [172,184–187], successive ionic layer adsorption and reaction (SILAR) [188], and CBD [189].

The aforementioned CuSCN thickness is an important parameter in the device fabrication for the conductivity as well as the visible-transparency. Ideally the CuSCN layer should fully saturate the nanostructured surface and leave a thin layer (100-300 nm thick) on top of the nanostructured surface. This would facilitate hole mobility to the top electrode without significantly increasing the series resistance. The effectiveness of the coating can often be determined by electrical analysis using the rectification ratio of the device; alternatively observations can be made using optical analysis techniques such as SEM imaging. Table 2-2 offers a comparison of various devices using different CuSCN deposition techniques.

Table 2-2 A list of solar cells and photodiodes that reported using CuSCN as a p-type material.

Deposition method	Structure	Rectification	V_{OC} (V)	J_{SC} (mA/cm^2)	CuSCN thickness (μm)	Ref.
Electrochemical	TiO_2/CuSCN	33 (1.5 V)		-	1	[183]
Electrochemical	ZnO/CuSCN	19 (0.5 V)		-	-	[181]
Electrochemical	ITO/ZnO/CuSCN/Ag	154 (2 V)		-	-	[190]
Electrochemical	ITO/ZnO/CuSCN/Au	3 (4 V)		-	-	[182]
Impregnation	TiO_2/N719/CuSCN	-	0.6	10.5	-	[170]
Impregnation	FTO/ZnO/In_2S_3/CuSCN/Au	-	0.6	11	3	[184]
Impregnation	ITO/ZnO/N719/CuSCN/(Ti/Au)	-	0.3	0.3	0.6	[191]

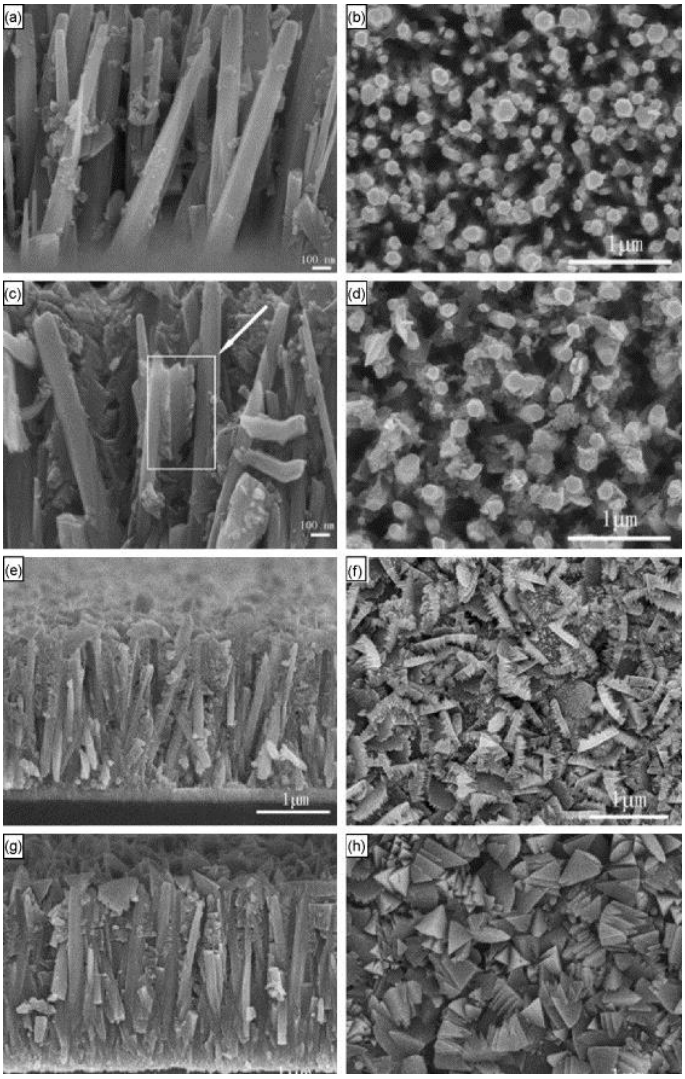

Figure 2.13 SEM images of cross-sectional and top views of electrodeposited CuSCN on ZnO rod arrays with different deposition time (a) and (b) 5 min, (c) and (d) 15 min, (e) and (f) 1 h, at the potential of −500 mV and temperature 0°C. (g) and (h) were prepared at −500 mV and 20°C for 1 h deposition. Ref. [181].

Electrochemical deposition is a popular choice for CuSCN coating; it offers reasonable pore-filling capabilities but is limited by the large grain-size (see Figure 2.13). This leads to a rough top layer that firstly, increases the contact resistance between the top electrode and the CuSCN, and secondly, gaps in the CuSCN layer may give rise to shorts when the top electrode is deposited. Furthermore, this method may not be suitable for pre-coated nanostructures (e.g. dyes/ nanoparticles/polymers) as it requires immersion in a chemical solution that may react or remove the previously deposited coatings during the electrochemical process.

Selk et al. compared three CuSCN depositions methods: electrodeposition, SILAR and impregnation on DSSCs [192]. The impregnation technique penetrated the porous ZnO layer the most effectively and yielded the highest performance of the three methods with a quantum efficiency of 0.46%. The large grain-size of CuSCN produced by electrodeposition prevented penetration through the ~20 nm sized pores in the ZnO layer, and reduced the efficiency to 0.017%. Poor pore-filling using the SILAR technique was assigned to the blockage of ZnO pores at the surface; this led to a build-up of CuSCN on top of the porous structure and prevented further penetration. This resulted in the lowest efficiency of the three DSSCs of 0.011%.

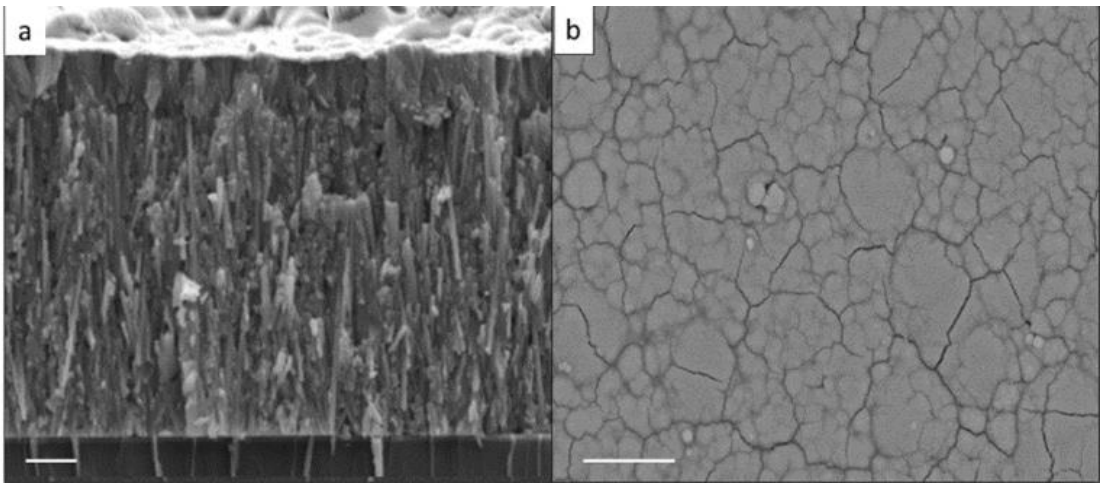

Figure 2.14 SEM images of the ZnO nanowire array after CuSCN impregnation deposition. (a) Cross-sectional image, scale bar 2 µm. (b) Top-view image, scale bar 10 µm. Ref. [193].

Impregnation is the commonly implemented method for depositing CuSCN due to its simplistic procedure that yields reasonable pore-filling (Figure 2.14a). This typically involves dissolving CuSCN powder in n-propyl sulphide (n-PS), where the concentration is reported to vary from 0.05 M [187] to an excess of CuSCN and removing the surfactant after centrifuging [185]. The clear solution is drop-coated using a glass pipette and spread onto the desired surface while it is heated on a hotplate between 65-100°C. The heat is required to remove the n-PS from the CuSCN, however this is a slow process and it is reported that devices are left in vacuum for days to completely remove the residual solvent [172,194]. A side-effect of the slow-evaporating solvent is the formation of cracks on the CuSCN surface (see Figure 2.14b). Hairline-cracks throughout the CuSCN layer leads to shorts and can significantly increase the series resistance of the CuSCN by limiting the hole-mobility [191,193].

2.2.2 Poly(3,4-ethylenedioxythiophene) /(PEDOT)

As well as inorganic hole collectors, there exist a number of conductive polymers that may be used as hole collectors: poly[2,5-dimethoxy-,1,4-phenylene-1,2-ethenylene-2-methoxy-5-(2-ethylhexyloxy)-1,4-phenylene-1,2-ethenylene] more commonly known as M3EH-PPV [195,196], poly(3-thiophene) [197], and poly(3,4-ethylenedioxythiophene) known as PEDOT/PEDT [198–201]. PEDOT was selected for this project due to its well-established background with regard to material properties and its use in optoelectronic devices. A background into PEDOT properties and its use in nanostructured devices will be given here.

2.2.2.1 Properties of PEDOT:PSS

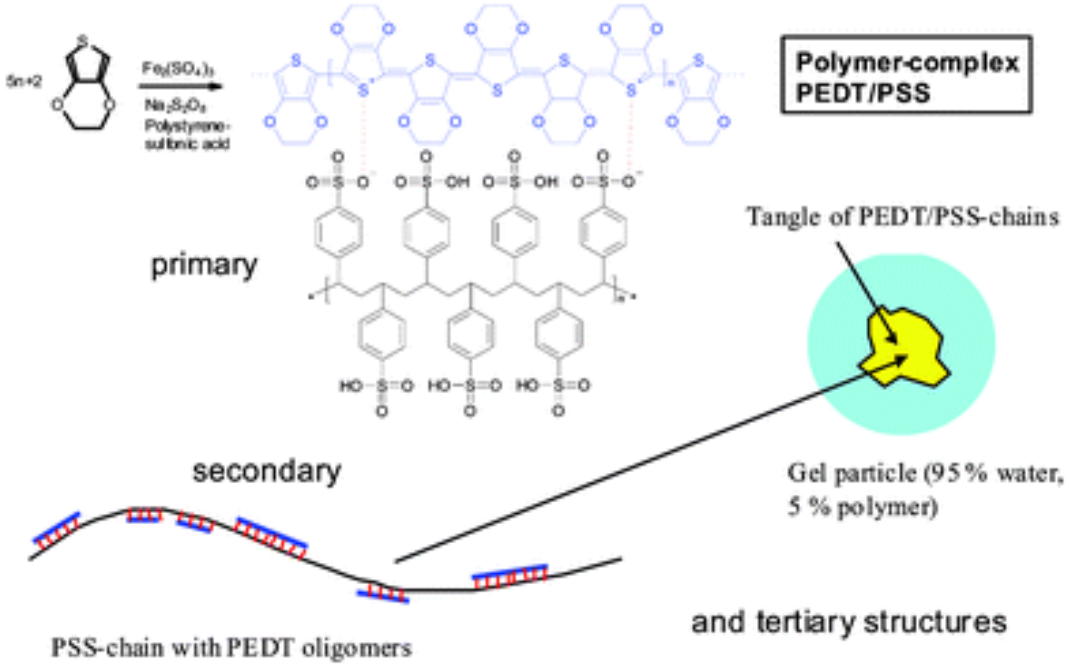

Figure 2.15 Synthesis, primary, secondary and tertiary structure of aqueous soluble PEDOT:PSS. Ref. [198].

PEDOT is an insoluble polymer with a high conductivity of 300 S/cm. To resolve the issue of insolubility a water-soluble polyelectrolyte was employed, poly(styrene sulfonic acid) (PSS) to form PEDOT:PSS (see Figure 2.15). The PEDOT:PSS dispersion appears dark blue and exhibits good film-forming properties, high conductivity (10 S/cm), good transmission to visible wavelengths and excellent stability [202–204].

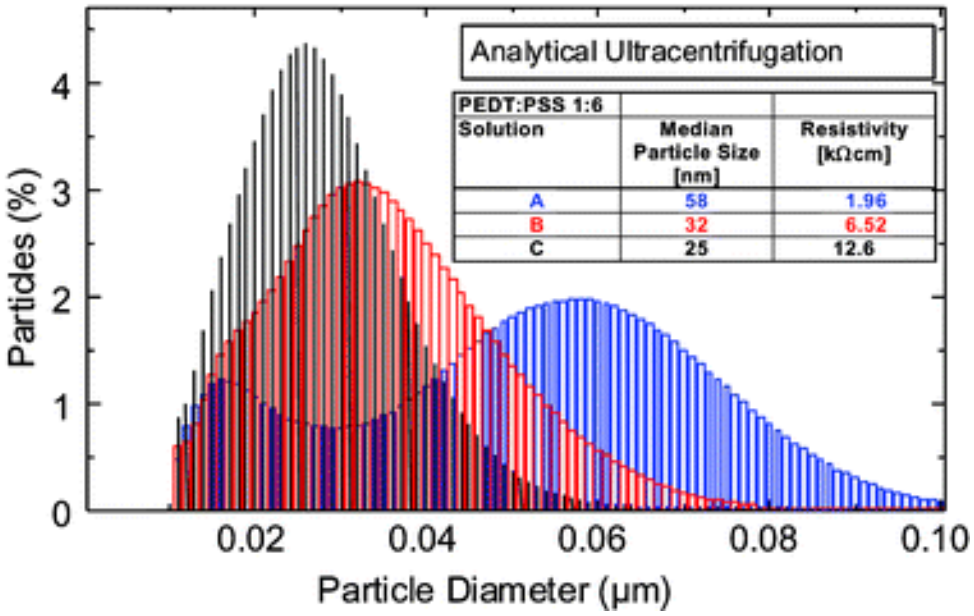

Figure 2.16 Relationship particle size/resistivity with constant PEDOT:PSS ratio. Ref. [198].

PEDOT:PSS films are reported to be highly stable, with no change in conductivity after being treated for up to 1000 h at 100˚C [205]. The particle size of PEDOT however, was shown to play a significant role in the conductivity and was dependent on the ratio of PSS to PEDOT. It was reported that smaller particles sizes significantly reduce the conductivity as well as the viscosity (see Figure 2.16) [198]. This is due to the PSS acting as an electrical insulator, restricting the transport of holes within the PEDOT polymer network [206].

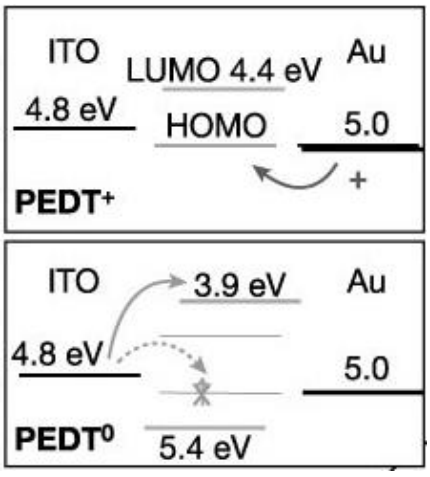

Figure 2.17 Energy level diagrams of 40 nm-thick PEDOT:PSS in the oxidized (upper panel) and neutral (lower panel) states, along with the electrode arrangement. Ref. [206].

The band-gap energy of PEDOT can range from 1.4 – 2.5 eV; this is controlled by adding substituents and co-repeat units that adjust the highest occupied molecular orbital (HOMO) and lowest unoccupied molecular orbital (LUMO) [198]. However Möller *et al*. [206] reported that the energy levels of PEDOT:PSS are responsible for the charge transport properties in the device (see upper panel Figure 2.17). The upper panel shows that in the positively charged state ($PEDOT^{+}$), the HOMO and LUMO are separated by 0.6 eV, and holes can be injected to the HOMO (at 5.0 eV) from either the ITO or Au electrodes. When a bias is applied that injects an electron, this results in the chemical reduction of $PEDOT^{+}$ to $PEDOT^{0}$, and is reported to change the energy levels so that the optical band-gap is now ~1.5 eV (lower panel Figure 2.17). Therefore, while there is an applied bias there is a rapid continuous oxidation and reduction taking place with the transfer of holes and electrons into the polymer.

2.2.2.2 PEDOT:PSS applications

The simple deposition process of PEDOT:PSS , good conductivity, and optical transparency to visible light have benefited the fabrication of solar cells [207–209] and LEDs [210–213]. A PEDOT:PSS layer on top of a Si p-i-n diode or ZnO was used to fabricate write-once read-many-times memory (WORM) devices that are used for radio frequency identification [206,214]. Piezoelectric energy-harvesting devices have taken advantage of the flexibility that conductive polymers offer and incorporate PEDOT:PSS either as electrode or as a hole collector [215,216]. PEDOT:PSS does not effectively penetrate pores in nanostructured devices due to its grain-size and polymeric structure. However this serves as a convenient hole collector in gas sensors that require the surface area used for sensing to remain exposed [217–219].

Although there exists a wide-range of applications for PEDOT:PSS, these few examples are given to highlight the versatile nature of this conductive polymer and demonstrate its well-established properties in device performance.

2.3 Ultra-violet photodetectors

As discussed in section 2.1.1, a large number of optoelectronic, energy-harvesting, and sensing devices can be fabricated using ZnO-nanorods. The final experimental chapter of this thesis is focused on UV photodetectors. Here, a background on photodetector

applications and commonly-used materials will be presented, with special attention given to ZnO-based devices.

2.3.1Background and theory

UV light is the electromagnetic radiation that occupies the spectral region λ = 400-10 nm. This highly ionising radiation is capable of activating many chemical processes and so detection of UV light is important for a wide range of applications. These include chemical and biological analysis (ozone, pollutants and organic compounds produce absorption lines in the UV region), flame detection (fire alarms, missile warning or combustion monitoring), optical communications (inter-satellite communications at $\lambda < 280$ nm), emitter calibration (instrumentation, UV lithography), and astronomical studies [7].

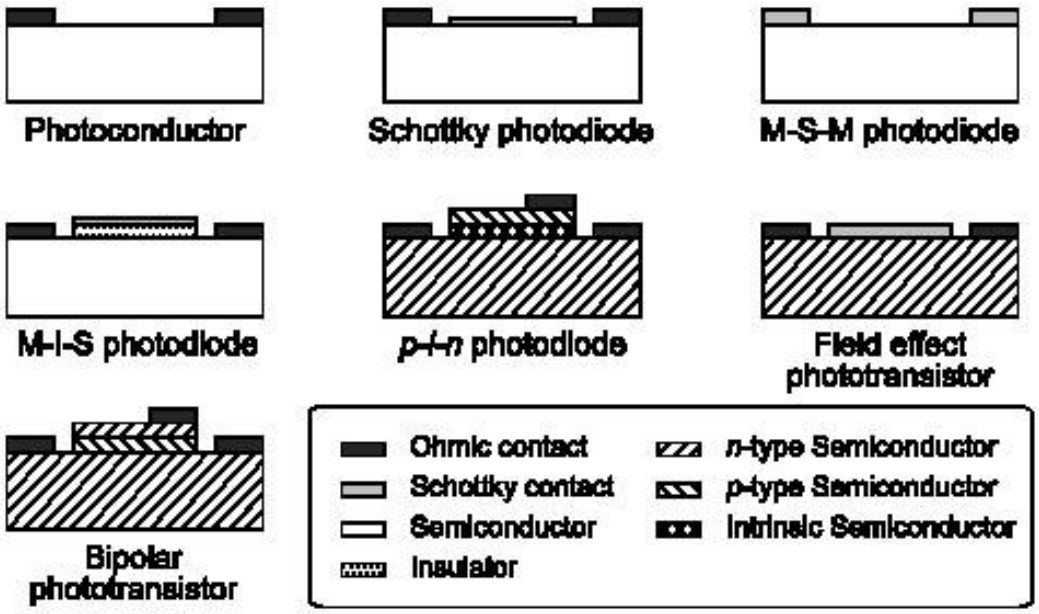

Figure 2.18 Schematic structure of different semiconductor photodetectors. Ref.[7].

A wide range of structures can perform the task of photodetection, for example: photoconductors, Schottky barrier photodiodes, metal-semiconductor-metal (MSM) photodiodes, metal-insulator-semiconductor (MIS) structures, p-n and p-i-n photodiodes, and field-effect and bi-polar phototransistors (see Figure 2.18). These fundamentally operate on the principle of photoconductivity/photovoltaic behaviour where the absorption of a photon results in the excitation of an electron from the valence band to the conduction band of the semiconductor. Hence, incident photons are directly converted into an electrical signal that can be collected by an external circuit. The main advantages of these

semiconductor photodetectors over other photodetectors are their small and lightweight structure, their insensitivity to magnetic fields, and their capability for high-speed operation.

Critical parameters used to describe the essential properties of semiconductor photodetectors are:

- Responsivity (R_λ), photoconductive gain (g) and quantum efficiency (η). Responsivity is defined as the photocurrent per unit of incident optical power. This is found using the quantum efficiency (number of electron-hole pairs generated per incident photon) and gain (number of carriers detected per photogenerated electron-hole pair) in the following expression:

$$R_\lambda = \frac{\lambda\eta}{hc} qg \qquad (1)$$

  where λ is the radiation wavelength, h is the Planck constant, c is the speed of light and q is the electron charge [7].
- Response times for detection and recovery are important factors when considering semiconductor photodiodes as these can vary significantly. These are referred to as the rise time, τ_r (or decay time, τ_d) and typically defined as the time in which the photocurrent increases from 10% to 90% (or decreases from 90% to 10%) of its maximum value when excited by high energy monochromatic laser pulses.
- Spectral photosensitivity, I_λ, is the ratio of photocurrent for a specific wavelength vs. the dark current, expressed as:

$$I_\lambda = \frac{I_{light} - I_{dark}}{I_{dark}} \qquad (2)$$

2.3.2 Semiconductors for UV photodetection

Semiconductors that satisfy the following conditions would be suitable for UV photodetection:

i. insensitivity to light in the visible spectral region (often referred to as visible-blind photodetectors),
ii. a high quantum efficiency,
iii. a high dynamic range of operation,
iv. and low background noise, i.e. high photosensitivity to low irradiances.

A few of the well-established semiconductors that fall into this category will be briefly discussed here.

2.3.2.1 Si-based photodetectors

Silicon-based photodetectors were initially designed for use in the visible spectral range due to silicon's relatively narrow indirect-bandgap of 1.1 eV. However it has also been applied to UV photodetection through the use of either p-n junctions or charge-inversion photodiodes. A thin layer of SiO_2 (~60 nm) typically coats the surface of the Si and is reported to play a dual role of surface passivation as well as act as an anti-reflection coating [220,221]. In the case of charge-inversion photodiodes, the presence of an electric field at the Si/SiO_2 interface drives the photodetection for high-energy radiation that is absorbed close to the surface. However, a number of drawbacks exist for these devices; the performance was shown to degrade over time as a result of UV light damaging the thin SiO_2 layer [220], sensitivity of Si to visible/infra-red wavelengths meant filters are required to block out unwanted spectral regions thus reducing the effective area of the device, and finally to reduce noise for high-sensitivity detection the active area must be cooled- this behaves as a cold trap for contaminants leading to lower photosensitivity [222].

2.3.2.2 Wide-bandgap photodetectors

Wide-bandgap semiconductors prevent the absorption of lower energy wavelengths, and so acts as a natural filter against the visible/IR spectrum. This advantage allows photodetectors to operate at RT. Furthermore, the strength of semiconductor chemical bonds provides photodetectors with radiation hardness and enhanced stability.

With these benefits there are also limitations; the most critical of these is the crystal quality. The difficulties in fabricating defect-free semiconductors results in most semiconductors possessing a significant quantity of dislocations, grain boundaries or point-defects. These act as optically active absorption centres that increase the detection of visible wavelengths, and also as recombination centres that contribute to the leakage current. Secondly, with most semiconductors it is necessary to increase the impurity dopant to achieve reasonable carrier concentrations. This however results in a reduction of carrier mobility.

Currently the most well-known photodetector materials include SiC [223], diamond [224–226], III-nitrides (AlN, GaN, InN) [227–229] and II-VI (ZnS, ZnSe, ZnO and other related compound semiconductors) [221] in a number of arrangements as shown in Figure 2.18. Because the focus of this thesis is on ZnO-based UV photodetectors, the next section will be dedicated to reviewing these devices in further detail.

2.3.2.3 ZnO-based photodetectors

As a wide-bandgap material ZnO has all the benefits that are associated with semiconductor photodiodes such as: radiation hardness, chemical stability, RT operation, and suitability for high-temperature and high-power applications. ZnO in particular is also a low-cost material that is easily fabricated by numerous techniques, some of which are low-temperature processes that allow flexible polymer substrates to be used.

Fabricius *et al*. [230] was the first to report a ZnO-based Schottky barrier type UV photodiode, using Au on a thin sputtered layer of polycrystalline ZnO. The device exhibited a τ_r of ~20 μs, a τ_d of ~30 μs and low quantum efficiency (1%) attributed to a large quantity of recombination centers in the polycrystalline ZnO layers. Since then, a multitude of MSM, p-n and p-i-n junction photodiodes involving ZnO have been fabricated and tested.

Liang *et al.*[6] reported a 1.5 A/W responsivity for an Ag-ZnO-Ag device under 368 nm, 0.1 μW illumination (at 5 V). The spectral photoresponse dropped by three orders of magnitude as the wavelength increased from 370 nm to above 390 nm, which corresponds to the ZnO band-gap energy of 3.35 eV. The τ_r and τ_d were reported as 12 ns and 5 ms, respectively. This rapid rise time is associated with the transit time of photo-generated electrons, whereas the prolonged recovery time has been linked to the re-adsorption of oxygen at the ZnO surface and grain boundaries [231,232]. ZnO is relatively unique in this sense in that it does not require impurity doping to enhance charge carrier concentration, instead it benefits from the photoconductivity provided by adsorbed oxygen (see section 2.1.4.4). This however, couples with the eventual re-adsorption of oxygen that can lead to prolonged photoconductivity (PPC).

A single ZnO nanowire laid across Au electrodes was the first ZnO-nanostructure tested as a UV photodetector [9]. Prior to this, only thin films had been used in ZnO photodetectors. Nanostructured ZnO maximises the photocurrent due to the additional surface-adsorbed oxygen contributing to the photoconductivity, furthermore, the scattering of photons may increase photon-capture. Kind *et al.* [9] presented a photocurrent of 10 nA (under 365 nm, 0.3 mW/cm^2 illumination) and a dark current of 0.01 nA at 1V. Although the rise and fall time appear to be relatively quick, this was not measured and was quoted as <1 s.

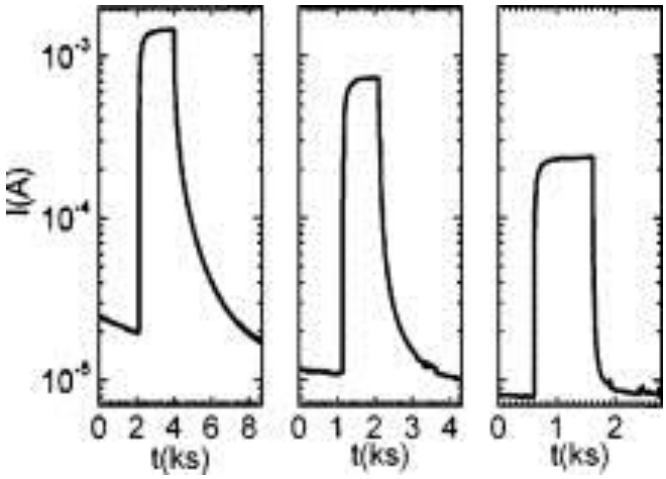

Figure 2.19 Photoresponse of the nanowire film to UV illumination in various oxygen pressures: 1.9×10^2, 2.0×10^4, and 1.0×10^5 Pa from left to right. [155].

The effect of atmospheric conditions on the UV photoresponse was also investigated. Wang et al. [155] found the response times of ZnO-nanowires (dispersed on Si-O-N substrate patterned with Pt electrodes) were faster in air than in vacuum, and the rate continued to improve with increasing oxygen partial pressure (p.p.). At 5 V the device was exposed to a 254 nm, 8W illumination source. In air, the current rose from 8 μA (dark) to 138 μA (UV) with τ_r ~50 s and τ_d ~710 s. In vacuum, the current increased from 14 μA (dark) to 5 mA (UV) and failed to saturate after 3300 s of exposure. The current failed to recover to its initial dark current even after a one-day period in the dark. For increasing oxygen p.p., the maximum photocurrent and dark current were shown to decrease (see Figure 2.19). The photosensitivity was quoted as 75, 65, and 30 for oxygen p.p. of 1.9x10^2, 2.0x10^4, and 1x10^5 Pa, respectively. The authors assign the differences in response times and photosensitivity to the rate at which oxygen physisorbs on to the ZnO surface. This has been supported by multiple groups since that have demonstrated similar behaviour under different atmospheres [233–235].

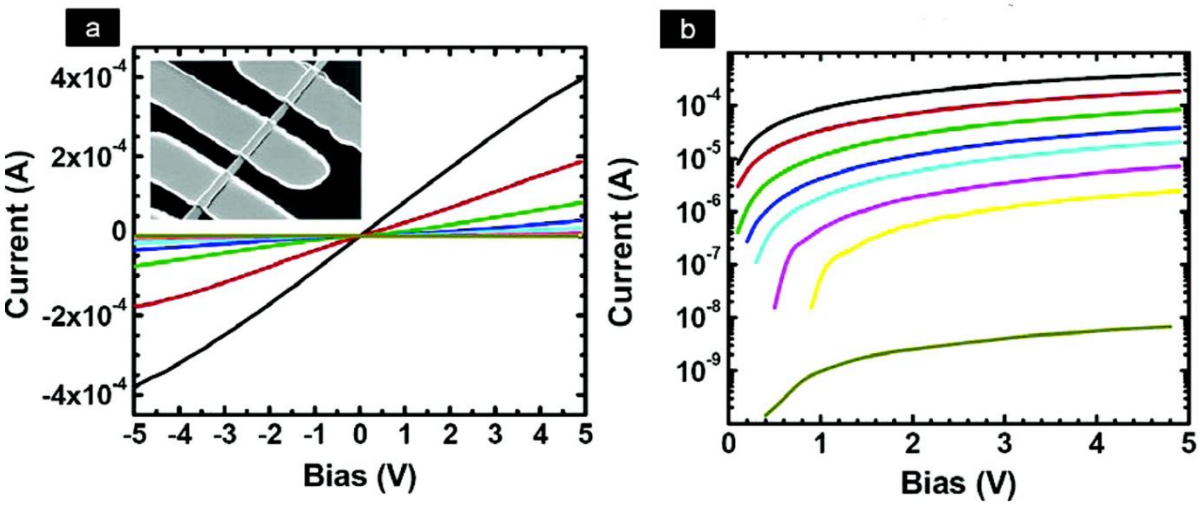

Figure 2.20 (a) I−V characteristics of a single-NW photodetector as a function of light intensity; from top to bottom, the curves were measured at the following intensities: 4 × 10^{-2} W/cm^2 (black), 4 × 10^{-3} W/cm^2 (red), 4×10^{-4} W/cm^2 (green), 1.3×10^{-4} W/cm^2 (blue), 4×10^{-5} W/cm^2 (cyan), 1.3×10^{-5} W/cm^2 (magenta), 6.3×10^{-6} W/cm^2 (yellow), and in dark (brown). Inset is the SEM image of a typical ZnO NW device (obtained at 45° tilt angle); the spacing between the electrodes is 2 µm. (b) The *I−V* curves presented in Figure 2.20a are re-plotted on a natural logarithmic scale. Ref. [8].

Varying the UV irradiance was tested on a single CVD-grown ZnO nanowire deposited onto a Si substrate with Ti/Au electrodes patterned on top (see inset Figure 2.20a). A high photoconductive gain (>10^8) was reported as the 390 nm irradiance rose from 6.8 µW/cm^2 to 40 mW/cm^2, which corresponds to a maximum photocurrent of 0.4 mA at 5 V (see Figure 2.20b). At lower light intensities the photocurrent followed a linear relation with light intensity, while at higher light intensities it deviated from this relation. The saturation of the photoresponse was explained by the number of available hole-traps at the ZnO surface decreasing at the higher intensities. τ_r and τ_d were reported as 23 s and 33 s, respectively, with a spectral photosensitivity of ~100. Fast transient photocurrent waveforms of ZnO nanowires in air show a rapid response of ~1 ns and a decay time of ~ 100 ns (at 1 V).

The difficulties in producing p-type ZnO has meant few ZnO p-n homojunctions exist. However, Lee *et al.* [236] reports a successful attempt in fabricating a UV photodetector using n-type ZnO nanowires (grown by CBD) and p-type Al, N co-doped ZnO film (grown by sol-gel). Upon 380 nm 55 µW/cm^2 illumination, a photocurrent of 175 µA was measured with a leakage current of 5 µA at -3 V. This corresponds to a photosensitivity of 35 and a responsivity of 4 A/W.

Multiple methods have been tested in attempt to increase the photocurrent response from ZnO-based diodes; these include surface functionalization [237], impurity doping [238,239], increased surface-to-volume ratio using nanostructured morphology [240], and nanowire arrays connected in parallel [241]. Each of these demonstrated positive results in increased photocurrent; however, the drawbacks of costly fabrication, prolonged response times or reduced photosensitivity/visible-blindness are common side-effects.

Table 2-3 summarises the critical parameters of the ZnO-based photodetectors.

Table 2-3 A comparison of ZnO-based photodetector performance.

Type	Structure	Growth method	Dark current	Responsivity/ Photocurrent	Response time τ_r/τ_d	Ref.
MSM	Ag-ZnO-Ag	MOCVD	1nA (5V)	1.5 A/W (5V, 368 nm)	12ns/5ms	[6]
MSM	Cr-Mn-ZnO-Au	RF-Sputtering	-	3 mA/W (365 nm)	20µs /30µs	[230]
MSM	Au-ZnO-Au	Vapour-phase	-	10 nA (1V, 365 nm, 0.3 mW/cm^2)	<1s/-	[9]
MSM	Al-ZnO	MOCVD	450 nA (5 V)	400 A/W (5V, 373 nm)	1 µs /1.5 µs	[242]
MSM	ITO-ZnO-Au	RF-Sputtering	640 µA (5V)	1616 A/W (5V)	71 ns/377 µs	[243]
MSM	Al-ZnO-Ti	P-MBE	10 mA (5 V)	1.68 A/W (20 V, 374 nm)	95 s/2068 s	[244]
MSM	Al-ZnO-Al	RF-Sputtering	6.7 µA (10V)	2.6 A/W (10V, 370 nm, 1.7 mW/cm^2)	10 ns/960 ns	[245]
p-n	Si-ZnO	RF-Sputtering	-	0.29 A/W (-5V 670 nm, 22mW/cm^2)	35ns/-	[246]
p-n	Si-O-N/ZnO/Pt	Thermal evap.	7.8 µA (-5 V)	152 µA (-5V, 254nm, 8W)	64 s/710 s	[155]
p-n	ITO/ZnO/NiO:Li/ Au	PLD	-	0.3 A/W (-6V, 360 nm, 0.3W/cm^2)	-	[247]
p-n	Ni/ZnO/Si	DC Magnetron sputtering	1 µA (-8 V)	210 A/W (-5V, 390 nm)	0.1 µs/-	[248]
p-n	p-ZnO/n-ZnO	CBD/Sol-gel	5 µA (-3 V)	4 A/W (-3V, 380 nm, 55 µW/cm^2)	-	[236]
MOS	MgZnO-Al	DC Magnetron sputtering	-	0.055A/W (5V, 366nm)	-	[249]

2.3.2.4 Self-powered photodetectors

Nanotechnology has become ever-present in our everyday lives, whether it is used in medical applications, communication devices, storage facilities, sensors or energy-harvesting. In order for these applications to completely function on the nano-scale they required to be self-sustaining, or, for the power source to function on a nano-scale. As the vast majority of previous photodetectors operate at reasonably high applied biases (> 5 V), they require bulky power supplies. This limits the functionality of these photodetectors, for

example in space applications, where mass and long-term sustainability are essential factors. This has led to a recent surge of publications surrounding self-powered photodetectors. The majority of photodetectors that operate at zero-bias use the photovoltaic effect, although a few examples are powered by a nano-scale fuel cell. This section examines some of these devices in more detail and a summary is presented in Table 2-4.

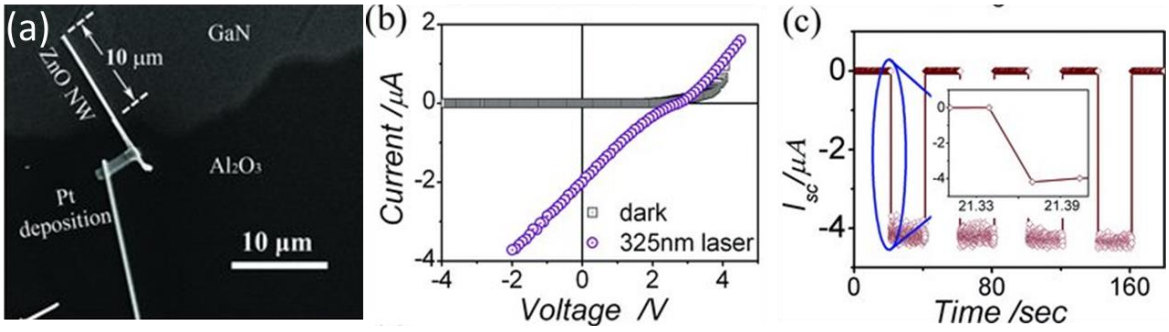

Figure 2.21 a) SEM image of the fabricated n-type ZnO nanowire/p-type GaN film heterojunction. b) I–V curves of the ZnO/GaN heterojunction under dark (square plot) and UV (circular plot) conditions. c) Short circuit current–time curves of the ZnO/GaN heterojunction. Ref. [250].

Bie *et al*. [250] first reported a 'self-powered, ultra-fast, visible-blind UV detection' using ZnO/GaN nano-scale p-n junctions (Figure 2.21a). This was based on the photovoltaic performance of n-type ZnO nanowires on a GaN film, which acted as a photodetector with no applied bias. The photocurrent was ~2 μA under a 325 nm laser irradiance of 100 W/cm^2, which corresponds to a responsivity of 0.5 A/W for the device area shown (Figure 2.21b). The response times of the device were given as τ_r = 20 μs and τ_d = 219 μs. One of the advantages quoted for this nano-scale device is that it required no passivation of the surface in order to stabilise it for an atmosphere environment. In addition, they demonstrated that by integrating the ZnO/GaN junction with a CdSe nanowire (bandgap 1.75 eV), they could produce a selective multi-wavelength photodetector for sensing wavelengths in the region of 650 nm as well as in the UV.

A photovoltaic response at 0 V was measured for a ZnO p-n homojunction using a single n-type ZnO nanowire and As-doped ZnO film [251]. A 325 nm laser irradiance of 50 mW/cm^2 was used to obtain a response of ~1.1 μA. The response times were reported as τ_r = 30 ms and τ_d = 50 ms.

Zhan et al. [252] demonstrated that by decorating the ZnO surface with thermally reduced graphene oxide (rGO) nanoparticles, ZnO could also function as a visible-photodetector. However, the performance of the photodetector remained relatively low with the photocurrent in the nA-range under 80 mW/cm^2 irradiance, and response times of 0.2 s.

One of the recent advances in improving photodetector performance is based on the functionality of the interface between an inorganic semiconductor and a quasi-liquid (gel) heterostructure [253]. A ZnO nanorod-agarose gel heterojunction sensitive to both UV and visible wavelengths exhibited an increase of three orders of magnitude in photoresponse as compared to the ZnO-nanorod array only coated with Pt. Although not specified as a self-powered photodetector the generated photovoltaic effect gives a short circuit current density of 5 μA/cm^2 under 100 W/cm^2 AM 1.5 irradiance, indicating its potential as a self-sustaining device. Response times for τ_r and τ_d were 250 ms and 100ms, respectively.

To provide a broader view of where ZnO-based diodes stand on the scale of self-powered photodetector performance, a comparison will be made with other semiconductors. For example a CdSe nanobelt was shown to exhibit photosensitivity of ~10^5, responsivity of 10.2 A/W and gain of 28 under 633 nm, 2.7 mW/cm^2 irradiance [254]. This responsivity is approximately two orders of magnitude greater than those reported for ZnO, however the response times follow a similar time-scale of τ_r = 82 μs and τ_d = 179 μs.

An alternative to the photovoltaic effect for self-powered photodetectors was presented by Yang *et al.* who integrated a single-fibre hybrid-structured microbial fuel cell to power a CdS nanowire photodetector [255]. This allowed a self-powered multicolour photodetector to obtain a responsivity of 300 A/W; this is up to 10^3 times higher than those achieved with MSM devices or p-n heterostructures.

Table 2-4 A comparison of self-powered photodetectors.

Type	Structure	Growth method	Responsivity/ Photocurrent at 0V	Response times τ_r/τ_d	Ref.
Schottky	GaN/Ti	VPE	0.09 A/W (362 nm, 80 mW/cm^2)	-	[256]
Schottky	CdS:Ga/Au	Thermal evap.	8A/W (510 nm, 0.27 mW/cm^2)	95 μs/290 μs	[257]
p-n	ZnO/GaN/Au	MBE	1μA/W (370 nm)	-	[258]
n-p-n	ZnO/PANI/ZnO	CBD	14 μA (365 nm, 8 W)	-	[259]
Schottky	CdSe/ Graphene/Au/In	Thermal evap.	10.2 A/W (633 nm, 2.7 mW/cm^2)	82 μs/179 μs	[254]
p-n	n-ZnO/p-ZnO	CVD	1.1 μA (30 W/cm^2)	30 ms/50 ms	[251]

2.4 Summary

This chapter provided a detailed background into areas that were relevant to this thesis. An introduction was given to each of the materials used: ZnO, CuSCN, and PEDOT:PSS, detailing their properties, growth methods, and applications. The second part of the chapter reviewed applications for UV photodetectors and the structures currently used as self-powered devices.

ZnO is a wide-bandgap semiconductor (3.3 eV) that typically exhibits n-type behaviour. Multiple growth methods exist for ZnO-nanostructures: thermal evaporation, CVD, MOCVD, PLD, and low-temperature CBD growth (<100˚C), which allows flexible/polymer substrates to be used. The high surface-to-volume ratio of nanostructured ZnO results in surface-related defects having a greater impact on material properties than for thin films. For example, the enhanced photoconductivity exhibited by ZnO nanowires is related to the increased quantity of adsorbed oxygen on the ZnO surface. Furthermore, defects incorporated into the ZnO lattice during low-temperature growth are shown to significantly influence the optical, morphological, and conductive properties of the material. These properties can cause unwanted side-effects in device performance. For instance DLE, caused by defects situated between the ZnO conduction and valence band act as recombination sites for charge carriers; firstly reducing the photoconductivity, and secondly, increase the spectral sensitivity to the visible-spectral region. However, donor-like defects may benefit device performance, increasing the photoconductivity and consequently improve the photocurrent response.

As of yet there are no direct methods to definitively identify defects present in the crystal lattice. EXAFS analysis however, has been used to obtain structural information about the ZnO crystal lattice. In optically-detected mode only information relating to specific

wavelength emissions will be captured. This would provide detailed information regarding the crystal structure surrounding specific emission centers, and may assist in identifying the defect present.

CuSCN is an inorganic wide-bandgap (3.6 eV) p-type semiconductor that can be deposited using impregnation, electrochemical deposition, or SILAR techniques. Difficulties arise with pore-filling of nanostructures due to the large grain-size of electrochemically and SILAR deposited CuSCN. 'Mud-cracking' of CuSCN is common in the case of impregnation, and is due to the slow evaporation of solvent from the CuSCN grains. Although CuSCN demonstrates chemical stability, reasonable hole conductivity, radiation hardness, and optical transparency to the visible spectra, the difficulties in effective deposition and thickness control has often caused this material to be dismissed in favour of an alternative.

PEDOT:PSS is an aqueous soluble conductive polymer used as a hole collector in electronic devices. The PEDOT:PSS HOMO and LUMO are separated by 0.6 eV at equilibrium, and 1.5 eV under applied bias. This is due to the rapid redox reaction taking place at the metal-polymer interface causing a chemical reaction that is reported to increase the optical bandgap. The ease of deposition, good hole conductivity and transparency to wavelengths >450 nm, has led to PEDOT:PSS being used to fabricate various hybrid inorganic/organic heterostructures for piezoelectric energy-harvesting, optoelectronics, and chemical sensors.

Multiple device structures exist for UV photodetectors (MSM, MIS, Schottky, photoconductor, p-i-n, p-n etc.). Employing wide-bandgap semiconductors as part of the structure provides a natural filter to visible wavelengths and allows the device to operate at RT. This makes UV photodetectors suitable for high-temperature and high-power applications. However, photodetectors that require a high bias to achieve reasonable photocurrent response are not capable of functioning on the nano-scale; this is due to the large components associated with providing the necessary output. Instead, self-sufficient photodetectors would be advantageous to applications that are limited by mass, size, energy storage, or portability. Important parameters in determining the effectiveness of self-powered photodetectors are: spectral sensitivity, responsivity, and rise/decay times.

3 Experimental

3.1 Synthesis and device fabrication

3.1.1 ZnO seed layer deposition

Transparent conductive oxide-coated (TCO) glass was supplied pre-coated with either indium-doped tin oxide (ITO) or fluorine-doped tin oxide (FTO) (15 Ω/square). These were used as substrates for the seed layer and eventual nanorod array. These substrates were cut to size using diamond-tipped glass cutters on the non-conductive side. They were then cleaned thoroughly to ensure the removal of any contaminants from the surface. This was done by placing them in beaker with acetone and sonicating them in an ultrasonic bath for 15 minutes. They were removed from the acetone and rinsed with isopropanol (IPA) before being placed in a beaker with IPA and sonicating again for 15 minutes. The substrates were removed and dried with nitrogen.

The substrates were then placed TCO-side up and rinsed with GPR-grade ethanol and dried with nitrogen. This was found to assist wetting of the surface with the seed solution. All the reagents involved in this experiment were of analytical grade and used as received without further purification. A 0.005 M solution of zinc acetate dihydrate (Sigma Aldrich ≥ 98%) in absolute ethanol (purity > 99.7%) was used for the seed solution. The solution was sonicated for 20 minutes to assist dissolution and then kept for 1 h before being deposited. The solution was deposited drop-wise on the TCO and left for 10 seconds before being rinsed generously with GPR-grade ethanol and dried with nitrogen. This was repeated five times to ensure enough zinc acetate adhered to the surface. The substrates were then placed in the centre of the hotplate and annealed at 350°C for 25 minutes. Once the substrates cooled to room temperature (RT) the process of seed deposition and annealing was repeated two more times. This ensured a good coverage of ZnO particles were adhered to the TCO surface and ready to act as nucleation sites for nanorod growth.

3.1.2 ZnO aqueous chemical synthesis

A chemical aqueous solution was used to grow ZnO nanorods onto the TCO substrates. The pre-seeded substrates were suspended TCO face-down in the aqueous solution using a

polytetrafluorine (PTFE) stand and secured in place with a glass slide and PTFE-coated wires. The aqueous-chemical synthesis was performed in a sealed glass vessel placed in a (Town and Mercer) conventional oven set to 90˚C (see Figure 3.1). When placing the substrates into the chemical solution it was essential to ensure there were no air pockets trapped beneath the stand. This would inhibit the solution from contacting the substrate and consequently prevent heterogeneous ZnO growth from the seed layer. The temperature of the solution was monitored using a Type-K thermocouple and the pH was measured using an YSI pH Metre Kit (pH Range 0 to 14.4 M).

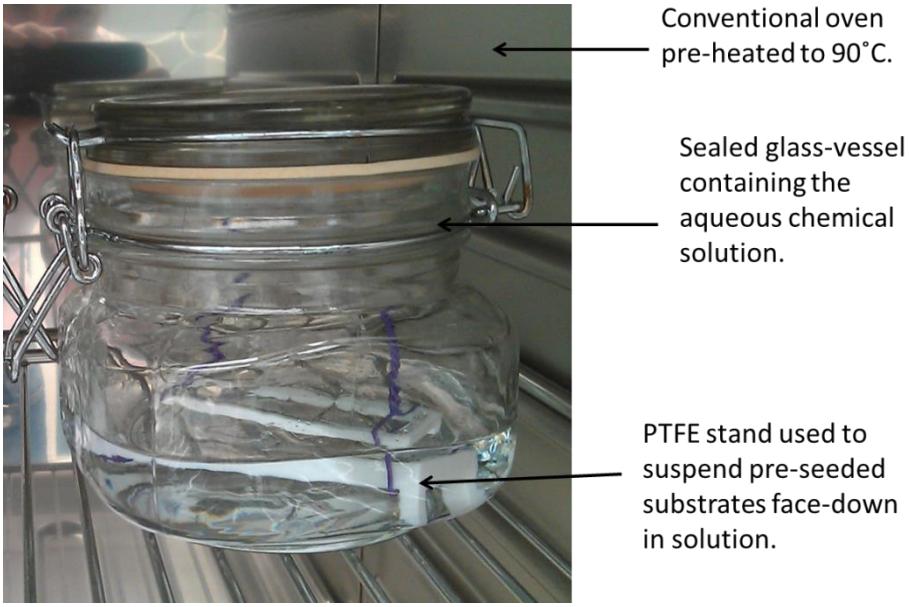

Figure 3.1 Photograph of the set-up used for ZnO nanorod growth using an aqueous chemical solution.

Factors that influence the material properties were investigated and are outlined below:

- Growth on FTO, ITO, and glass substrates.
- The effect of a pre-seeded substrate as opposed to non-seeded.
- The influence of precursor concentration on ZnO growth.
- Substrate stands (made of PTFE and acrylonitrile butadiene styrene (ABS)) was shown not to influence the growth.

Experimenting with precursor concentrations of alkaline reagents [hexamethylenetetramine (HMT/ $(CH_2)N_4$) and/or ammonia hydroxide] and zinc nitrate hexahydrate ($Zn(NO_3)_2).6H_2O$) led to nanorods with varying diameters, lengths and densities. One particular solution presented nanorods with interesting material properties that warranted further investigation.

Consequently, the project focus was altered to accommodate this and further analysis was then performed on nanorods synthesised using this (pH 11) solution.

The majority of the project focuses on ZnO nanorods grown using two synthesis solutions and are distinguished by their pH: pH 6 and pH 11.

The pH 6 synthesis consisted of an equimolar 0.0025 M solution of zinc nitrate hexahydrate and HMT, with a total volume of 250 mL. Synthesis solutions were made using de-ionised water with purity of 18.2 MΩ. The solution was placed in a pre-heated oven at 90˚C for 2.5 h. The synthesis was repeated six times using a fresh solution each time to acquire the desired nanorod length.

The pH 11 synthesis comprised of 15 mL of 0.2 M zinc nitrate hexahydrate (Sigma Aldrich 99+%) solution (18 mM), 15 mL of 0.8 M hexamethylenetetramine (HMT) (Sigma Aldrich 98%) solution (73mM) and 135 mL of 0.2 M ammonia hydroxide solution (0.163 M) and resulted in a final solution pH of 10.9. This solution was placed in the pre-heated 90˚C oven for 4 h and the process was repeated up to eight times with fresh solutions.

In both cases, the stands and substrates were thoroughly rinsed with de-ionised water to remove any adhered precipitate after each synthesis. This minimised the precipitate transferred to the next solution and removed any large agglomerates attached to the top of the nanorod array. When the final synthesis was completed, the substrates were carefully removed from the stand, rinsed with deionised water, and dried with nitrogen gas.

Before the glass vessels were re-used they were thoroughly cleaned with hydrochloric or nitric acid and rinsed with de-ionised water. The same process was followed for the stands and glass slides.

3.1.3 Thermal annealing of ZnO

Annealing of the nanorods took place in a tube furnace (Lenton Type 3216CC) that allowed selected gases (air, nitrogen or oxygen) to flow over the substrate surface at a flow rate of 0.5 L/min. The selected gas was allowed to flow through the tube furnace for up to 15 minutes before starting the anneal process. The duration and temperature of the anneal

process was varied as required and the ramp rate was set to 3˚C/min. Samples were left to cool unassisted in the furnace until they reached RT before being removed.

3.1.4 P-type deposition

Prior to depositing any p-type materials an intermediate-step was required to insulate the TCO-exposed sides of the substrate. A glass pipette was used to deposit a 10 wt.% solution consisting of M_w 120000 poly(methyl methacrylate) (PMMA) in anisole along the FTO-exposed substrate edges. The samples were then placed on a hotplate at 50˚C to dry for 2 minutes. A multi-meter was used to ensure the TCO-edges were properly insulted, otherwise the process was repeated. This was performed instead of etching the TCO from the glass as it proved more effect when preventing shorts from occurring in the device.

3.1.4.1 Copper (I) thiocyanate (CuSCN)

During this project attempts were made to improve the CuSCN layer. This consisted of developing a new deposition technique, and optimising the process in terms of drying periods, different concentrations (0.1-0.2 M), and quantity deposited after each drying interval. This required testing numerous devices and in order to reduce inconsistencies across the range of samples, it was ensured that comparisons were made with simultaneously synthesised nanorods.

Two new deposition techniques were developed and tested: the spray deposition and the spin-coat method. The experimental methods are detailed below:

Spray-deposition technique

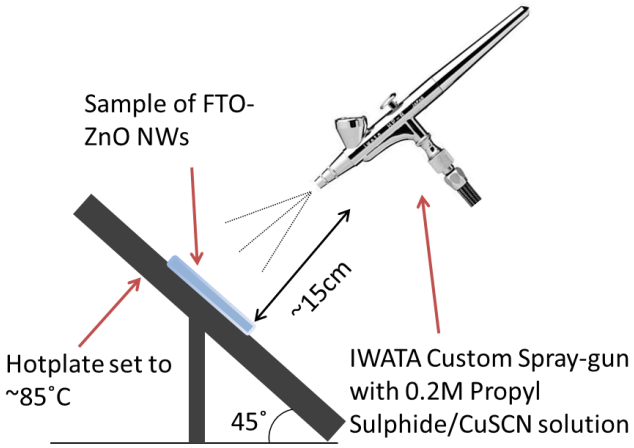

Figure 3.2 Schematic showing the spray-deposition of CuSCN using a pneumatic IWATA Custom-Micron C spray gun.

This deposition of CuSCN involved using a (IWATA Custom-Micron C) pneumatic spray gun with a narrow 0.2 µm nozzle. The nozzle opening could be varied to control the spread of the spray; in this case it was set to 2 on the first turning. The attached air-compressor was used to determine the pressure applied to the spray gun. A saturated solution of CuSCN was produced using 0.200g dissolved in 10ml n-propyl sulphide. The solution was stirred for up to 24 hours at RT before leaving the needle-like crystal precipitate to settle for a further 24 hours. Substrates coated with the ZnO nanorods were placed on a hotplate at 85-95˚C and maintained at this temperature throughout the deposition (see Figure 3.2).

Approximately 1 mL of CuSCN solution was placed into the cup of the spray gun and a micro-fine mist was deposited at a pressure of 0.1 MPa for 10-20 second intervals using a sweeping side-to-side motion. The n-propyl sulphide solvent can be harmful if inhaled and so for safety measures the experiment was conducted in a fume hood. This ensured an even coverage over the entire surface. The solution was given 1-3 minutes to fully evaporate until the propyl-sulfide solvent was not detected olfactorily. The process was repeated until a smooth, shiny layer was observed over the entire area, or when the sample was completely transparent to the naked eye. This is dependent on the porous volume that requires filling, but on average 2 µm long nanorods requires approximately 5-10 coatings (and takes between 10-15 minutes).

The morphology of 25, 50, 75, 100, 125, and 150 spray-deposited CuSCN layers was analysed to obtain the optimal thickness.

To ensure no bare ZnO nanorods were exposed between the PMMA and CuSCN when the electrode was deposited, the edges were re-coated with PMMA.

Spin-coating technique

For this method the ZnO nanorod coated substrate was attached to the rotational disc in the (TC100 MTI corporation) spin-coater using double-sided sticky tape. A heat lamp positions ~20 cm above the sample was used to maintain sample temperature at ~80˚C. The 0.2 M CuSCN solution was deposited drop-wise onto the sample that was rotating at speed of 1000 rpm. Up to 20 drops were placed at 20 s intervals to completely coat the ZnO array.

Impregnation technique

This is a popular technique used for the deposition of CuSCN and was used in this project as a comparison for the new methods that were developed.

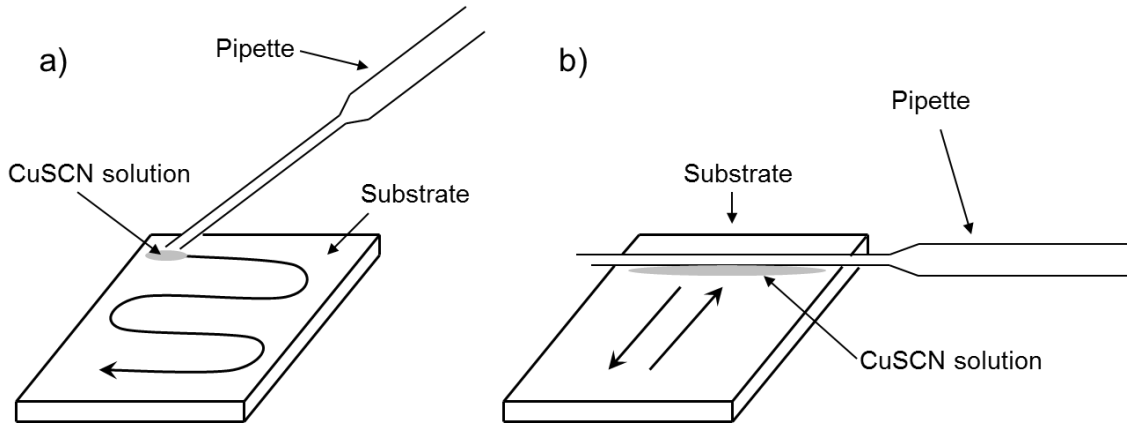

Figure 3.3 Schematic of the two methods used to deposit of CuSCN via impregnation, a) using the pipette-tip and b) using the pipette-edge. (Supplied by Joe Briscoe PhD)

The concentration of CuSCN solution remained identical to that used in the micro-spray method (i.e. fully saturated). The sample was placed on a hotplate between 80-90˚C. Impregnation was performed by suspending a droplet of CuSCN solution either on the edge or tip of a glass pipette. It was positioned so that the droplet was barely in contact with the surface and then moved across the surface to coat the sample as shown in Figure 3.3. After the first coating the sample was left for up to 5 minutes to evaporate the solvent before the next layer was deposited. Additional heating stages were introduced to improve the deposition: after every 5 layers the sample temperature was increased to 150˚C for 10 minutes before returning to the deposition temperature.

3.1.4.2 PEDOT:PSS

Aqueous PEDOT:PSS solution was deposited onto the ZnO nanorods using a TC100 MTI corporation spin-coater. The samples are secured in place with double-sided sticky tape. The rotational speed was varied from 500-3000 rpm and it was found to give a smooth even coating at 2000 rpm. Hence, the speed was maintained at 2000 rpm for 1 minute while ~0.5 mL PEDOT solution was deposited in a steady stream above the centre of the substrate. The sample continued to spin for up to 30 s after deposition; this allowed any excess PEDOT solution to spin-off from the edges and assisted in the drying process before handling. After coating the sample it was placed on a hotplate at 120°C for 2 minutes to remove any residual solvent from the conductive polymer and improved adherence to the nanorod structure. One-coating was usually sufficient, however occasionally a second coating was deposited if the film thickness appeared too thin.

In attempt to improve the PEDOT:PSS penetration into the nanorod array, it was thought this could be achieved by simply diluting the aqueous PEDOT:PSS. Therefore, dilutions of PEDOT:PSS in acetone (1:5 and 1:10 volume ratios) were used to investigate the effect on PEDOT:PSS penetration.

3.1.5 Electrode deposition

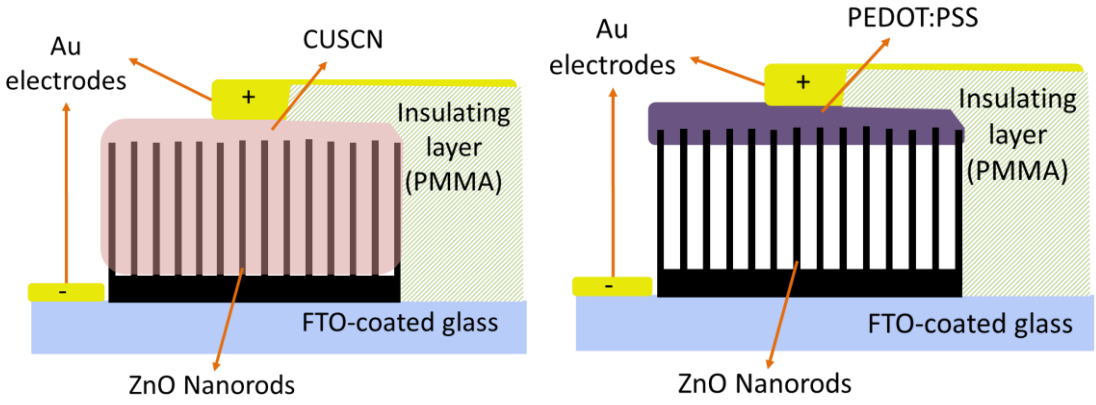

Figure 3.4 Schematics of the final devices a) ZnO-CuSCN and b) ZnO/PEDOT:PSS.

A steel template created a mask during the sputtering process and determined the electrode size. When the Agar Auto Sputter Coater reached a chamber pressure of < 0.1 mbar, gold was sputtered for 30 s onto the surface. The process was repeated twice to obtain a suitable

thickness of ~100nm. Schematics of the completed ZnO-CuSCN and ZnO-PEDOT:PSS devices are shown in Figure 3.4.

3.2 Characterization

3.2.1 Scanning electron microscope

Morphological analysis was conducted using an FEI Inspect-F scanning electron microscope (SEM) operating at 20 kV. Samples were mounted onto steel stubs and carbon tape was used to secure the sample in place as well as provide a good conductive pathway to prevent charging of the sample surface. Images were obtained either top-down, or by tilting the stage 45˚ for cross-sections.

3.2.2 Transmission Electron microscopy

A JOEL 2010F transmission electron microscope (TEM) operating at 200 kV was used to study the ZnO nanorod morphology using bright- and dark-field imaging. Selected area electron diffraction (SAED) patterns were obtained to examine the crystallography of the ZnO. This analysis was performed on nanorods that had been scraped from the TCO substrate into a vial of GPR-grade ethanol (supplier VWR). This was sonicated for 5 minutes before depositing 1-2 drops of the suspension onto a Cu TEM grid.

3.2.3 X-ray diffraction & Glancing incidence XRD

The X-ray diffraction (XRD) analysis was performed with an X'Pert PRO MPD θ-2θ System in θ-2θ Bragg-Brentano configuration with a diffracted beam monochromator. Glancing incidence XRD (GIXRD) was performed with a Siemens D500 using CuK_{α} radiation (λ = 0.1540 nm) under a glancing angle configuration of 3˚ with 2-D sample rotation. Samples were examined as a thin-film on the substrate surface without any special treatment.

3.2.4 Optical absorption

The UV-Vis absorption spectra of samples were collected using an integrating sphere in connection with a Perkin Elmer Lamba 950 spectrometer. Samples were mounted with the ZnO-CuSCN surface facing the light source to minimise the reflection that would otherwise occur from the smooth glass surface.

3.2.5 Photoluminescence

Photoluminescence (PL) spectroscopy was performed at RT using a micro-Raman system in co-ordination with a He:Cd CW laser Triax 320 (325 nm excitation, 1200/1 mm grating, 30 mW output power). Samples were laid flat ~1 cm beneath an emitter-detector bundle optic cable. The experiment was performed in a darkened laboratory to minimise the influence of external light sources. The laser-bulb was left to warm-up for up to an hour to ensure the illumination intensity would remain stable during the experiment. Scan rates were performed at 1 nm/s for the wavelength range 350-800 nm.

3.2.6 Photovoltage measurements

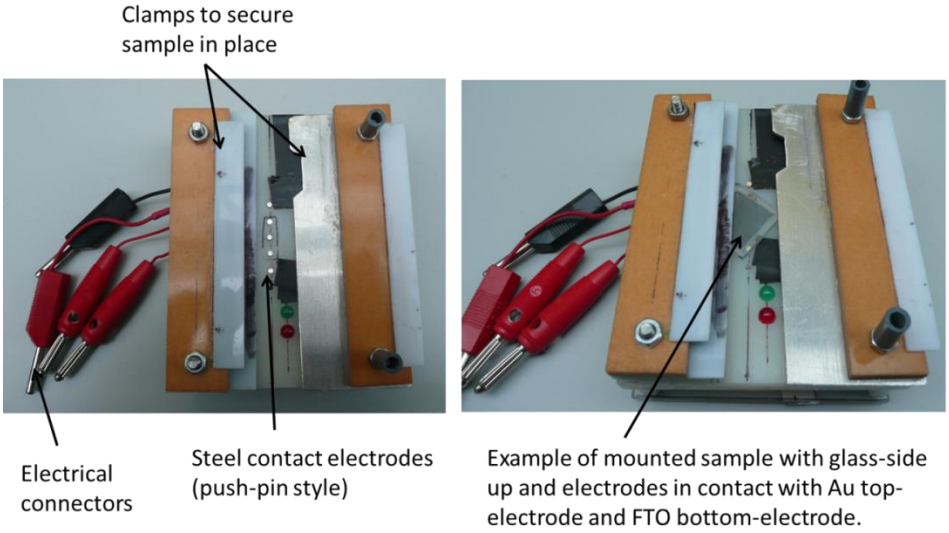

Figure 3.5 Photographs of the mounting used when electrically testing the devices.

Photo-voltage measurements were conducted using an Nd-YAG 325/532 nm 5 ns pulsed laser with a 1 MΩ resistance connected in series with the device. The samples were mounted face-down in a clamp-style set-up that was used for all electrical measurements (see Figure 3.5). This required the laser pulse to first penetrate the FTO-coated glass before reaching the p-n- heterostructure. The intensity of the 4 Hz 325 nm and 532 nm pulse was measured as 0.3 μJ/pulse and 0.1 mJ/pulse, respectively.

3.2.7 Raman spectroscopy

Raman scattering measurements were performed using a Renishaw inVia monochromator equipped with CCD detector and an Nd-YAG 473 nm excitation source. The data for each

sample was averaged over 30 acquisitions, each with an exposure time of 10 s. Long-range and short-range scans were performed.

3.2.8 Hall Effect measurements

Hall measurements were conducted to determine the carrier mobility, charge concentration, and establish the majority carrier. Hall Effect measurements were conducted using the Van der Pauw method. Square glass substrates were cut to 1 cm^2 pieces and clean thoroughly using isopropanol and acetone in an ultrasonic bath. ZnO-nanorods were grown onto the glass substrates using a seed layer. Only the bulk ZnO layer at the base of the nanorod contributes to this measurement as the charge carriers cannot traverse across the porous array. The CuSCN layer was also measured to investigate how the resistivity varies for across thicknesses (700nm – 6 μm).

Four (right-angle triangle) gold contacts measuring 0.02 cm^2 were sputtered onto each corner using a mask as a template. The sample was then mounted using silver paint onto a printed circuit board that had been etched using $FeCl_3$ to create four Cu electrodes. Hall mobility was calculated from an average of five measurements with the compliance voltage set to 5 V, a measuring current of 1.6 μA and magnetic field of 0.5 T.

3.2.9 Electrical measurements

Current-voltage (I-V) characteristics of the devices were obtained via a Keithley 2400 source meter controlled using Labview 8.2 software. The I-V sweep was conducted at RT under dark, UV illumination, or solar simulated (Newport) conditions using an A.M 1.5 filter. UV illumination consisted of a 380 nm wavelength light emitting diode (LED) positioned ~1 cm directly above the sample. The output power for the 380 nm UV LED was measured using an International Light Technologies ILT14000-A Radiometer Photometer. The intensity of the solar simulator was maintained at a constant power source of 200 W, which corresponds to an irradiance of ~1 sun (100 mW/cm^2).

I-V tests were repeated over time to examine the stability of PEDOT:PSS and CuSCN devices. Multiple contacts were deposited on the active area and each was tested to ensure consistency across the device.

For self-powered photocurrent measurements, the Keithley 2400 applied bias was set to equal zero. The LEDs were sourced from RS Components (640 nm, 588 nm, 525 nm, 470 nm) and Thorlabs (405 nm and 380 nm). The visible LEDs irradiances were measured and calibrated using an Ocean optics spectrometer. A range of intensities between 0.8-6.0 $mWcm^{-2}$ were used to obtain the photocurrent measurements. The LEDs were positioned ~1 cm directly above the device in an enclosed chamber and powered by Rapid DC power supply HY3003D.

3.2.10 Extended x-ray absorption fine structure (EXAFS)/ X-ray excited optical luminescence (XEOL)

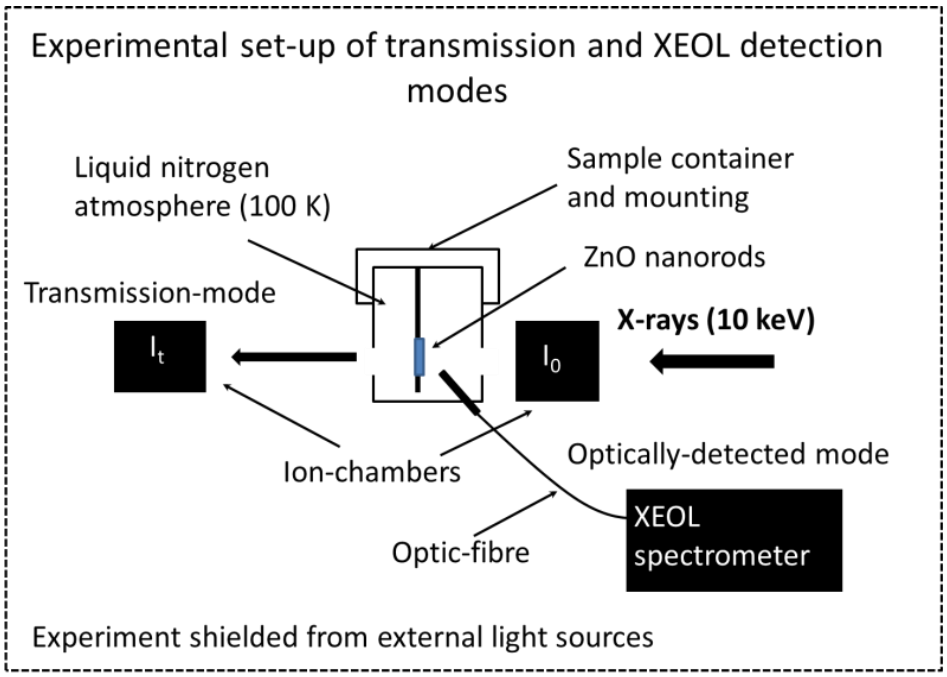

Figure 3.6 Schematic of the experimental set-up for detecting EXAFS emission in transmission and fluorescence (XEOL) modes.

The schematic of the experimental set-up (Figure 3.6) demonstrates the two modes used in our experiments: standard transmission mode (TM) and optically-detected mode (OM).

EXAFS experiments at the Zn *K*-edge were conducted at the Diamond Light Source (DLS) B18 beam-line. An ion-chamber positioned behind the specimen detected X-rays transmitted through the specimen and provided the EXAFS for TM. The optically detected signal was collected using an optic fibre offset at angle in front of the specimen to capture photons for

OM. The detection system consisted of a Triax 180 spectrometer equipped with Synapse CCD and a Newport VIS Femtowatt photoreceiver. Liquid nitrogen was used to maintain a specimen temperature of 100 K. Two deep-level emissions were analysed in OM: 500 nm and 660 nm. For transmission mode the X-rays were not able to penetrate the ITO-coated glass and so the ZnO nanorod film was peeled from the substrate using Kapton tape and examined thus. In OM the ZnO samples were examined on the ITO-coated glass.

ATHENA software (part of the SIXPACK software package) was used to perform the preliminary analysis and subtract background (R_{bgd} = 1.0) from the collected EXAFS data. The EXAFS data in the *k* range or 2.0 to 11.6 $Å^{-1}$ were used for analysis. In order to visualise the atomic structure and relative bond-lengths from the absorbing atom, the EXAFS data was Fourier transformed (FT) to *r* space [260]. The ARTEMIS software package used FEFF calculations to provide theoretical fits in *r* space for range *r* = 1.0-3.2 Å. The a number of parameters were used in adjusting the fit to obtain the atomic bond lengths, these included: the amplitude factor (S_0^2), which was varied to determine information on the local occupation numbers (N) and the Debye-Waller factor (σ^2), which represents the thermal vibrations and static disorder in the lattice.

4 ZnO nanorod synthesis and characterisation

Reviews on aqueous chemical growth solution have demonstrated that a number of factors influence ZnO growth, as discussed in Chapter 2. This project required the successful fabrication of ZnO nanorod arrays before further experimentation could take place. Therefore, a well-established method first reported by Vayssieres et al. [44] was chosen to demonstrate the aqueous solution process could be performed successfully with repeatability. This process was labelled the pH 6 synthesis (so-named for the initial pH of the solution) and is detailed in the experimental 3.1.2. Once it was established that the aqueous method could be performed successfully, the alkaline solutions (HMT and ammonia hydroxide) and zinc nitrate hexahydrate concentrations were varied to monitor the effects on morphology. During this project, ZnO nanorods prepared using a pH 11 solution (see section 3.1.2) presented interesting photoluminescence properties and warranted further investigation. Consequently, the effect of processing on the ZnO properties was primarily focused on these unusual pH 11 grown nanorods. A detailed analysis of the ZnO morphology, crystallography, and optical properties was performed, with special attention given to the effect of anneal atmosphere.

The pH 11 grown nanorods were shown to exhibit green photoluminescence, which provided the opportunity to collect high-quality EXAFS spectra in optically-detected mode (see section 3.2.10). Primarily the aim of using this technique was to prove it could distinguish between different regions in the crystal lattice, and secondly, to gain further understanding regarding the origin of defect emissions.

4.1 Aqueous chemical growth

4.1.1 Initial growth analysis

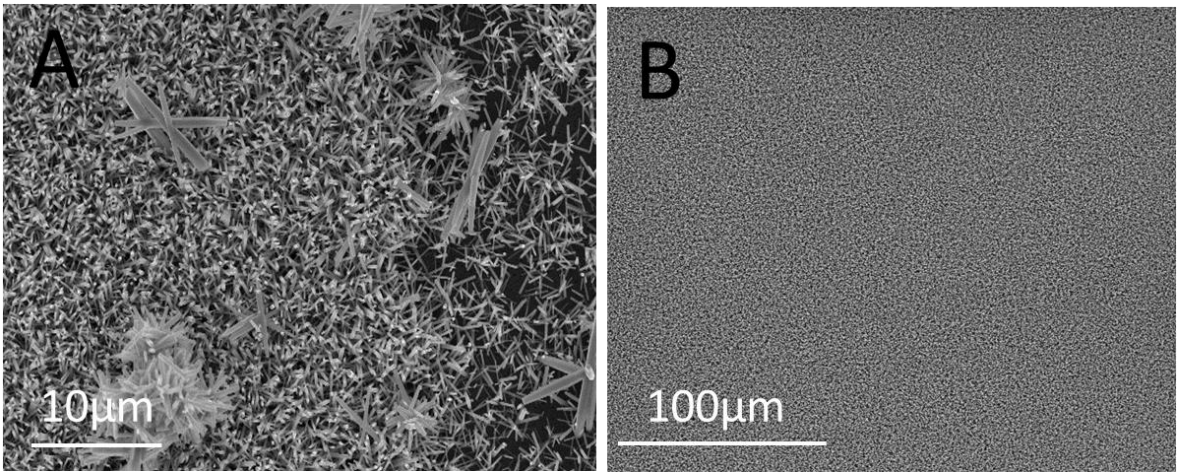

Figure 4.1 SEM top-down view of ZnO nanorod arrays showing A) agglomeration of large nanorod clusters on the array and B) a ZnO nanorod surface free from nanorod clusters.

Initial attempts to grow ZnO nanorod arrays often led to inconsistencies on the substrate surfaces that were visible to the naked eye. On closer inspection using SEM analysis, it was found that large agglomerations of nanorods formed clusters on the array and areas exist where little or no growth occurred (Figure 4.1A). It was proposed that these larger nanorods form homogeneously in solution and agglomerate to create clusters. These clusters attach to the surfaces of the stand and substrate when removed from the solution. This occurs each time the stand was removed and placed into a fresh solution. This was resolved by thoroughly rinsing the stand and substrate surface with de-ionised water after each synthesis to minimise the nanorod clusters on the surface. The areas with minimal growth observed on the right of Figure 4.1A could be linked to multiple factors; damaged or unclean TCO surface, ineffective seed-layer deposition, or air-pockets trapped beneath the stand during growth. These factors were addressed in turn by carefully monitoring that each processing step was performed with care and precision. This eventually resulted in the fabrication of a consistent, clean nanorod array as shown in Figure 4.1B.

4.1.2 Precursor concentrations

Precursor concentration, pH, and capping agents are reported to affect the morphology of the ZnO and create various nanostructures [57,261]. The ability to influence the ZnO

morphology is highly beneficial for applications that require high surface-to-volume ratios, or particular mechanical attributes, e.g. flexibility. The initial aim was to synthesise long, thin nanowires using zinc nitrate, HMT and/or ammonia hydroxide. A number of different solutions were used and examples of these are given here: solution A (0.02 M zinc nitrate in 0.18 M ammonia hydroxide), solution B (0.01 M zinc nitrate, 0.07 M HMT in 0.16 M ammonia hydroxide), solution C (0.02 M zinc nitrate, 0.05 M HMT in 0.16 M ammonia hydroxide) and solution D (0.02 M zinc nitrate, 0.07 M HMT in 0.16 M ammonia hydroxide, the pH 11 synthesis).

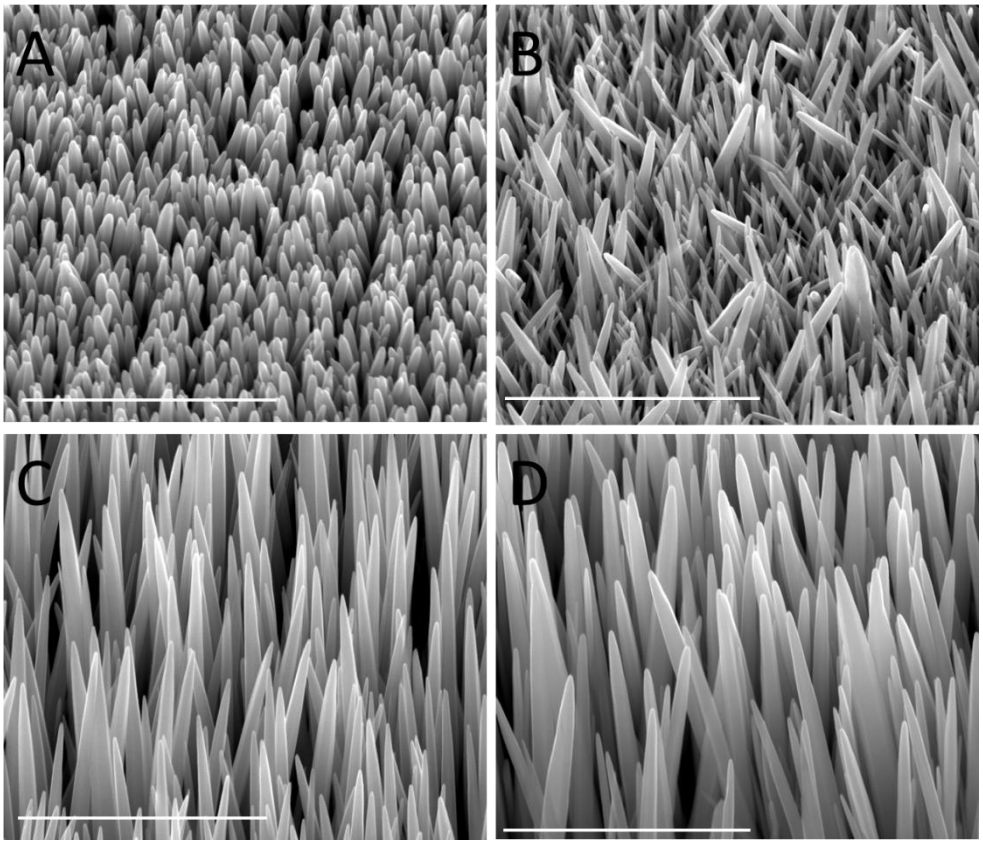

Figure 4.2 SEM images (obtained at a 45˚ tilt) of ZnO nanorods prepared using various precursor concentrations solutions: A) A, B) B, C) C, and D) D (scale bars - 3 µm).

The morphology of the nanorods grown using solutions A-D was analysed using the SEM (Figure 4.2A-D). The absence of HMT in solution A resulted in a dense array of stubby nanorods with rounded tips (Figure 4.2A). Solution B generated an array with a lower nanorod density causing increased misalignment (Figure 4.2B). This behaviour was assigned to the partial dissolution of the seed layer prior to reaching the growth temperature. Solution C and D produced arrays with similar density, alignment, and aspect ratios. However, only solution D resulted in the unusual photoluminescence characteristics that led to further

analysis being performed. Although a number of samples were produced using concentrations of 28-32% ammonia, only the high purity 32% ammonia would result in the unusual nanorod properties presented here. Hence, it was shown that the purity of ammonia hydroxide was critical to the synthesis process.

4.1.3 Substrate and seed-layer analysis

Glass, ITO, and FTO substrates both seeded and non-seeded, were used to demonstrate the effect on nanorod density and alignment. Eight four-hour pH 11-syntheses were used for each sample set.

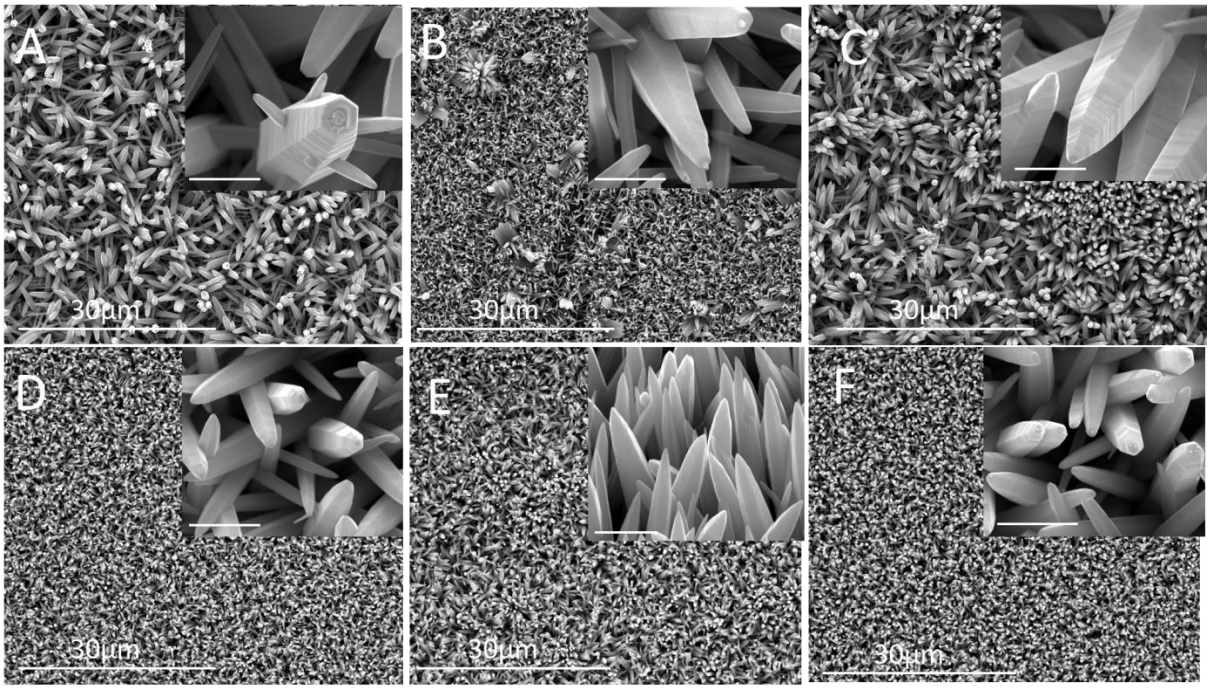

Figure 4.3 SEM images of ZnO nanorods on non-seeded A) ITO-coated glass, B) plain glass, C) FTO-coated glass, and pre-seeded D) ITO-coated glass, E) plain glass, F) FTO-coated glass. Inset scales bars are 1 µm.

Comparing the non-seeded (Figure 4.3A-C) and seeded substrates (Figure 4.3D-F), confirms the seed layer is necessary for improved alignment and consistent nanorod diameter. Non-seeded substrates typically display nanorods with larger diameters and growth along the twin planes (see inset Figure 4.3A). The seeded glass, ITO, and FTO substrates do not appear to exhibit significant differences between their morphology. This suggests the seed layer has stronger influence on ZnO growth than the surface-roughness of the substrate.

4.2 Growth mechanisms and experimental observations of aqueous-grown nanorods

In this section, HMT and/or ammonia hydroxide, and zinc nitrate ($Zn(NO)_3$) were used to create an alkaline pH 11 solution and a weakly acidic pH 6 solution. HMT is reported to act as a pH buffer that gradually decomposes to supply ammonia and hydroxyl ions to the reaction (eq. 1 & 2) [47,50,52]. Production of ZnO occurs via the equilibrium reactions shown in eq. 3 & 4 for pH 6 solutions and eq. 5 & 6 for pH 11 solutions [262]. This indicates that once the Zn-precursors are exhausted, dissolution of ZnO will initiate. The chemical reactions for the aqueous synthesis at 90˚C are given as [47]:

$$(CH_2)_6N_4 + 6H_2O \xrightarrow{\Delta} 6HCHO + 4NH_3 \quad (1)$$

$$NH_3 + H_2O \leftrightarrow NH_4^+ + OH^- \quad (2)$$

$$Zn^{2+} + 2OH^- \leftrightarrow ZnO + H_2O \quad (3)$$

$$Zn(NH_3)^{2+} + 2OH^- \leftrightarrow ZnO + NH_3 + H_2O \quad (4)$$

$$Zn(OH)_4^{2-} \leftrightarrow ZnO + H_2O + 2OH^- \quad (5)$$

$$Zn(NH_3)_4^{2+} + 2OH^- \leftrightarrow ZnO + 4NH_3 + H_2O \quad (6)$$

The reaction for the pH 11 synthesis takes significantly longer than the equimolar pH 6 syntheses. This was inferred from the duration of solution turbidity that indicates the homogeneous formation of ZnO in the solution. The reaction nears completion when the solution becomes transparent again. This leaves behind white powdered precipitate at the bottom of the reaction vessel as a result of the homogeneous reactions taking place. In the case of pH 11 syntheses, only a thin well-adhered film remained on the side of the glass vessel, with minimal precipitate present. This is in contrast to the equimolar pH 6 synthesis, which left significant amounts of precipitate at the base of the vessel. This observational difference indicates homogeneous growth was restricted for high pH, whereas homogeneous growth was favoured for the lower pH 6 synthesis.

The rate of reaction for this synthesis can be expressed as:

$$r = k[HMT][Zn(NO_3)_2] \quad (7)$$

For pH 6 aqueous solution: r = [0.025][0.025] = 0.0063

For pH11 aqueous solution: r = [0.073][0.018] = 0.0013

This shows the rate of reaction was five times quicker during the pH 6 syntheses than during the pH 11 synthesis. However, reaction rate does not determine the growth rate of the nanorods, simply the rate at which ZnO was formed in the solution. The growth mechanism i.e. homogeneous/heterogeneous growth is what governs the nanorod growth from the pre-seeded TCO-substrate. The increased HMT concentration in the pH 11 solution acts as a pH buffer and ensures the solution maintains its high pH throughout the synthesis. This restricts homogeneous growth of ZnO particles in solution and conserves the Zn-precursors for heterogeneous nanorod growth.

4.3 Morphology

The positive polar face (0001) preferentially adsorbs $OH^-/Zn(OH)_4^{2-}$ ions to the surface before they dehydrate and enter the crystal lattice. As the non-polar faces of the wurtzite structure have a significantly lower surface energy than the positive (0001) plane, this gives rise to the anisotropic growth of ZnO in the c-axis direction. Rapid preferential growth on (0001) plane is indicated by tapering of the edges and the formation of needle-like tips [59]; furthermore, this plane also dissolves fastest under reverse equilibrium, forming ZnO nanotubes [47,263]. If the synthesis is incomplete, remnant Zn-precursors exist both in the solution and on the nanorod surface.

In the following section, SEM analysis was used to examine the morphology at different stages of growth, and post-annealing in various atmospheric conditions.

4.3.1 Synthesis analysis

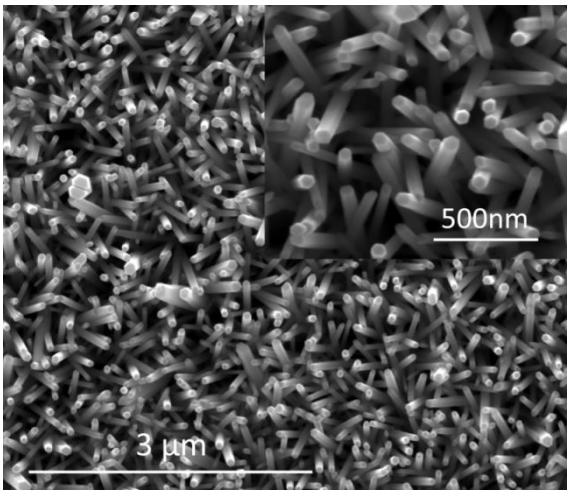

Figure 4.4 SEM micrograph of ZnO-nanorods synthesised using six 2.5 h repeats in aqueous pH 6 solution, inset shows enlarged top-down view of the nanorods.

The pH 6 synthesis results in hexagonal columns 1.5-2 µm in length and 50-80 nm in diameter, giving a minimum aspect ratio of 1:20. The nanorod length was estimated due to the difficulty in obtaining clean-cut cross sections of the substrate without damaging the nanorods. The nanorod tips are flat with a hexagonal-shape (Figure 4.4 inset). This indicates the heterogeneous growth rate was slow enough to allow well-structured crystals to form. Figure 4.4 shows a relatively high-density of unaligned/disordered nanorods with a good coverage across the substrate surface.

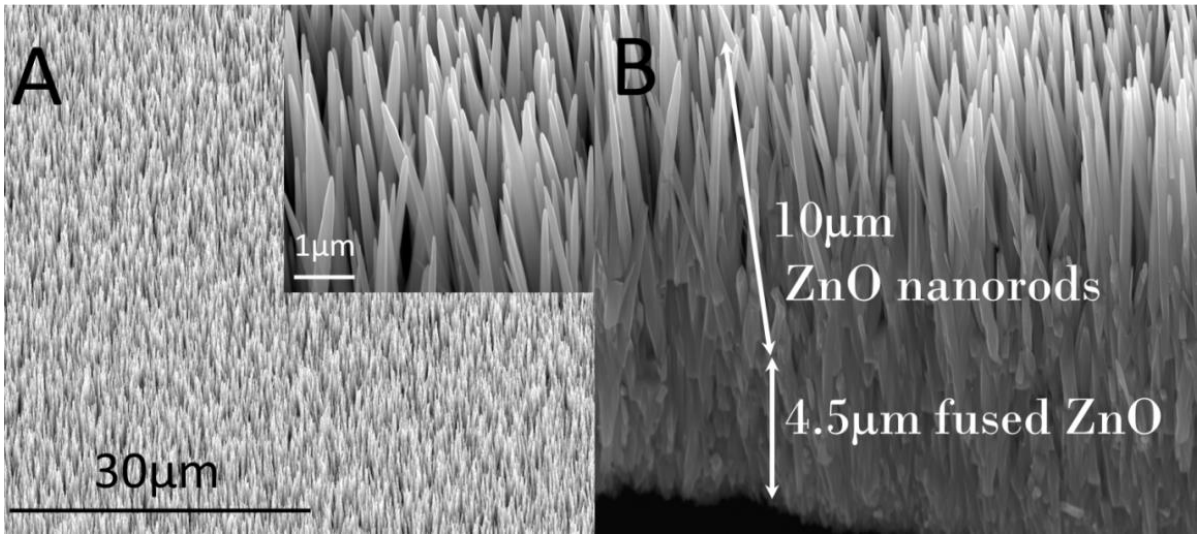

Figure 4.5 SEM micrographs of ZnO-nanorods synthesised using eight 4 h repeats in aqueous pH 11 solution. A) A 45˚ tilted view of the nanorod array, with the inset showing a magnified view of the nanorod tips. B) A cross-section of the nanorods array showing a fused ZnO layer at the base.

The pH 11 synthesis resulted in a high density of well-aligned nanorods (see Figure 4.5a). The inset of Figure 4.5a highlights the difference in tip morphology; where the pH 6 tips were flat and hexagonal, the pH 11 nanorod tips are tapered. This indicates an incomplete synthesis reaction and rapid growth along the c-axis. The improved alignment of the nanorod array is explained using the cross-sectional SEM micrograph (Figure 4.5b). At the base of the array there exists a bulk layer of fused ZnO nanorods of all orientations. Only nanorods orientated along the c-axis are able to grow with minimal obstruction, resulting in the ordered array. Nanorod lengths range between 12-15 µm including the fused ZnO layer at the base, diameters range from 100-300 nm due to the long tapering tips. This gives a minimum aspect ratio of 1:40.

The initial stages of growth were studied to assess whether the difference in morphologies could be linked to the growth rate.

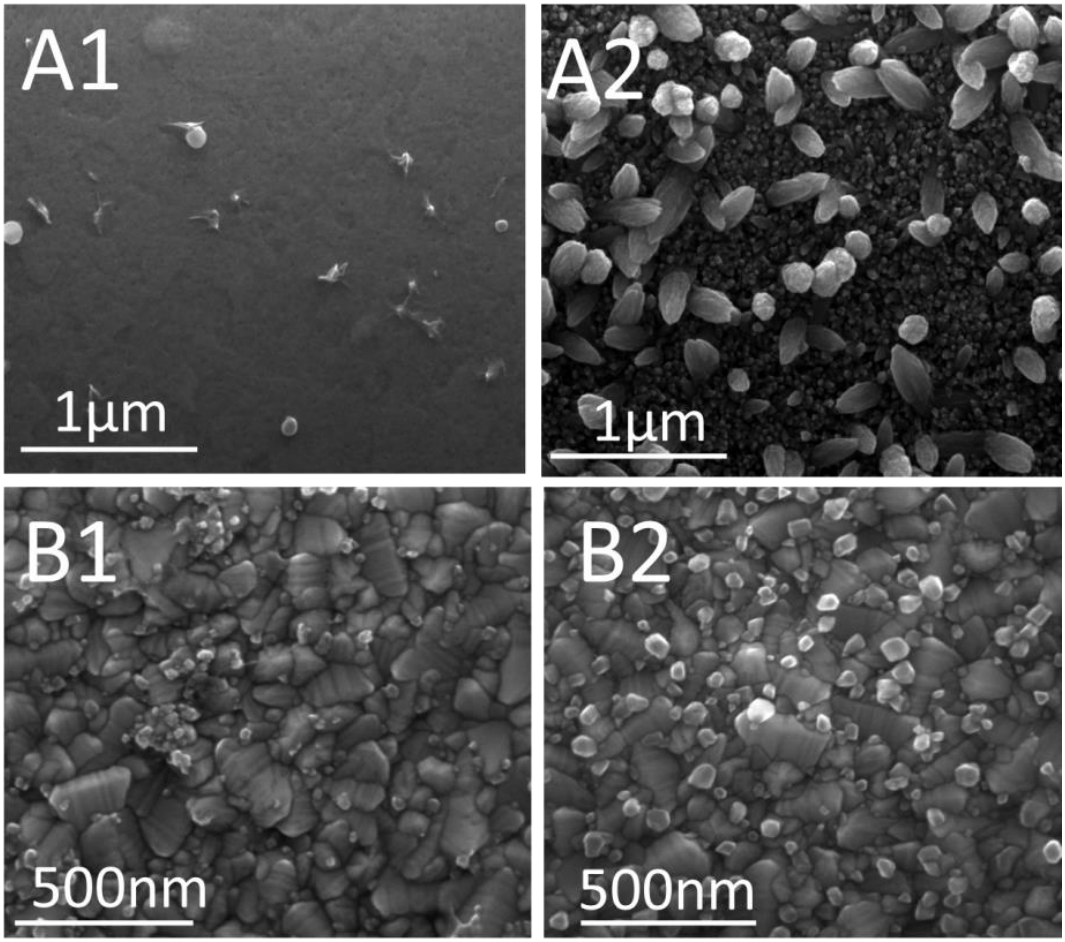

Figure 4.6 The SEM micrographs show the initial stages of A) pH 11 B) pH 6 ZnO growth at 1) 30 minutes and 2) 45 minute intervals.

For both pH 6 and 11 solutions, virtually no growth was observed for the initial 30 minutes into the synthesis (Figure 4.6 – A1, B1). However, 15 minutes later, ZnO growth was clearly observed for both solutions (Figure 4.6 – A2, B2). It was during this 15 minute time interval that the minimum temperature required to initiate growth was reached; this supports the observed turbidity occurring during this time. Even at these early stages of growth, a significant difference in the ZnO morphology can be observed between the two solutions. Gherkin-shaped structures, some up to 200-400 nm long, were produced in the pH 11 solution and possess tapered tips with grooved edges (Figure 4.6-A2). The pH 6 solution exhibited a lower density of small (<100 nm), angular ZnO structures (Figure 4.6-B2). This provides further evidence that different rates of heterogeneous growth occurred in the two solutions, and would explain the morphological differences observed for the completed nanorod arrays.

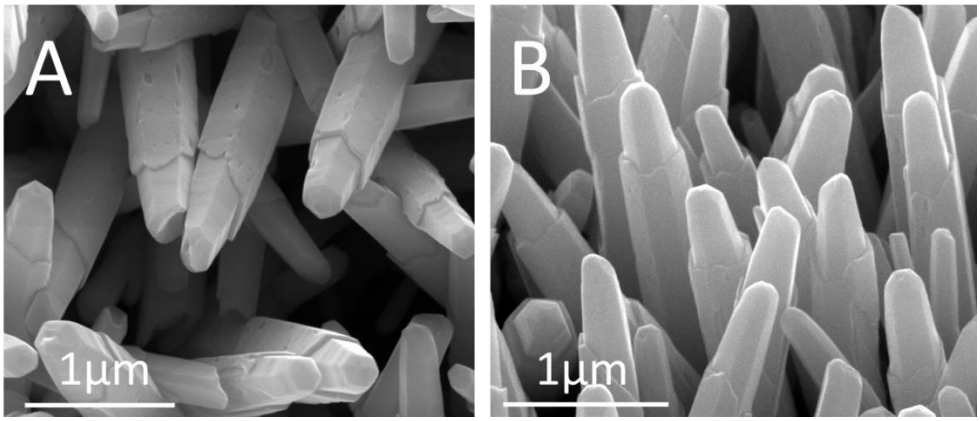

Figure 4.7 SEM micrographs of ammonia-etched (pH 11) ZnO-nanorods, A) a top-down view showing an inner core and an outer shell and B) a 45° tilted-view showing the rounded nanorod tips.

The pH 11 ZnO nanorods were chemically etched to reveal further detail about their internal structure. Different etch-rates were observed for what appears to be an outer-shell and a core structure of the nanorod (Figure 4.7A). This structure can be assigned to the rapid growth rate that favours small polycrystalline grain structures. However, during the multiple syntheses, the crystal structure at the core and base of nanorod would have had a longer growth period. This encourages the formation of larger crystal grains, which increases the chemical stability for these regions. Newly-formed polycrystalline ZnO layers (outer-shell) however, were easily etched away leaving behind the core-structures with rounded tips (Figure 4.7B). Incomplete syntheses lead to unreacted Zn-precursors remaining on the nanorod surface post-synthesis. These precursors gradually become trapped in the build-up of polycrystalline layers during the rapid growth rate.

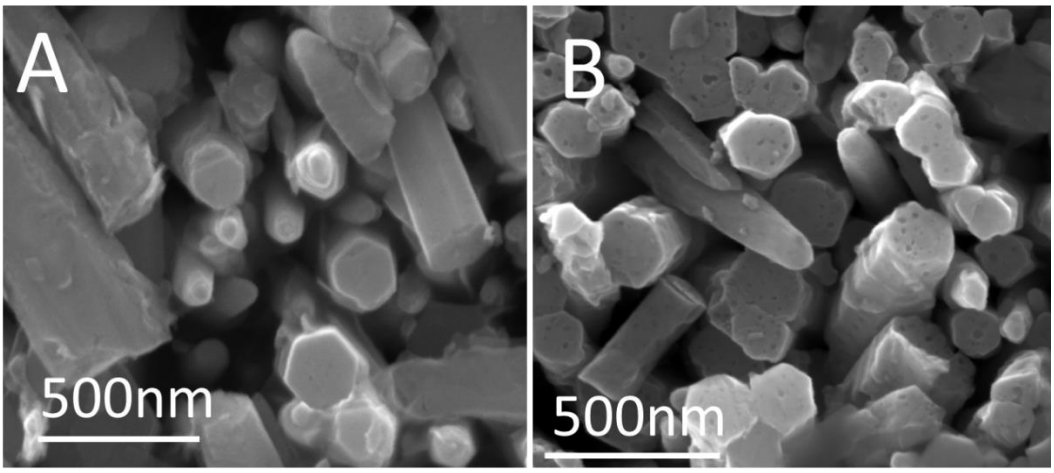

Figure 4.8 SEM micrographs showing the cross-section of pH -11 grown ZnO-nanorods, A) before and B) after annealing.

The nanorod cross-section was examined by removing the top of the ZnO array using a cotton tip. For as-grown nanorods the cross-section appears solid and smooth (Figure 4.8A), whereas the annealed sample revealed a pitted surface indicating the nanorod structure has numerous pores in its core structure (Figure 4.8B). The formation of these pits may be attributed to the metal-organic precursors trapped in the nanorod bulk, which decompose during the anneal process. The release of gaseous by-products (e.g. H_2, NH_3, CO_2, or N_2) accumulating at grain boundaries form pockets of gas enclosed in crystalline material before gradually diffusing out of the nanorods. This would result in the porous nanorod structure observed in Figure 4.8B.

4.3.2 Effect of annealing

As mentioned in the introduction to this section, the pH 6 synthesis is a well-established method and the well-formed crystal structure typically remains stable post-annealing. This was confirmed when the pH 6 ZnO nanorods were annealed in air for 1 h at 400˚C and no change in morphology was observed. The following discussion therefore concentrates on the morphological sensitivity observed for pH 11-nanorods post-annealing in oxygen, air, and nitrogen atmospheres.

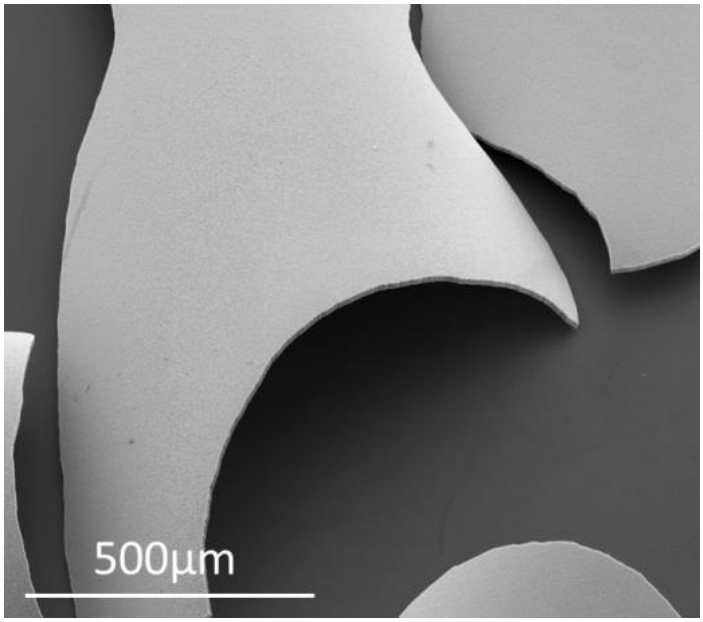

Figure 4.9 SEM image showing a film of ZnO nanorods peeling from the substrate surface.

Annealing the pH 11 grown ZnO would occasionally result in the film peeling away from the substrate surface, exposing the bare TCO beneath (Figure 4.9). This was attributed to the different thermal expansion coefficients and cooling rates of the ZnO bulk layer (at the

nanorod base) and TCO material, which caused the film to crack and buckle during the anneal process. Although this proved beneficial for imaging cross-sections of the array, it did not aid further development of the device. The gas flow rate and ramp rate of the anneal temperature were adjusted to minimise the thermal differences between the two materials. Maintaining a slow ramp rate of 3˚C/min and gas flow of 0.5 L/min was found to reduce the occurrence of peeling.

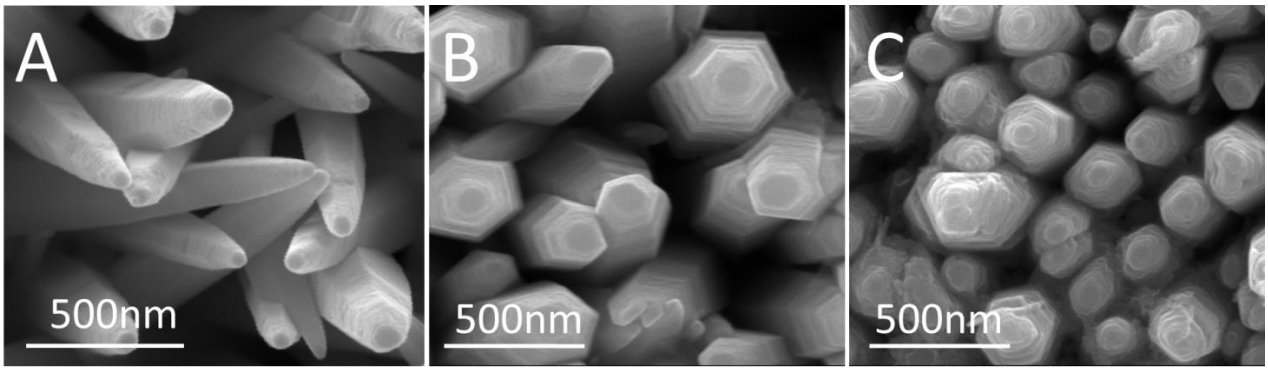

Figure 4.10 SEM micrographs (top-down view) of pH 11 grown ZnO-nanorods A) as-grown, and annealed in B) oxygen and C) nitrogen atmospheres at 400˚C for 1 hour.

As-grown nanorods were shown to have narrow tapered tips with a rough-appearing surface (Figure 4.10A). Upon annealing in oxygen and air atmospheres, the nanorod tips became more hexagonal and flater (Figure 4.10B). Nitrogen-annealed nanorods however, possess jagged, uneven peaks that appear to have degraded during the anneal process (Figure 4.10C). The chemical etching and thermal anneal process, establish that the nanorod surface was energetically unstable. Due to improved hexagonal morphology exhibited by the oxygen- and air-anneal (see Figure 4.10B), it suggests that oxygen was necessary for the crystallisation process. The degraded nanorods formed in the reducing nitrogen atmosphere (Figure 4.10C), serve to support this statement.

In order to determine whether the ZnO crytal structure was truely dependent on the presence of oxygen, different characterisation techniques were used to analyse the crystal structure.

4.4 Crystallography

Glancing incidence XRD (GIXRD) is typically used for analysing thin films. Here, it provides crystallographic information relating to the nanorods tips. The linear attenuation coefficient ($\bar{\mu}$) measures how strongly ZnO absorbs or scatter light. This can be calculated by the expression below:

$$\bar{\mu} = \bar{\rho} \sum \left(\frac{\mu}{\rho}\right)_i g_i, \quad (8)$$

where $\bar{\rho}$ is the density of ZnO (5.675 g·cm^{-3}), $\left(\frac{\mu}{\rho}\right)$ is the mass attenuation coefficient of Zn ~ 56.60 (cm^2·g^{-1}) and O ~11.16 (cm^2·g^{-1}) (for 8 keV X-rays), and g_i is the mass fraction (Zn ~0.80 and O ~0.20) [264]. Appling these values for ZnO gives $\bar{\mu}$ = 269.6 cm^{-1}. The penetration depth (l) of the X-rays used in the GIXRD analysis can be determined using:

$$l = \frac{\sin \alpha}{\bar{\mu}} \quad (9)$$

For the glancing angle (α) of 3˚ this gives a penetration depth of 1.94 µm.

4.4.1 pH 6-synethsised ZnO-nanorods

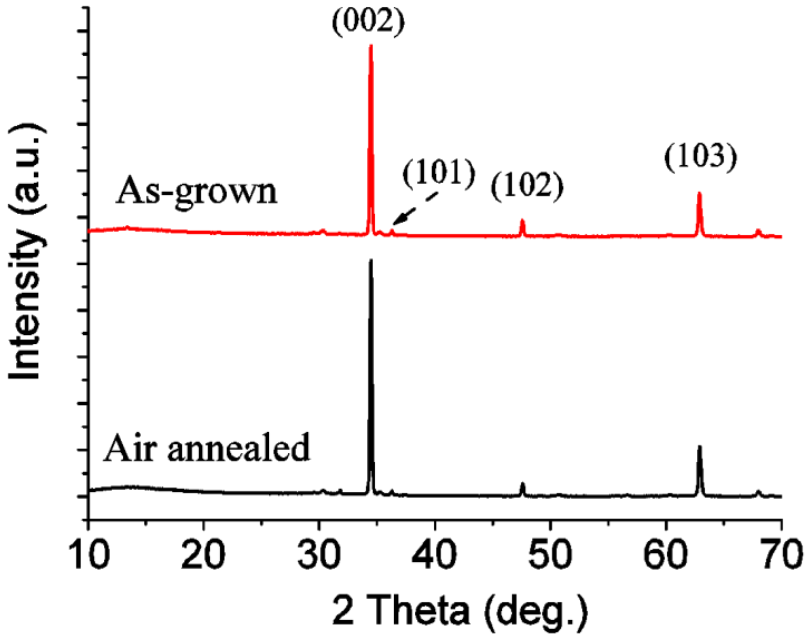

Figure 4.11 Glancing incidence XRD plot of pH 6 grown ZnO nanorods, at room temperature and post-annealing for 1 hour at 400˚C in air.

GIXRD analysis confirmed the wurtzite crystal structure of ZnO pH 6 nanorods with peaks indexed according to the JCPDS 36-1451. Figure 4.11 shows the nanorods are primarily orientated in the c-axis as expected from the SEM Figure 4.4. No difference in the crystal structure or orientation was shown to occur post-annealing in air. This is further evidence to support the stability of the crystal structure formed during the pH 6 synthesis process, with no morphological changes observed.

4.4.2 pH 11-synethsised ZnO-nanorods

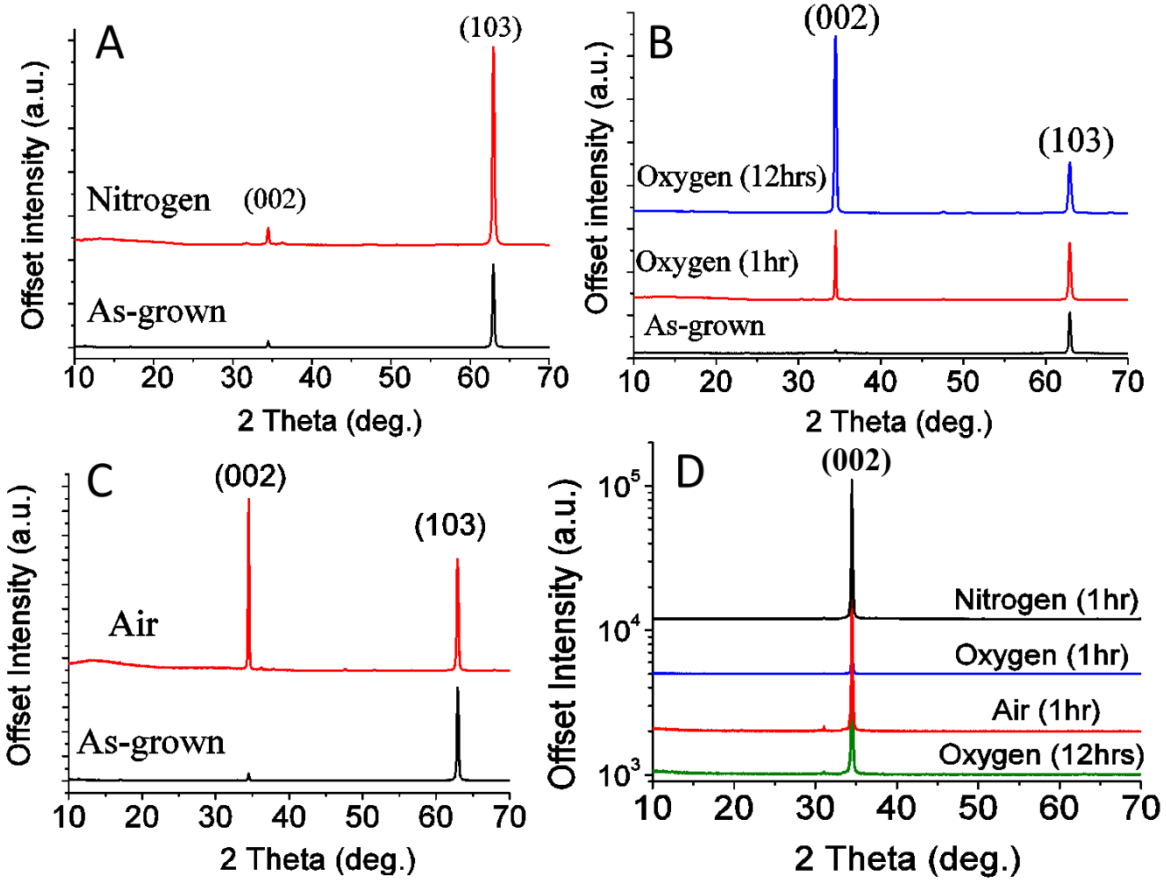

Figure 4.12 GIXRD of pH 11 synthesised ZnO-nanorods in various annealing atmospheres of A) nitrogen, B) oxygen and C) air. D) Theta-2Theta XRD of all ZnO nanorods on a logarithmic scale.

GIXRD analysis of pH 11 nanorods revealed significant changes in crystal structure for the different anneal-atmospheres. Firstly, as-grown ZnO shows a dominent orientation in the [103] direction, which intensifies upon annealing in nitrogen (Figure 4.12A). However, in the presence of oxygen (air/oxygen anneal atmospheres), a significant rise in (002) peak intensity was observed (Figure 4.12B and C). The (002) peak continued to increase with anneal duration and becomes the dominent orientation after annealing for 12 h (Figure 4.12B). This change in peak intesnity was either due to smaller particles agglomerating to form larger crystal grains in the [002] orientation, or alternatively, the formation of new ZnO from Zn-precursors trapped in the crystal lattice. The evidence in Figure 4.12 points towards the latter, as the aglomeration of smaller particles would occur for all anneal atomospheres, but the latter only occurs in the presence of oxygen, which in this case it does. Theta-2theta XRD analyses the entire nanorod array from a fixed position perpendicular to the substrate and

obtains the spectra in Figure 4.12D. This supports the SEM analysis (Figure 4.5B) that displays well-aligned crystalline nanorods orientated in the c-axis direction.

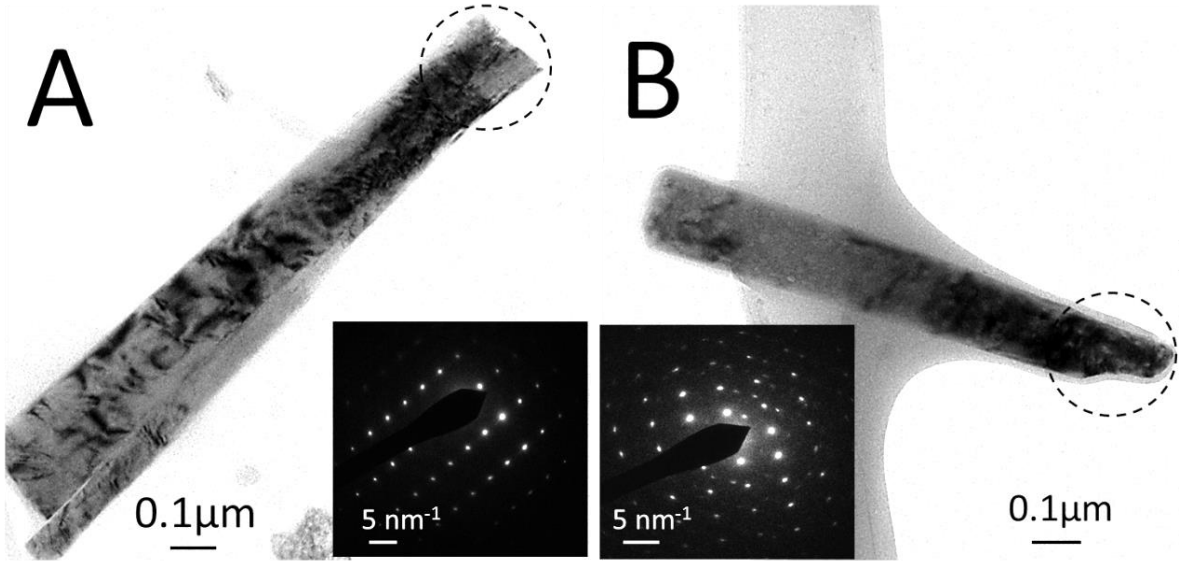

Figure 4.13 TEM micrographs of pH 11 grown ZnO nanorods A) as-grown and B) post-annealing in air (1 h), insets show the selected-area electron diffraction pattern for the areas indicated by the dashed circle.

Transmission electron microscopy (TEM) was used to analyse the structure of single ZnO nanorods. Bright-field TEM micrographs show the nanorod before (Figure 4.13A) and after annealing (Figure 4.13B). The inconsistent contrast across the nanorod length in both Figure 4.13 A and B indicates areas of different densities, dislocations, or other morphological defects. The mottled contrast in Figure 4.13B is evidence that defects remain in the lattice after annealing for 1 h at 400˚C. SAED patterns were used to obtain information regarding the crystal lattice. The inset of Figure 4.13A shows a well-defined wurtzite pattern for the as-grown ZnO nanorods. However, multiple diffraction patterns were detected for the annealed sample (Figure 4.13B inset). The additional crystal lattices would be further evidence of new crystalline material formed during the anneal process.

HRTEM imaging provides improved resolution of the nanorod structure and shows numerous brighter spots approximately 10-20 nm in diameter patterning the nanorod structure (Figure 4.14A). This is evidence of the porous structure left behind post-annealing as indicated by Figure 4.8B. In Figure 4.14B the crystal lattice of the ZnO nanorod was observed, the c-axis direction is indicated perpendicular to the lattice planes (white arrow).

The average lattice separation was measured as 0.518 nm and is in good agreement with the expected 0.520 nm reported for ZnO [265].

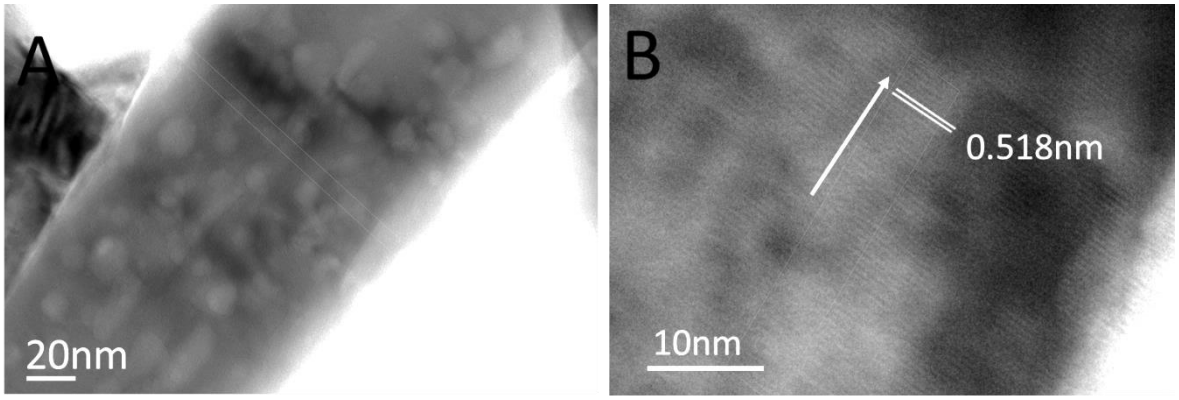

Figure 4.14 HRTEM images of A) an annealed ZnO nanorod and B) showing the lattice separation and c-axis direction (white arrow).

4.5 Optical Analysis

4.5.1 Colouration

ZnO is thermochromic; typically ZnO is grey at room temperature but becomes yellow when heated above 300˚C due to desorption of oxygen from the surface. Upon cooling the re-adsorption of oxygen returns ZnO back to its original colour.

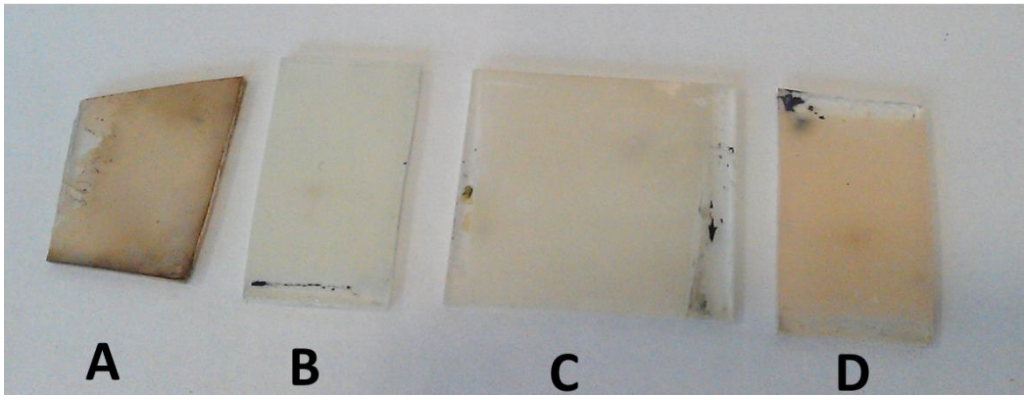

Figure 4.15 Colouration of ZnO nanorods: A) nitrogen-annealed B) as-grown C) oxygen-annealed and D) air-annealed.

However, in the case of pH 11 grown ZnO nanorods, a permanent colour change was observed. The original grey ZnO (Figure 4.15B) turned brown, creamy-yellow, and pink post-annealing in nitrogen, oxygen, and air, respectively (Figure 4.15 A, C, and D). This permanent colour change in ZnO was previously reported for ZnO annealed in temperature

exceeding 1000˚C and assigned to the introduction of intrinsic defects during the anneal process [71]. However, as discussed in section 2.1.4.2, the cause of the colouration remains in question and further analysis would be required to determine the source.

4.5.2 UV-Vis absorption

Absorption spectra were used to analyse the optical transparency of the ZnO nanorods grown here. This enabled the use of Tauc plots that can approximate the optical band-gap of the material.

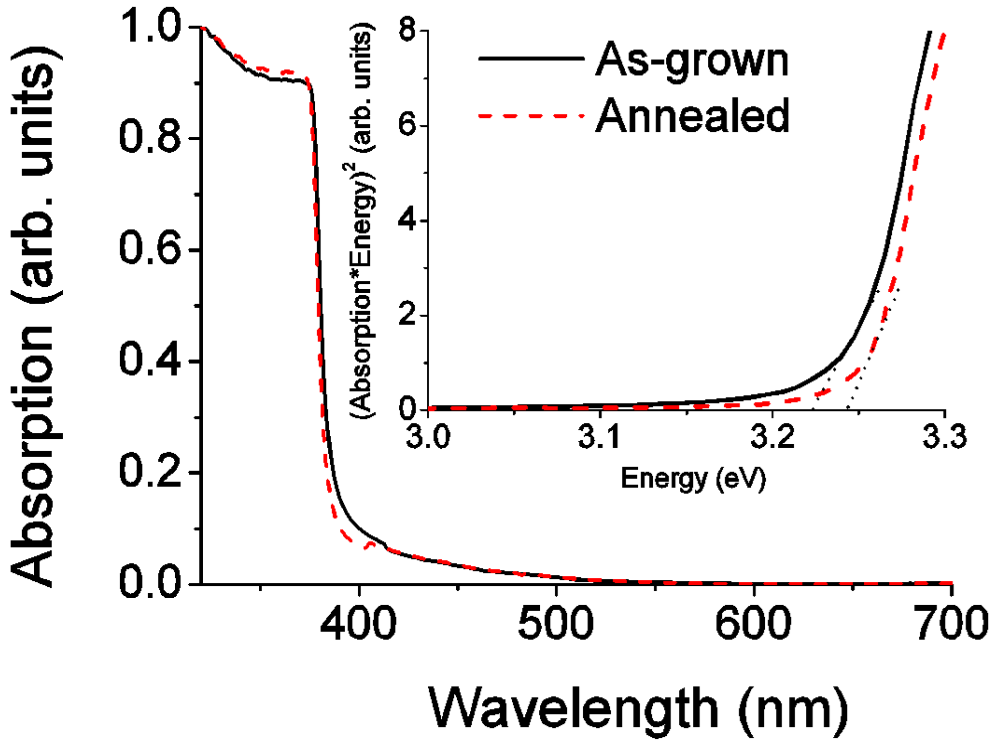

Figure 4.16 Absorption spectra of pH 6 grown ZnO nanorods, before and after annealing in air at 400˚C. Inset displays the Tauc plot and the dotted-lines represent the optical band-gap approximations.

The absorption spectra of pH 6 grown nanorods shown in Figure 4.16, demonstrates the high optical transparency associated with ZnO. The absorption onset at ~380 nm corresponds to the wide band-gap (~3.3 eV) of ZnO. The Tauc plot shows a slight increase in the optical band-gap from 3.22 to 3.24 eV for as-grown to annealed ZnO, respectively. This can be assigned to an improved crystal lattice or the removal of point defects during the anneal process, both of which reduce recombination centres related to the visible region of the spectra and therefore improves UV emission.

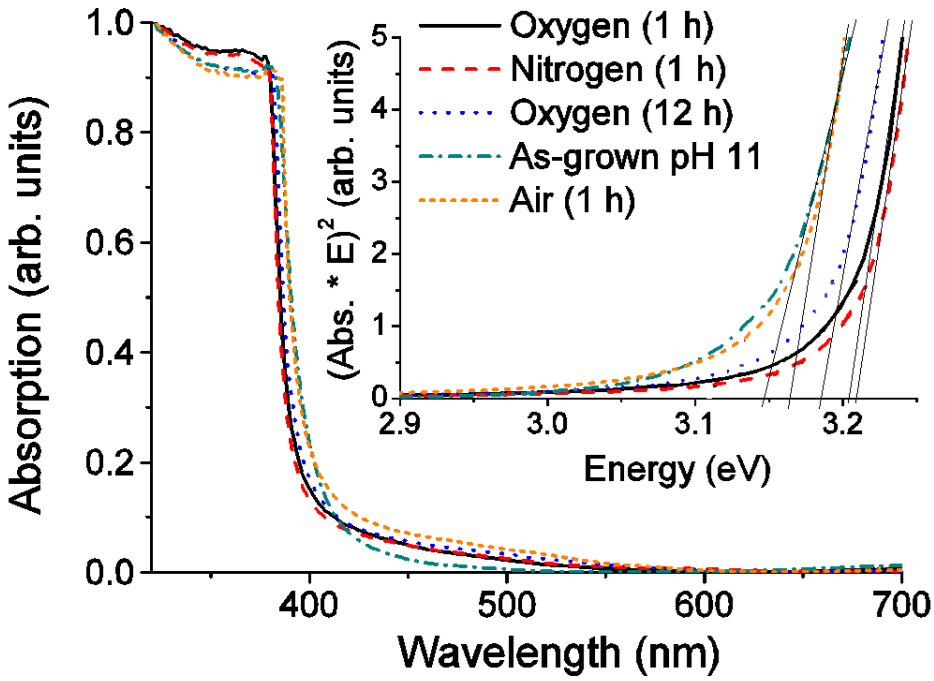

Figure 4.17 Absorption spectra of pH 11 grown ZnO nanorods, before and after annealing in various atmospheres. Inset displays the corresponding Tauc plot; the solid-lines represent the optical band-gap approximations.

As with the pH 6 nanorods, the absorption spectra of pH 11 nanorods show good optical transparency to the visible region. However, an earlier absorption onset was observed around 390-400 nm (Figure 4.17). This becomes clearer when studying the Tauc plot (inset Figure 4.17), which shows the optical bandgap is lower by ~0.1 eV when compared to that of the pH 6 ZnO (Figure 4.16 inset). The difference was attributed to the significant quantity of defects present in the pH 11 nanorods as evidenced by the permanent discoloration and morphological changes. These defects act as recombination centres that influence the optical properties by trapping electrons that would otherwise transition to the valence band and contribute to the UV emission. Thermal annealing was used to improve the crystal lattice by energising point defects to migrate through the lattice into lower energy states or diffuse out of the nanorod. The removal of these defects from the lattice serves to improve the crystallinity and hence increase the optical band-gap, as shown by the inset of Figure 4.17. The optical bandgap of the 12 h oxygen anneal was lower than that of the oxygen 1 h anneal. This suggests that prolonging the anneal time at 400˚C is insufficient for the removal of these defects.

4.5.3 Raman spectroscopy

Long-range Raman spectroscopy was employed to determine whether any unreacted precursor materials from the synthesis process were present near the surface of ZnO nanorods before and after annealing.

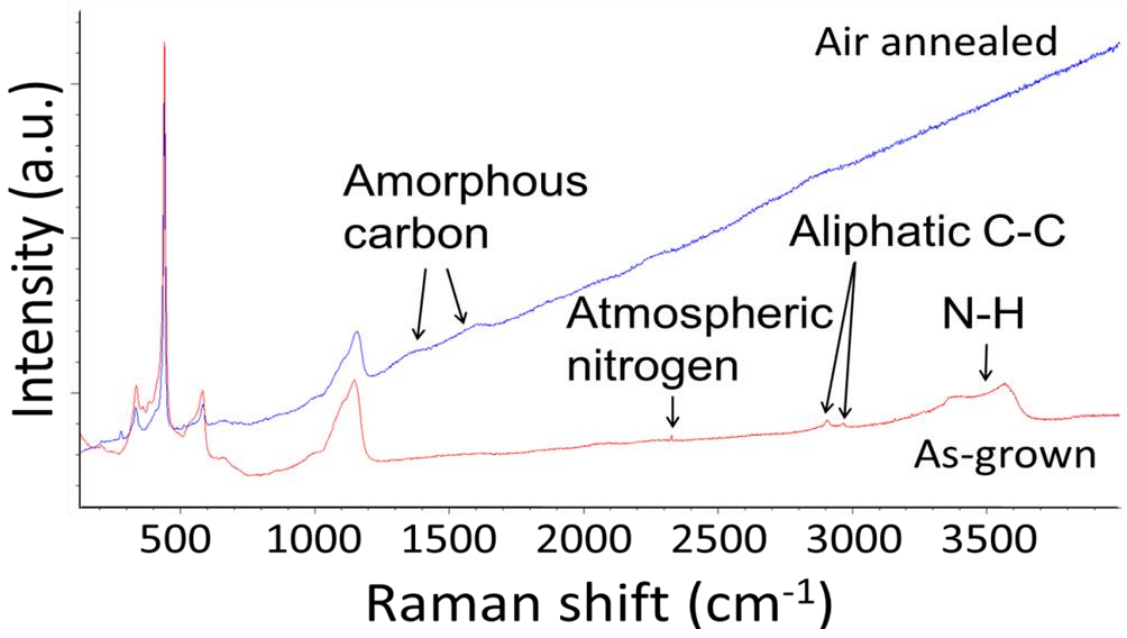

Figure 4.18 A long-range Raman spectra of (pH 11) ZnO nanorods as-grown and annealed in air.

Aliphatic carbon, N-H_x species and atmospheric nitrogen were detected prior to annealing, which confirmed the presence of unreacted precursor material on the nanorod surface (Figure 4.18). Post-annealing these peaks are removed, which implies the anneal process has removed or converted the precursors into another form. The increasing slope of the air-annealed sample is evidence of photoluminescence behaviour under the 473 nm laser excitation. The earlier peaks (<1500 cm^{-1}) are not labelled in Figure 4.18, but a more detailed view of this region is presented in Figure 4.19.

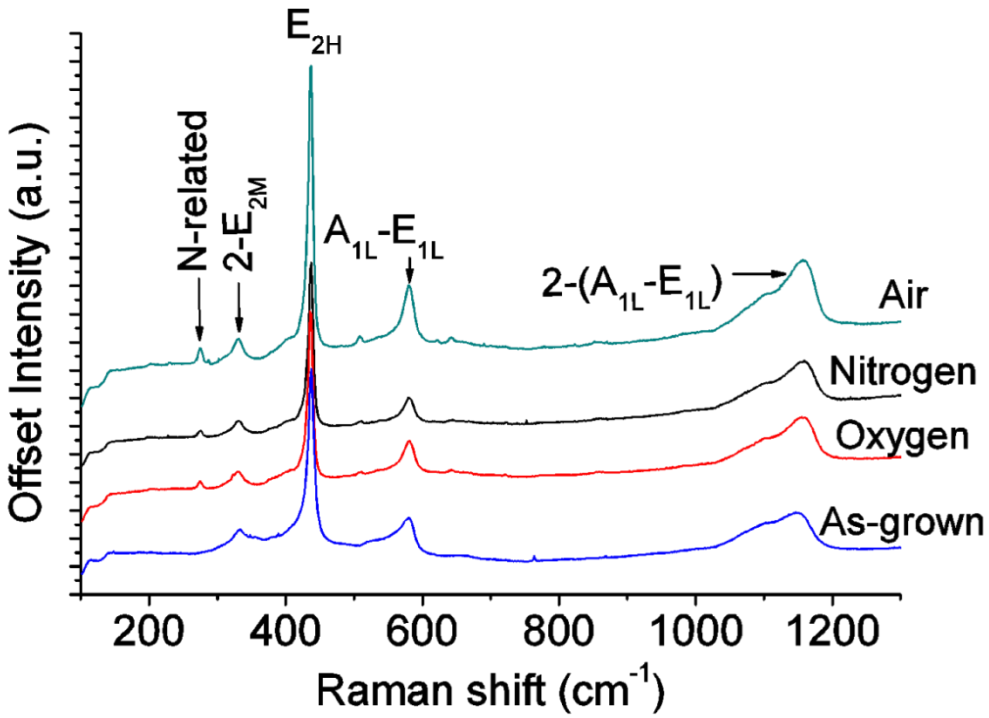

Figure 4.19 A Raman spectra (offset in the y-axis) of (pH 11) ZnO nanorods as-grown, and annealed in various atmospheres.

The intense E_{2H} mode for all samples is further evidence of the high crystallinity of these nanorods. The second-order Raman spectral peak ($2\text{-}E_{2M}$) at 329 cm^{-1}, the first-order ($A_{1L}\text{-}E_{1L}$) mode at 579 cm^{-1} and second-order ($2\text{-}(A_{1L}\text{-}E_{1L})$) mode at 1158 cm^{-1} are all associated with ZnO. However, additional peaks at 273 cm^{-1} and 508 cm^{-1} were observed for annealed samples (Figure 4.19) and have previously been reported as nitrogen-related peaks [117] (see section 2.1.3.2.2). The N-related peak present for all annealed samples implies the source of N-doping originates from the synthesis process rather than the anneal atmosphere. This gives evidence to suggest the $N\text{-}H_x$ species detected in long-range Raman analysis has not been entirely removed but converted to form separate N-related species, resulting in the unintentional N-doping of pH 11 nanorods.

4.5.4 Photoluminescence

Photoluminescence (PL) measurements were undertaken in order to probe the energy transitions within the ZnO and determine a relationship between material colour and defect structure.

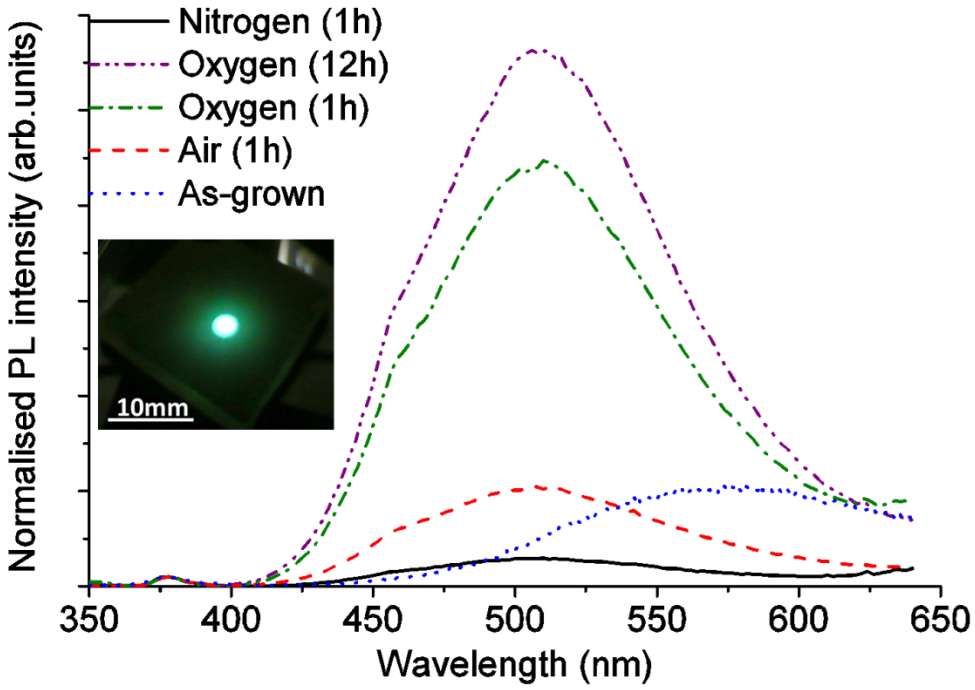

Figure 4.20 Normalised photoluminescence spectra to the UV emission peak of pH 11 ZnO nanorods, as-grown and annealed in various atmospheres at 400˚C. Inset photograph shows the green luminescence visible to the naked eye.

The strong Raman E_{2H} mode, dominant (002) XRD peak, and wurtzite SAED pattern observed for all samples indicate the high ZnO crystallinity. Consequently, this would be expected to generate strong near band-edge emission (NBE). However, the normalised PL in Figure 4.20 shows a weak NBE emission at ~377 nm (3.3 eV) for all samples. The reduced emission suggests a rapid recombination at defect states that give rise to the deep-level emission (DLE) observed here. Yellow DLE at ~570 nm (2.2 eV) was observed for the as-grown sample and has previously been linked to $Zn(OH)_2$ on the surface [150]. However, in this case the O-H stretching mode was not detected by Raman at 3200-3600 cm^{-1} suggesting another source for yellow emission. As discussed previously, the Raman analysis shows N-H_x species present near the surface and this may account for the yellow PL emission. This is supported by the Raman stretching mode of N-H present prior to annealing at 3300-3600 cm^{-1} and its disappearance post-annealing, consequently when the yellow PL emission is also removed.

Annealing of the ZnO nanorods resulted in the development of an intense broad green DLE peak at ~505 nm (2.4 eV), with a shoulder in the blue region at ~460 nm (see Figure 4.20 and inset). The weak NBE and strong DLE is further evidence that interactions at the surface can

alter the measured PL spectra as nanorods that exhibit a well ordered structure are expected to produce a strong NBE. PL analysis showed the green (2.4 eV) emission was highest when annealed in oxygen, followed by air and nitrogen. Blue emission was previously linked to the presence of zinc interstitials (Zn_i) [138], although numerous theoretical calculations shows these defects are relatively unstable and would easily anneal out at 400˚C [68,84,86,266]. Look *et al*.[267] however proposed that complexes of Zn_i and nitrogen impurities could be stable and act as shallow donors.

In order to give a guide whether acceptors or donors are the majority carriers in ZnO, Hall measurements were performed on the air-annealed sample. A bulk donor concentration of n = $8.5x10^{16}$ cm^{-3} confirmed ZnO was n-type, with a carrier mobility of μ_e = 1.63 cm^2 $V.s^{-1}$. Due to the porous nature of the array only the bulk region of the ZnO array, consisting of fused nanorods at the base, was subject to the electric field. Hence the thickness of this region (~4 µm – see Figure 4.5B) was used to calculate the bulk concentration. The conductivity was calculated to be 1.2 $S.m^{-1}$.

The assignment of the green emission to a particular defect structure is a complex task, as a number of defects have previously been assigned to this emission [127–129]. Correlations between the green luminescence and oxygen vacancies (V_O) are frequently cited, which were based on V_O being assigned to the g~1.96 line in EPR measurements [268]. This has since been shown to be due to shallow donors or conduction band electrons [71]. Furthermore the V_O electronic transition state (2+/0) is reported to be 0.5 eV [84] or 0.4 eV [86] above the VBM or 3.0 eV [269] below the CBM, which makes V_O an unlikely contributor to green emission. A growing body of evidence indicates that V_{Zn}^{2-} may be a significant contributor to green luminescence. V_{Zn}^{2-} has a transition between the (1-/2-) charge states 0.9 eV above the valence band maximum (VBM). The transition from the conduction band to the (-1/-2) state would give rise to the green (2.4 eV) emission observed here. However, it must be considered whether it is possible to form V_{Zn} using the synthesis and processing used here.

First-principle studies by Van de Walle *et al.* and numerous authors since [68,84,86,266] have used local-density-function approximations (LDA) to calculate the formation energies of various defects in ZnO. These latest studies are finding that V_{Zn}^{2-} have the lowest formation energy in O-rich conditions for n-type ZnO. The high pH synthesis environment arises from the high quantity of available hydroxyl ions (see reaction schemes), which

provides an excess of oxygen for the reaction. Hence, under the O-rich synthesis conditions, V_{Zn}^{2-} are the most energetically favourable and stable defects to form in the ZnO-nanorods.

The absence of green emission prior to annealing is attributed to H^+ defects, which are present from various sources in the aqueous synthesis and considered to be shallow donors in ZnO. Van de Walle [91] suggested H-doping was the cause of ZnO n-type behaviour, and as a donor-defect it would effectively passivate acceptor-states such as V_{Zn}^{2-}.

During the oxygen/air-anneal, any N-H_x on the nanorod surface is oxidised and ZnO is formed from the unreacted Zn-precursor material. Simultaneously, N-H_x trapped in the nanorod bulk dissociates to form N- and H-related species. This leads to the N-doping of the nanorods, while the liberated H^+ gradually diffuses out of the nanorods, or substitutes on available V_O sites (H_O) forming shallow donors [95]. As a result, H^+ passivation of the V_{Zn}^{2-} defects and associated PL quenching is significantly reduced [270]. Due to the nanorod morphology and low H_2 partial pressure of all anneal atmospheres, it is predicted that the outward diffusion rate of H_2 is similar for all atmospheres; hence the appearance of green DLE post-annealing in all cases.

To account for the dependence of green emission intensity on the anneal atmosphere, it is proposed that two processes occur during the thermal anneal: firstly, the oxidation of remnant Zn-precursors to form new ZnO (oxygen/air-anneal only), and secondly, once the Zn-precursors are exhausted, newly formed ZnO at the nanorod surface is subject to the formation of additional V_{Zn}^{2-} under high oxygen partial pressure conditions (oxygen-anneal only). Neither of these processes occurs during the reducing nitrogen-anneal. Instead, the Zn-precursors decompose forming an amorphous region at the surface that quenches emission from the bulk, or alternatively compensators (e.g. V_O, N_{Zn}, (N_{Zn}-$2V_{Zn}$), or (Zn_i-N_O)) are formed that passivate V_{Zn}^{2-} sites and quench the emission. This explains the observed trend of DLE intensity in Figure 4.20: oxygen > air > nitrogen. The prolonged 12 h oxygen-anneal indicates the defect responsible for the green emission is relatively stable at temperatures of ~400˚C (Figure 4.20).

Tam *et al.* [129] used positron annihilation spectroscopy (PAS) to link acceptor-like V_{Zn} defects to the green emission. It was pointed out that single-point defects are relatively mobile at high temperatures and would easily anneal out below 600˚C. This argument gives rise to the alternative belief that a more stable V_{Zn}-defect complex is responsible for green emission [271]. Recently Kuznetsov *et al.* [146] conducted PAS, PL and Hall measurements

on ZnO and related them to previous findings to ascertain the origins of green luminescence. It was concluded that an extrinsic acceptor-like impurity such as Cu_{Zn} was most likely responsible, and that these defect states could be readily passivated by V_O. As the formation energy of V_O is lower in reducing atmospheres, this alternative hypothesis could also explain the DLE trend observed here.

Despite these attempts to assign the green emission to particular defects, as of yet a direct method for detecting specific defects in ZnO does not currently exist. Therefore, it cannot be demonstrated conclusively that V_{Zn}^{2-} are solely responsible for green emission. However, a large body of evidence supports the preferential formation of V_{Zn}^{2-} in O-rich conditions, as is proposed here, which also accounts for the highest green emission intensity for oxygen annealed ZnO. Therefore the green emission for these ZnO-nanorods is assigned to the presence of zinc vacancies.

4.6 Extended X-ray absorption fine structure (EXAFS) analysis

EXAFS analysis was obtained for the absorbing Zn atom with a K edge of 9659 eV using both transmission mode (TM) and optically-detected mode (OM) (see experimental section 3.2.10). The pre-requisite for EXAFS in OM is strong emission in the visible region; it was therefore only satisfied by the annealed pH 11 grown nanorods.

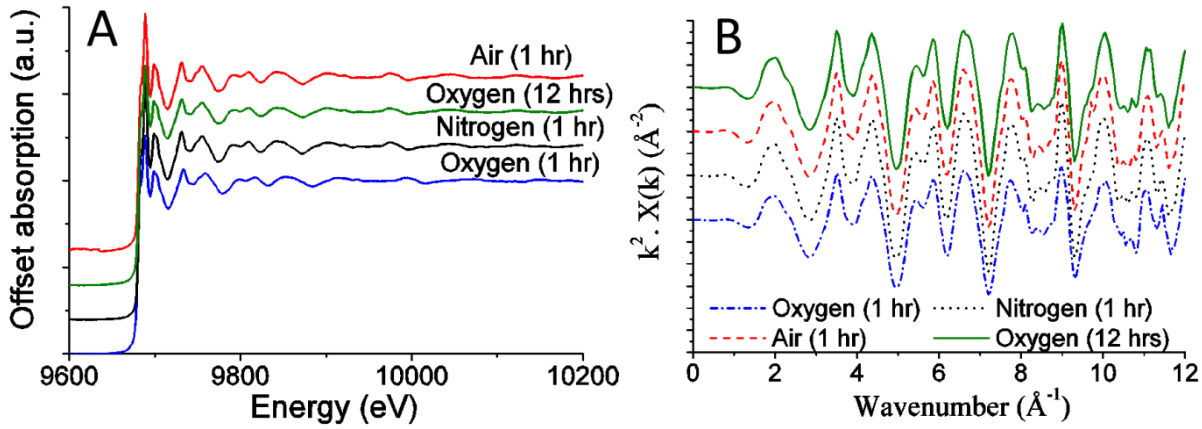

Figure 4.21 A) EXAFS obtained in transmission mode for ZnO nanorods annealed in various atmospheres and B) their corresponding k-space spectra.

The EXAFS absorption spectra and corresponding k-space for TM was given in Figure 4.21A and B. As-grown ZnO nanorods did not exhibit the intensity of emission required to generate

a reasonable EXAFS signal and so was omitted from this study. A clear onset of the absorption edge was observed for the Zn atom at ~9659 eV (Figure 4.21A) and the k-space spectra corresponds to the scattering and absorption of electrons within the atomic structure surrounding the central Zn atom (Figure 4.21B).

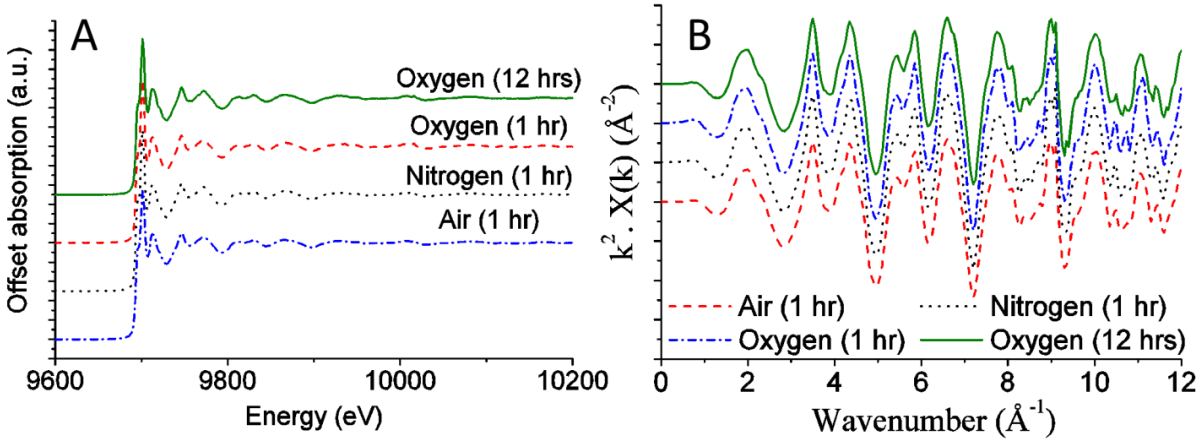

Figure 4.22 EXAFS (offset in y-axis) of ZnO obtained in optically-detected mode showing a) absorption spectra of the annealed specimens and b) the corresponding k-space data.

Figure 4.22A and B demonstrates high-quality XEOL was obtained in OM up to 12.0 $Å^{-1}$. This data presents a unique opportunity to examine the local structure surrounding the absorbing Zn atom relating to specific wavelength emissions.

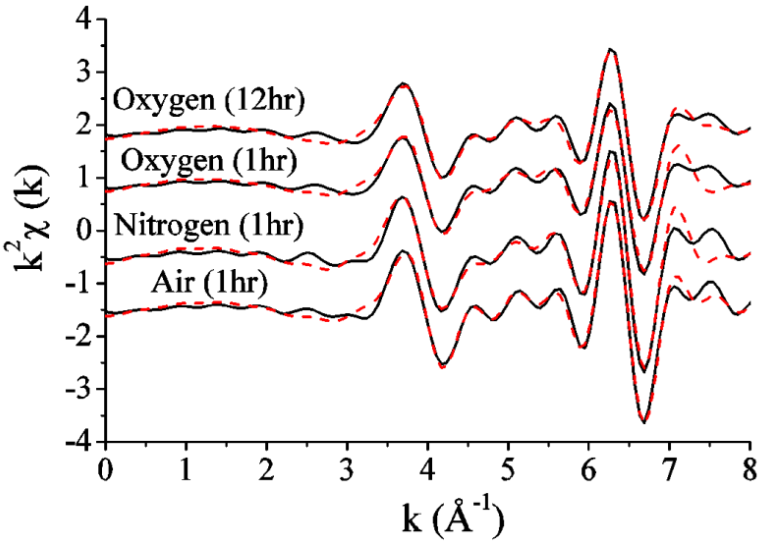

Figure 4.23 EXAFS obtained in transmission mode for ZnO-nanorods annealed in air, nitrogen and oxygen. The plots are offset in the y-axis and the theoretical fit is represented by the red dashed-line.

The k^2-weighted EXAFS in TM and their corresponding fits are shown in Figure 4.23. The bond lengths extrapolated from the fits are presented in Table 4-1.

Table 4-1 Bond length (d), Debye-Waller factor (σ^2) for ZnO nanorods extrapolated from TM EXAFS data in Figure 4.23. Model obtained corresponds to a fully occupied wurtzite structure (space group: p63m) with lattice parameters a and b = 3.245 Å, c = 5.205 Å and the crystalline symmetry of oxygen *(u)* = 0.345. S_0^2 of 0.95(5) was used in the data fits [272].

	Zn-O_1			Zn-O_2			Zn-Zn_1			Zn-Zn_2		
Specimen	***N***	***d* (Å)**	**σ^2 (Å^2)**	***N***	***d* (Å)**	**σ^2 (Å^2)**	***N***	***d* (Å)**	**σ^2 (Å^2)**	***N***	***d* (Å)**	**σ^2 (Å^2)**
Model	1	1.9526		3	1.9858		6	3.2090		6	3.2495	
Nitrogen (1 h)	1	2.0131	0.0041	3	1.9772	0.0046	6	3.1913	0.0021	6	3.3114	0.0021
Air (1 h)	1	2.0020	0.0044	3	1.9817	0.0049	6	3.1900	0.0023	6	3.3079	0.0023
Oxygen (1 h)	1	1.9058	0.0049	3	1.9930	0.0054	6	3.1944	0.0025	6	3.3211	0.0025
Oxygen (12 h)	1	1.9642	0.0054	3	1.9832	0.0060	6	3.1870	0.0028	6	3.3074	0.0028

The bond lengths are shown to be within 0.07 Å of the wurtzite ZnO model. The low-temperature environment used for this experiment (100 K) means the Debye-Waller factor (σ^2) is primarily dependent on the static disorder of lattice, as the thermal vibration of the atomic pairs will be minimal. The first shell (Zn-O) shows a σ^2 of ~0.005, which is relatively high when compared to similar values previously reported by Han *et al.* at RT [273]. In addition, the σ^2 values are significantly reduced for the second shell, indicating that the average crystal structure has low Zn-Zn disorder when compared to Zn-O. A correlation was observed in Table 4-1 between the increasing disorder (σ^2) and the oxygen partial pressure. This suggests the defects responsible for the disorder play a major role in the overall emission.

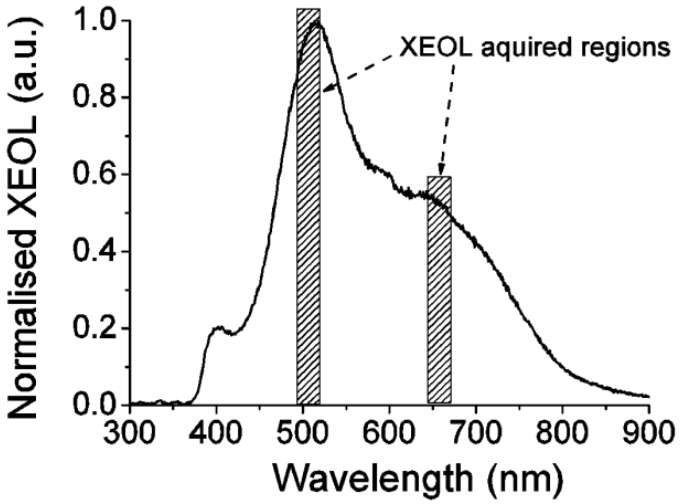

Figure 4.24 A representation of the XEOL emission spectra for air-annealed nanorods at RT, indicating the 500 nm and 660 nm deep-level emission regions used for EXAFS data analysis.

XEOL was obtained in OM for spectral regions that possessed high DLE intensity under X-ray excitation i.e. 500 nm and 660 nm as shown in Figure 4.24. Fourier transforms (FT) were plotted for the two spectral regions (Figure 4.25) with the extrapolated site-specific information shown in Table 4-2.

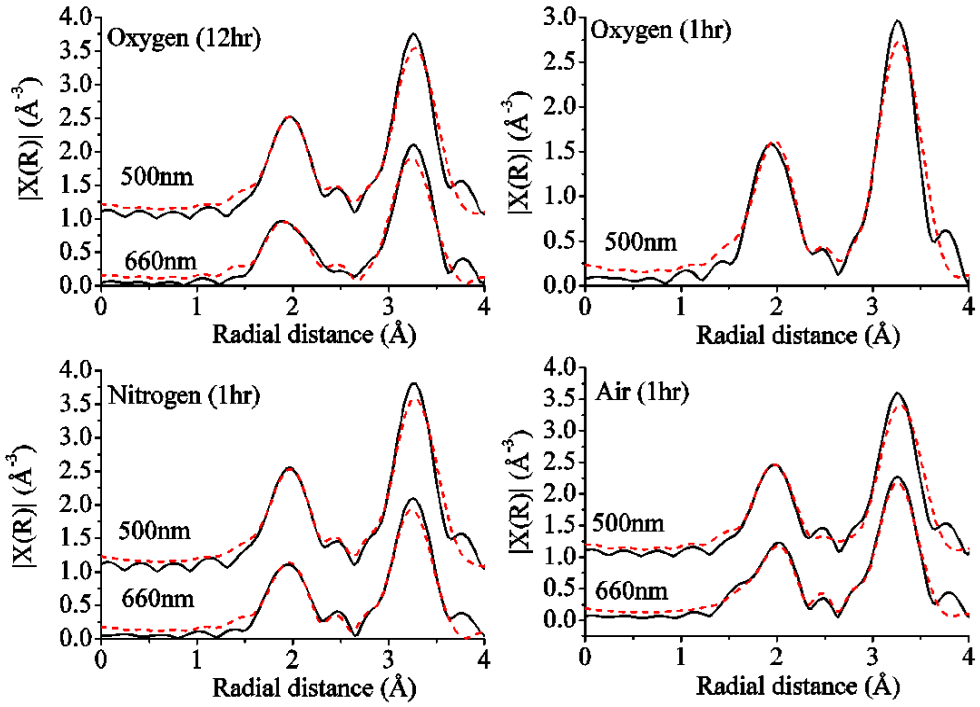

Figure 4.25 Fourier transformed EXAFS (offset in the y-axis) for 500 nm and 660 nm XEOL emission from ZnO-nanorods annealed in air, oxygen, and nitrogen (solid-line) and their theoretical fit (red dashed-line).

Table 4-2 Bond length (d), degeneracy (N), and Debye-Waller factor (σ^2) obtained using specific XEOL wavelengths detected from ZnO nanorods annealed in various atmospheres.

	Zn-O(1)			Zn-O(2)			Zn-Zn(1)			Zn-Zn(2)		
Specimen	***N***	***d* (Å)**	**σ^2 (Å^2)**	***N***	***d* (Å)**	**σ^2 (Å^2)**	***N***	***d* (Å)**	**σ^2 (Å^2)**	***N***	***d* (Å)**	**σ^2 (Å^2)**
Model	1	1.9526		3	1.9858		6	3.2090		6	3.2495	
Nitrogen (1 h) 500nm	0.8	1.9915	0.0034	2.4	1.9685	0.0035	4.5	3.1798	0.0019	4.5	3.2961	0.0019
Air (1 h) 500nm	0.7	1.9905	0.0028	2.1	1.9709	0.0029	3.9	3.1814	0.0016	3.9	3.2962	0.0016
Oxygen (1 h) 500nm	0.9	1.8836	0.0030	2.7	1.9778	0.0030	5.0	3.1776	0.0034	5.0	3.2716	0.0034
Oxygen (12 h) 500nm	0.8	1.9899	0.0032	2.4	1.9702	0.0033	5.4	3.1793	0.0044	5.4	3.2767	0.0044
Nitrogen (1 h) 660nm	0.5	1.9904	0.0034	1.5	1.9565	0.0035	3.2	3.1899	0.0017	3.2	3.3063	0.0017
Air (1 h) 660nm	0.6	1.9913	0.0035	1.8	1.9660	0.0036	3.6	3.1724	0.0017	3.6	3.2880	0.0017
Oxygen (12 h) 660nm	0.6	1.9510	0.0060	1.8	1.9737	0.0062	3.4	3.1855	0.0035	3.4	3.2691	0.0035

The sensitivity of this technique was highlighted by variances between the two wavelength emissions that show changes in both peak position and width. This demonstrates the ability to

detect subtle changes in the atomic structure related to the different emission centres. It should be noted that OM is a surface sensitive technique and so emissions are influenced by photon scattering, re-absorption, and surface defects. These bond lengths relate to the specific regions where the DLE originates. Consequently, due to the different anneal atmospheres the defects may form in different regions of the nanorods i.e. the surface, bulk, or grain boundaries. This is evidenced by the varying values of σ^2 and degeneracy for the specimens.

The data obtained for 500 nm emission reveal the disorder in the Zn-Zn shell (σ^2) was significantly lower for nitrogen- and air-annealed specimens than for oxygen annealed ZnO (Table 4-2). This corresponds closely to the DLE intensities observed in Figure 4.20, and indicates the green (500 nm) emission is linked to disorder at Zn-sites in the lattice.

First and second shells both show diminished degeneracy (N) with respect to the model; this is accounted for by the XEOL strongly relying on surface emissions. The degeneracy has previously been used to analyse the displacement of atoms, deduce vacancies in the lattice [274], or differences in grain size [275]. The volume-to-surface ratio of the nanorods is calculated to be 1:25 (for nanorods dimensions: 10 µm long, 200 nm diameter and 1 nm surface depth). Hence, significant contribution to the lattice disorder arises from the surface as the theoretical fit solely relies on the bulk wurtzite model.

The variances in degeneracy were used to identify the regions emitting the specified wavelengths, i.e. bulk, grain boundaries, or surfaces. It is worth noting that the XEOL obtained is an average of data from all regions contributing to this wavelength emission. It is therefore not possible to pin-point the origins of emission. However, as the 660 nm emission shows higher disorder for the Zn-O shell for all specimens and is approximately half the expected degeneracy for both Zn-O and Zn-Zn shells, it can be inferred that the 660 nm emission originates from the nanorod surface for all specimens.

For 500 nm and 600 nm emission the oxygen (12h) annealed nanorods show significantly increased disorder than the other samples. This demonstrates that even after annealing at 400˚C for 12h, the defects responsible for these emissions were not removed and instead continue to increase in density. This corresponds to the increased PL observed for the 12 h oxygen anneal (Figure 4.20). As the XEOL is strongly linked to surface emissions it was deduced that the disorder corresponds to this region. Therefore, the increased disorder in this region is linked to the increasing quantity of V_{Zn}^{2-} forming on the nanorod surface during the prolonged anneal in the high oxygen partial pressure environment.

The final observation for the data collected was the bond lengths for each orbital obtained in TM and OM, are shown to be within 0.01 Å of each other with minor exceptions. This consistency and the closeness of the fit to the wurtzite model, strengthen the reliability of this technique.

4.7 Summary

A thorough characterisation and detailed analysis was conducted on ZnO nanorods synthesised using two aqueous chemical solutions: a very weakly acidic pH 6 solution and a high ammonia-based pH 11 solution. The main difference between the growth solutions was shown to be the heterogeneous growth rate; this had a significant impact on almost all the ZnO material properties due to unreacted precursors on the surface and encapsulated throughout the nanorod bulk. This was demonstrated by the morphological and crystallographic changes during the anneal process. The presence on precursor material was further supported by Raman spectroscopy, which also revealed that the ZnO nanorods were doped with nitrogen-related defects during the anneal process. Upon UV excitation the nanorods exhibited strong green PL emission that was dependent on the annealing atmosphere. After reviewing the available theoretical and experimental analysis on this subject and relating it to the obtained results, it was inferred that V_{Zn}-related defects are most likely responsible for the observed green luminescence.

Finally, the pH 11 ZnO nanorods were used to successfully demonstrate for the first time the effectiveness of EXAFS analysis in optically-detected mode to distinguish between different structural regions. Red (660 nm) emission was confirmed to originate from surface defects, while the green (500 nm) emission was linked to defects on Zn sites.

5 Influence of p-type material on device performance

One of the main challenges faced by those using copper (I) thiocyanate (CuSCN) is that of deposition (see section 2.2.1.2). This chapter demonstrates the development and analysis of a technique used to resolve this issue. A direct comparison was performed between the widely-used impregnation technique, and the spray-deposition technique developed here. Morphological, crystallographic, and optical properties were investigated using SEM, GIXRD, and optical absorption measurements. To demonstrate the effectiveness of the spray-method, purely inorganic heterostructured ZnO nanorod-CuSCN diodes were fabricated to assess the pore-filling ability, electrical stability, and performance.

Inorganic CuSCN was compared with a hole collecting polymer, PEDOT:PSS in order to analyse the variances and effect of p-type material on performance. The purely inorganic (ZnO-CuSCN) and hybrid (ZnO-PEDOT) devices were tested as photodiodes, and the photocurrent and response times to UV illumination were examined.

5.1 Copper (I) thiocyanate deposition

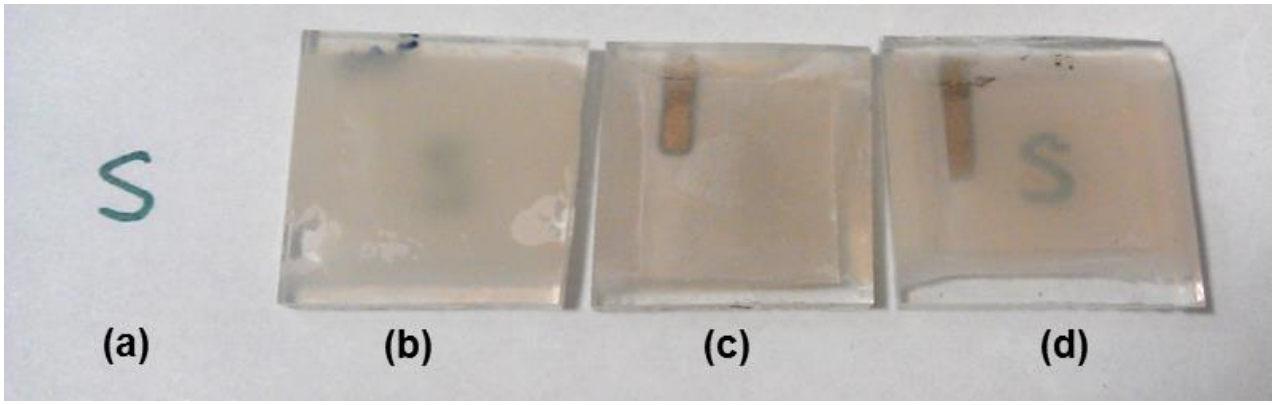

Figure 5.1 Photograph of a) no sample present, b) FTO-ZnO nanorods, c) ZnO nanorods-CuSCN-Au impregnaion coated, and d) ZnO nanorods-CuSCN-Au spray-coated with Au electrode.

The above photograph shows the development of ZnO-CuSCN devices with uncoated ZnO nanorods (Figure 5.1b) and after CuSCN deposition using impregnation (Figure 5.1c) and spray-coating (Figure 5.1d). A visible difference in the sample transparency is observed between the two techniques, where the letter ‘S’ is visible after spray-coating but not after

impregnation. The reasons for this and its impact on device performance are discussed in the following section.

5.1.1 Impregnation deposition

The impregnation technique is one of the most widely-used deposition methods for CuSCN and is detailed in section 3.1.4.1. As discussed in section 2.2.1.2, it was often reported that cracks form in the p-type layer due to the slow evaporation of solvent. Initial attempts at depositing the CuSCN using this method are shown here.

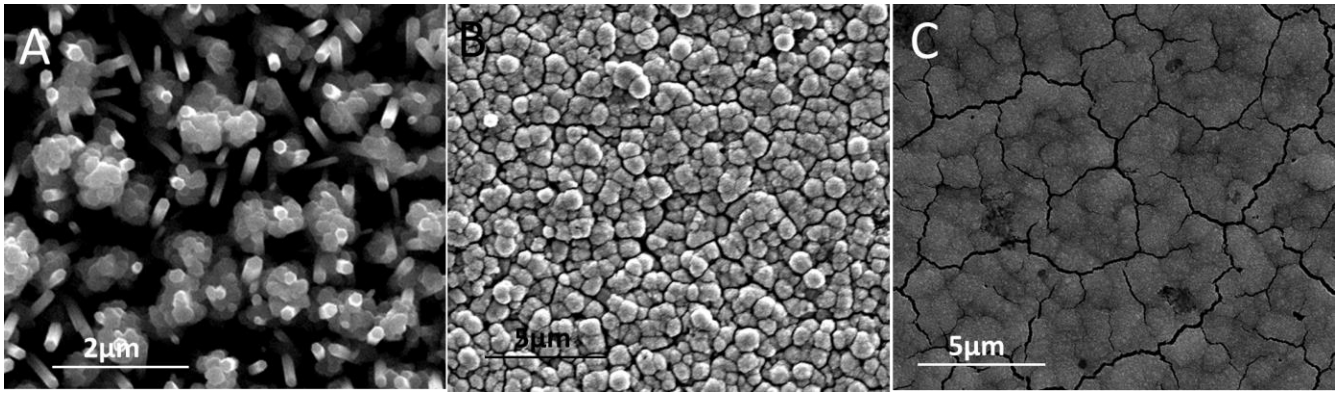

Figure 5.2 SEM micrographs of CuSCN deposited onto ZnO nanorods via the impregnation technique, A) 10 layers, B) 24 layers, and C) 48 layers.

Large clusters of CuSCN particles, 100-300nm in diameter, were observed to adhere to the nanorod surface after 10 layers (Figure 5.2A). Additional layers resulted in disconnected CuSCN islands in close formation rather than a smooth film (Figure 5.2B). After 48 layers a smoother film appears, but crevices 100-500 nm wide form a network across the entire surface (Figure 5.2C). These cracks would often cause the completed devices to short as the sputtered Au electrodes would penetrate between the gaps and contact the ZnO-FTO surface.

Optimizing the process using longer intervals between depositions and periods of higher temperatures (150˚C) for 10-15 minutes resulted in fewer cracks from forming. However, unless the impregnation deposition is performed by an automated robot it involves a number of limiting factors. For example, the delicate nanostructured surface is at risk of being damaged by the glass pipette during the deposition and requires the pipette to be controlled with precision. Control over the droplet is limited to the pressure applied to the nipple and movement of the pipette. This often results in excess solution being deposited causing white precipitate to form. This forms an opaque sample as shown in Figure 5.1c, due to the

scattering of photons. In this case it indicates either a rough CuSCN surface and/or unsaturated pores in the nanorod-array.

Consequently, it was decided that for the project to move forward the number of device failures needed to be minimised. This required an improved method for CuSCN deposition and led to two methods being tested: spin-coating and spray-coating.

5.1.2 Spin-coating

The spin-coating method used for this process is detailed in section 3.1.4.1. The 0.2 M CuSCN solution was deposited drop-wise using a pipette onto the rotating ZnO sample. The sample was heated to ~80˚C using a heat lamp.

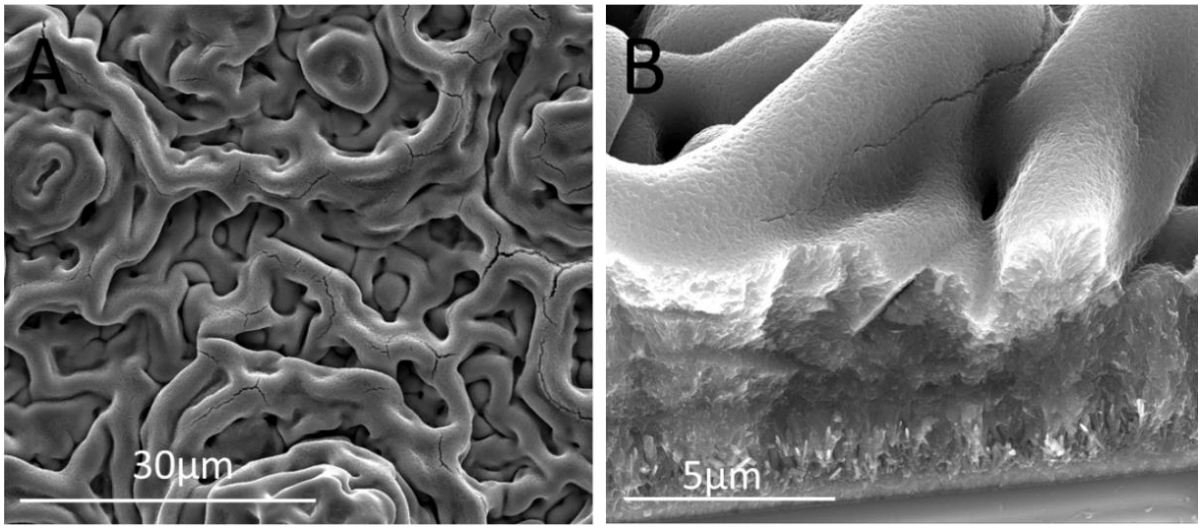

Figure 5.3 SEM micrographs of CuSCN deposited onto ZnO nanorods using the spin-coat method A) top-down and B) cross -section view.

After the CuSCN solution saturated the array, the sample rotation led to thin layers of CuSCN accumulating on top. The ripple effect of the CuSCN layer shown in Figure 5.3A was linked to the n-propyl sulfide (n-PS) partially re-dissolving the CuSCN before evaporating. The sample rotation leads to the CuSCN solution producing peaks and troughs that lead to the appearance observed in Figure 5.3A. In this case, 20 drops of CuSCN solution resulted in a layer 5-7 µm thick that would likely cause increased series resistance (Figure 5.3B). This process may be optimised by reducing the total quantity of CuSCN deposited and investigating the ideal spin-rate. However, the unevenness of the top surface and presence of cavities up to 2 µm in size suggest this process is not suited to device processing. Furthermore, it does not have the benefit of scalability.

5.1.3 Spray-deposition

An alternative approach of using a fine-mist of CuSCN solution to coat the nanorod array was considered. Initially this was performed using a commercial aerosol bottle, but when the first tests proved promising a pneumatic spray-gun was used. This allowed the adjustment of the nozzle size that controlled the mist dispersion and an air compressor was used to regulate the pressure with which the spray was generated. The spray-deposition was conducted in a fume-hood due to the pungent n-PS smell. However, the strong ventilation caused the spray to be misdirected. To overcome this, a shield was erected between the hotplate and the air-vent. Furthermore, the initial sputter was not directed onto the sample as this often consisted of larger droplets. The side-to-side sweeping motion allows multiple samples to be coated at once, and gives time for the n-PS to evaporate from the deposited droplets. A detailed account of the deposition process is given in section 3.1.4.1.

When performed correctly, the CuSCN spray deposition shows no visible differences in the sample appearance until the final stages. The deposition is complete when the ZnO sample changes from grey and opaque (Figure 5.1b) to a transparent/reflective surface (Figure 5.1d). This is representative of the CuSCN solution penetrating into the nanorod array and filling the pores that give rise to photon scattering.

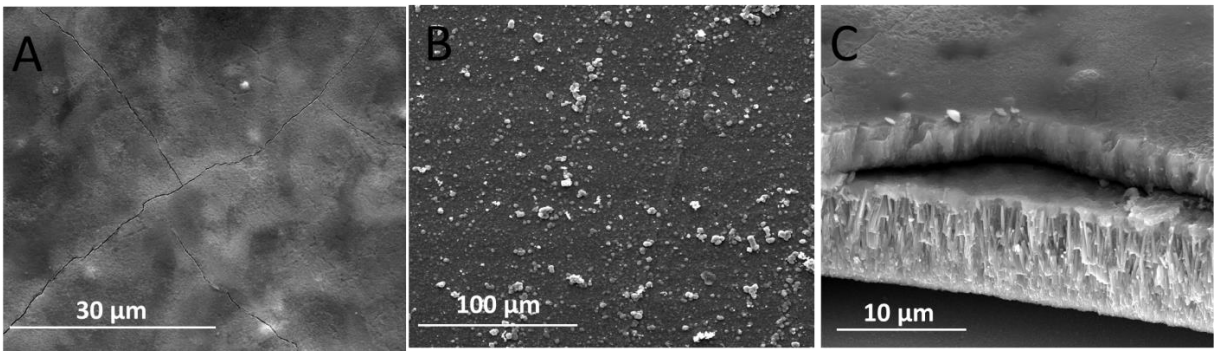

Figure 5.4 SEM micrograph of CuSCN deposited via spray-coating top-down view of A) shorter spray intervals, B) excess CuSCN deposition, and C) cross-section view.

When refining this technique, it was found that if insufficient time is given for the n-PS to evaporate thin cracks will form in the CuSCN layer (Figure 5.4A). In addition, if too much CuSCN is deposited during one spray interval, a white precipitate will form on the surface. This is indicative of large CuSCN particles up to 1-2 µm in diameter forming clusters on the surface and prevents the CuSCN-spray from penetrating deeper into the array (Figure 5.4B). This results in an uneven surface that does not provide optimal coverage and increases the

contact resistance. Therefore, for the spray-coat method to be effective, depositing excess CuSCN solution must be prevented and the drying intervals between sprays maintained.

The thickness of the CuSCN layer is not known unless an SEM cross-section is taken. The amount of CuSCN to be deposited is dependent on the porosity of the array and the concentration of CuSCN solution used. It was found that non-saturated CuSCN solutions required additional layers, for example a 0.1 M solution would take twice as many sprays to complete than a saturated 0.2 M solution. This was linked to less CuSCN present in each spray-deposition, and the increased quantity of n-PS solvent required longer intervals between sprays. Therefore, the optimal processing conditions required a saturated CuSCN solution.

5.1.4 Morphological, crystallographic, and optical analysis

Morphological differences between the spray-coating and impregnation techniques were assessed using SEM analysis. CuSCN is not highly conductive, which means the electron beam would distort the material if a high voltage is applied. Hence, a lower accelerating voltage of 10 keV was chosen for the SEM analysis. Section 2.2.1 described the problems non-ideal CuSCN morphology can cause, for example increased series and contact resistance of the CuSCN layer, and more critically complete device failure due to shorts. Here, the significant impact morphology and pore-filling has on the device performance is established.

The spray-deposition was shown to produce a high density of evenly distributed 40 nm CuSCN grains on the nanorod surface (Figure 5.5-B1); while impregnation generated sporadic coverage of 120 nm grains (Figure 5.5-A1). It would be expected that larger grains of CuSCN would offer a lower series resistance due to the lower number of grain boundaries. However, because the evaporation of n-PS is a slow process [276] this leads to voids between CuSCN grains, which increases the series resistance of the material. The spray-gun used here generates a 0.2 μm fine-mist of the saturated CuSCN solution. This allows evaporation of n-PS to occur prior to contacting the ZnO surface. Consequently, the mist consists of small supersaturated droplets of CuSCN solution that nucleate on contact with the heated surface. Once nucleated, rapid evaporation of the remaining n-PS will occur and leave behind crystalline CuSCN. This drastically minimises the amount of n-PS trapped in the grains and leads to a compact, uniform coverage of CuSCN over the ZnO nanorods as evidenced by Figure 5.5-B2.

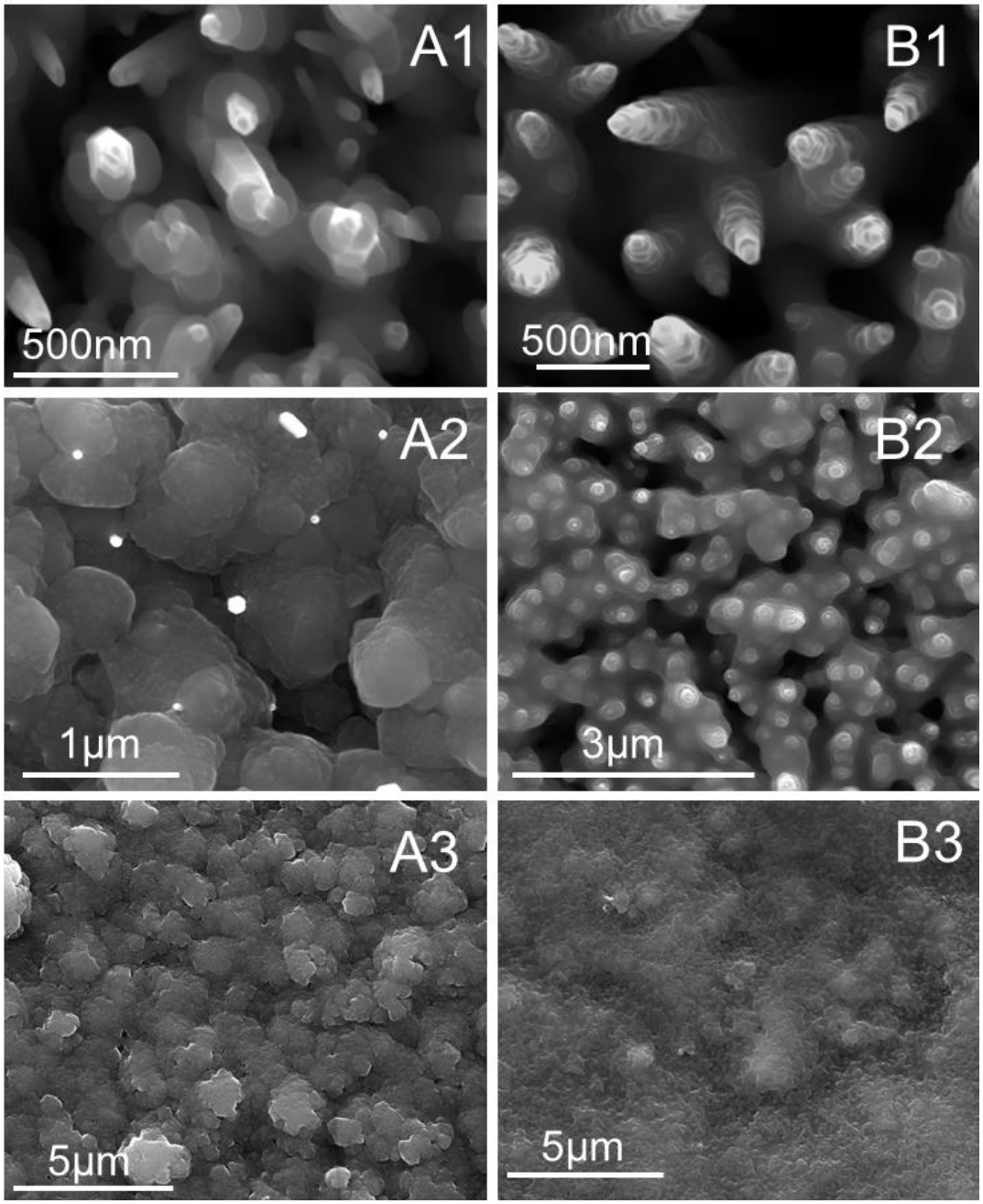

Figure 5.5 SEM micrographs of the CuSCN layer at the initial, intermediate and final stages of deposition for A1-3) impregnation and B1-3) spray-coating.

ZnO-CuSCN diodes fabricated using the CuSCN impregnation technique, show a change in performance over time. This was assigned to the slow evaporation of n-PS that typically requires the sample to be stored in vacuum for up to two days [172,194]. In the case of spray-deposition the device performance did not change significantly over the time, i.e. a device tested within minutes of the CuSCN coating performed in a similar manner to a nine-month old device. This demonstrates that very little n-PS was trapped in the CuSCN grains during the spray-deposition.

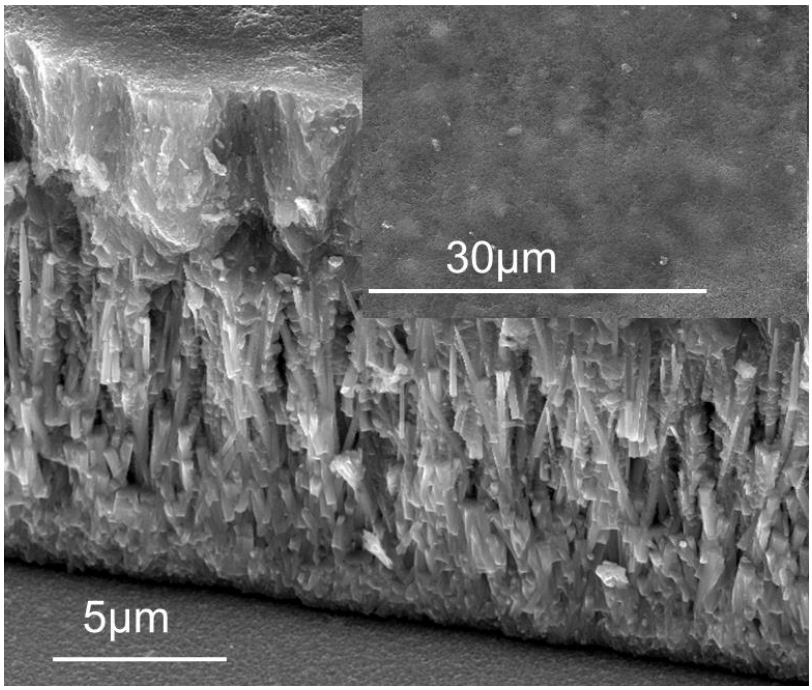

Figure 5.6 SEM micrograph showing the cross-section of CuSCN coated ZnO nanorods and inset of the top-down view after 150 sprays.

Deposition is complete when a smooth top-surface was observed by eye, and appeared reflective under light. For Figure 5.5-B3 this required 150 spray steps; it was however dependent on the volume of pores in the nanostructure. SEM analysis shows no observable mud-cracks in the CuSCN layer (Figure 5.6 inset). Furthermore, the removal of drying steps during the processing and the storage time typically required to generate acceptable device performance, has significantly simplified and increased the speed of device production. For comparison, bare nanorod surfaces and cavities between CuSCN grains were observed for impregnation-deposition (Figure 5.5- A2). The irregular grain-sizes and sporadic coverage led to a rough top-surface, which would contribute to the opaqueness observed in Figure 5.1c. Spray-deposition produced good pore-filling of the ZnO nanorods, maximising contact at the ZnO-CuSCN interface (Figure 5.6). However, high density and irregular alignment of the nanorod array prevents the CuSCN mist from penetrating to very base of the nanorods; this is evidenced by the unsaturated pores at the base of the array (Figure 5.6).

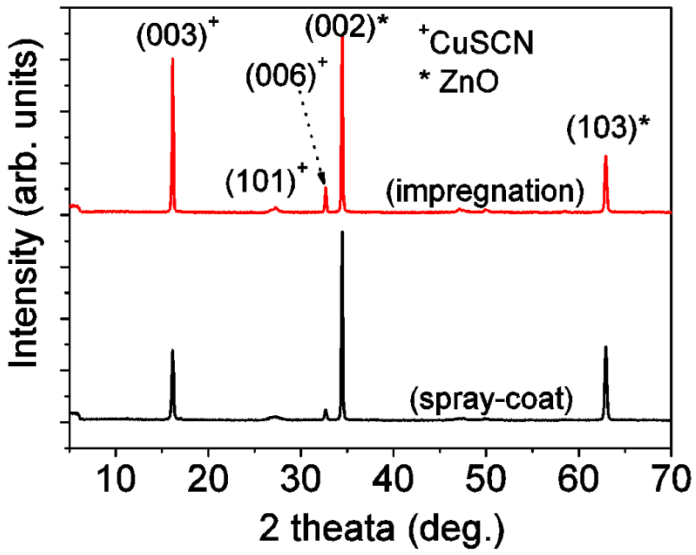

Figure 5.7 Glancing incidence XRD (off-set in y-axis) for ZnO nanorods coated with CuSCN using the spray-coating and impregnation techniques. Where $^{+}$ represent CuSCN peaks and * are assigned to ZnO peaks.

GIXRD analysis of the ZnO-nanorod/CuSCN heterostructure confirms the peaks match those of β-phase CuSCN (JCPDS 29-581) and the wurtzite structure of ZnO (JCPDS 79-0207) (Figure 5.7). The full-width half-maximum (FWHM) of the XRD peaks provides information regarding the grain-size at specific orientations. These are presented in Table 5-1.

Table 5-1 Full-width half-maximum (FWHM) values from the GIXRD data shown in Figure 5.7.

XRD Peak (˚)		**FWHM (˚)**	
		Impregnation	*Spray*
003 (16.16)	CuSCN	0.165	0.218
006 (32.69)	CuSCN	0.180	0.255
002 (34.46)	ZnO	0.166	0.169
103 (62.90)	ZnO	0.267	0.271

Table 5-1 confirms there is minimal difference between the ZnO-nanorods coated in each sample. This supports the proposal that variations in device performance primarily arise from the CuSCN layer. The FWHM of the spray-deposited XRD peaks are 24-30% wider than that the impregnation peaks. This is consistent with the significantly smaller grain-sizes observed in the SEM analysis for spray-deposited CuSCN (Figure 5.5-B1).

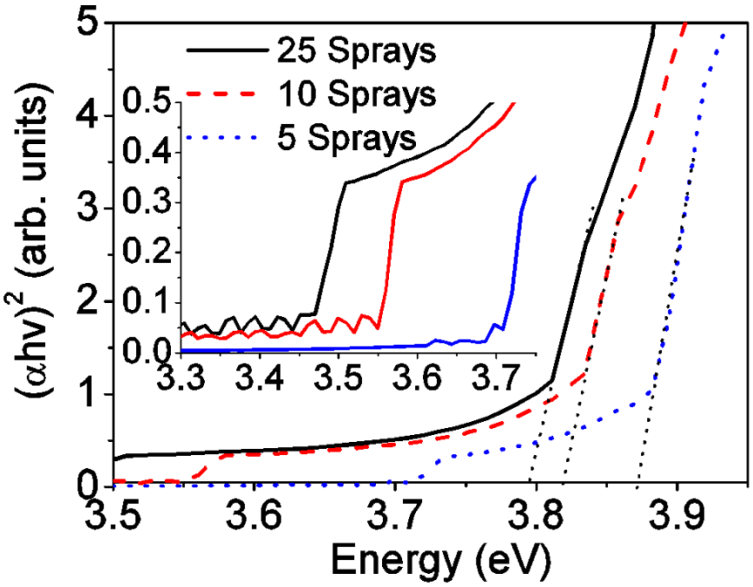

Figure 5.8 A Tauc plot of thin-film CuSCN after 5, 10 and 25 spray-depositions, with inset highlighting interference fringes. Dotted-line represents the optical band-gap associated with each deposition.

CuSCN was spray-deposited onto cleaned glass substrates with a range of film thicknesses (100 - 700 nm). The control over the deposition rate/thickness was demonstrated by the incremental decrease in optical band-gap from 3.87 eV to 3.79 eV, gradually approaching the bulk bandgap of CuSCN 3.6 eV (Figure 5.8). Thin-film interference fringes were observed to occur prior to the absorption onset (inset Figure 5.8) and confirms the uniformity and evenness of films deposited onto the glass substrate.

5.1.5 Electrical testing

Hall Effect measurements were performed to assess the conductivity of spray-deposited CuSCN films (see experimental section 3.2.8). CuSCN film-thickness was determined using an SEM cross-section view of the sample. For a 6 µm-thick film, Hall mobility was measured to be 70 $cm^2/V.s$, the highest reported to date, with a hole carrier density of $1.6x10^{13}$ cm^{-3}. Conductivity was calculated to be 0.02 $S.m^{-1}$. This value is comparable to those previously reported for undoped CuSCN [185,277]. The high mobility reported here, substantiates the impact morphology has on the material properties. Although the CuSCN grain-size is smaller than that of impregnation, this is counteracted by the dense and compact nature of the film.

A direct comparison of the Hall Effect measurement was not possible for the impregnation technique. The inability of the CuSCN solution to readily wet the heated glass surface led to a streaky residue instead of a thin-film. In addition, any further applications of the solution re-

dissolved the CuSCN present on the surface. This renders the impregnation process unsuitable for depositing thin-films on surfaces with a low roughness factor.

Spray-deposited films were therefore compared to literature values for previous CuSCN films. The fact that the CuSCN spray readily coated the glass surface is further evidence that a supersaturated droplet of n-PS/CuSCN is being produced. The interfacial reaction of the supersaturated droplet is not governed simply by the n-PS but a combination of the surface interactions of the CuSCN and n-PS. The ability to uniformly coat and adhere to surfaces with a low roughness factor is another advantage of the spray-coat technique.

The electrical testing was performed as described in the experimental section 3.2.9. The ZnO-CuSCN diodes were tested on the day fabrication was completed, i.e. after the CuSCN deposition and Au electrode was sputtered.

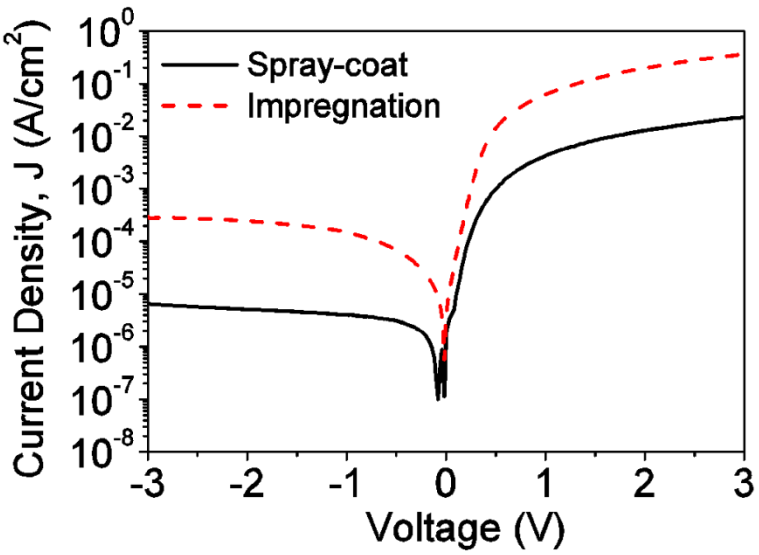

Figure 5.9 Semi-log J-V curve of a ZnO-nanorod/CuSCN diode, deposited via spray-coating (solid-line) or impregnation (dashed-line).

A semi-log J-V plot obtained under the same conditions for both impregnation and spray-deposition is shown in Figure 5.9. Rectifications of 1240 and 3550 at ±3 V were exhibited for impregnation and spray-coating, respectively. The spray-deposition achieved approximately three times the rectification than the alternative method of impregnation. Furthermore the spray-deposition has a dark current-density of 7 $\mu A/cm^2$ at -3 V, which is an order of magnitude less than the impregnation technique. This was linked to significantly fewer shorts in the device that contribute to the leakage current.

The enhanced performance is primarily attributed to the improved pore-filling that results in increased interfacial contact with the ZnO-nanorods and assists in charge carrier separation. Secondly, the reduced contact resistance between the top Au-electrode and the smooth CuSCN layer improves the mobility of carriers into the top electrode. Lastly, the high carrier mobility (70 cm^2/V.s) demonstrated by Hall Effect analysis is assigned to the absence of insulating gaps in the CuSCN layer caused by the slow evaporation of n-PS solvent. These rectifications are approximately ten times better than those previously reported for ZnO-CuSCN diodes [180], and the same order of magnitude as recent NiO-ZnO p-n-heterojunctions at an applied bias of 1 V [278].

5.2 Hybrid ZnO-photodiodes using PEDOT:PSS

PEDOT:PSS is a conductive polymer (1 $S.cm^{-1}$) with a bandgap of 1.6 eV and good optical transparency to the visible region, which makes it a suitable hole collector for optoelectronic devices. ZnO-nanorods synthesised using the pH 6 method was spin-coated with PEDOT:PSS to fabricate a hybrid photodiode. In attempt to improve penetration of the polymer into the nanorod array, three PEDOT:PSS solutions were tested: undiluted in its aqueous form, and diluted in acetone using 1:5 and 1:10 volume ratios.

5.2.1 Device fabrication

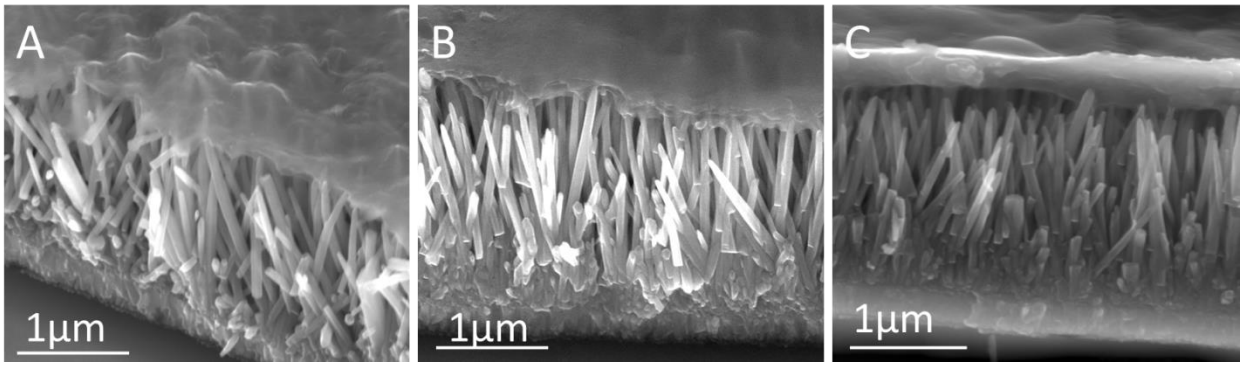

Figure 5.10 SEM cross-section micrographs taken at a 45˚ tilt showing ZnO-nanorods coated with PEDOT:PSS that was A) undiluted, B) diluted in 1:5 acetone, and C) diluted with 1:10 acetone.

Both ZnO and PEDOT:PSS are hydrophilic in nature and so it would be expected that they would easily bond. However, the network of PEDOT:PSS polymer chains form large grains of ~1 µm, which prevents the polymer from penetrating below the nanorod tips into the narrow pores. Therefore the PEDOT:PSS layer 'floats' on top of the nanorod array, which reduces the interfacial contact between the ZnO and PEDOT:PSS layer (see Figure 5.10A).

The PEDOT:PSS was diluted (1:5 and 1:10) in acetone in attempt to improve the penetration depth. Instead this was found to achieve to opposite effect and reduced the penetration further (Figure 5.10B and C). This was attributed to the acetone dissolving the PSS coating, which led to an increase in PEDOT grain size.

5.2.2 Electrical testing

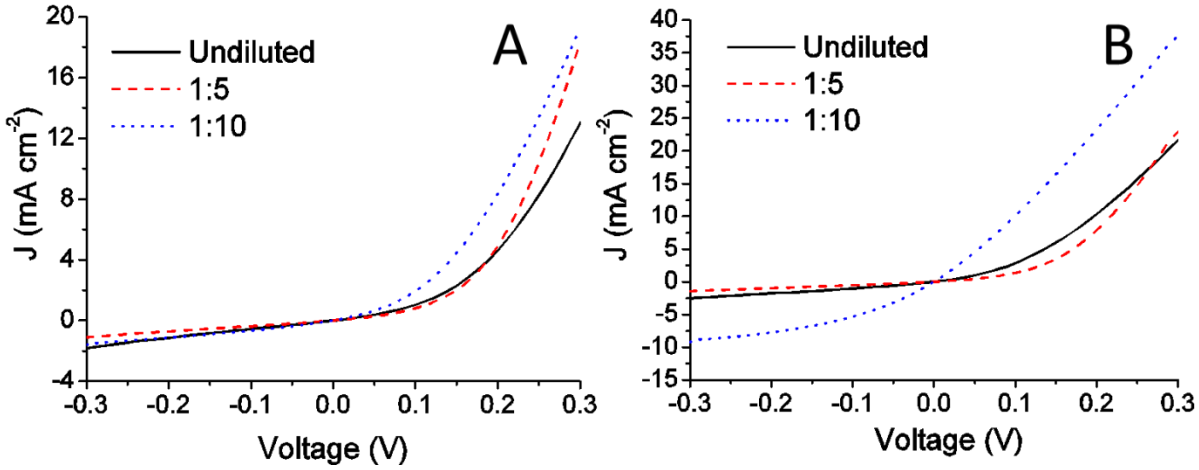

Figure 5.11 J-V plot of ZnO-PEDOT:PSS photodiodes in A) dark and B) AM 1.5 conditions.

Table 5-2 Rectification ratios of ZnO-PEDOT:PSS diodes extrapolated from Figure 5.11.

Rectification @ ± 0.3V	Undiluted PEDOT	1:5 PEDOT-Acetone	1:10 PEDOT-Acetone
Dark	7	17	12
AM 1.5	9	16	4

The hybrid photodiode was tested under dark and AM 1.5 conditions. Increased forward current density was observed for the acetone diluted 1:5 and 1:10 samples (Figure 5.11A). This gives evidence to support the removal of insulating PSS from the conductive polymer. The 1:5 and undiluted PEDOT:PSS show similar rectifications under dark and AM 1.5 conditions (Table 5-2) and indicates poor charge separation at the interface. The 1:10 diluted sample exhibits the greatest difference in rectification between the dark and illuminated conditions, this is attributed to the improved hole mobility caused by fewer insulating PSS boundaries in the PEDOT layer. ZnO nanorods used to fabricate these devices were synthesised simultaneously to ensure the observed variances primarily originate from the PEDOT:PSS.

5.3 A performance comparison of hybrid and purely-inorganic photodiodes

A direct comparison was performed in this section between four devices; ZnO grown using pH 6 and 11 solutions (annealed in air), and the two p-type materials CuSCN and PEDOT:PSS. The device performance will be investigated and related to the differences in the device structure and properties of the ZnO nanorods.

SEM cross-sections present a significant morphological difference between the hybrid and purely-inorganic devices. Inorganic CuSCN was shown to saturate the porous array (Figure 5.6), whereas organic PEDOT:PSS was suspended on the nanorod tips above the array (Figure 5.10). As a result, the ZnO-CuSCN device has high interfacial contact between the p- and n- type materials, and the ZnO-PEDOT hybrid device has a high surface area of exposed nanorods.

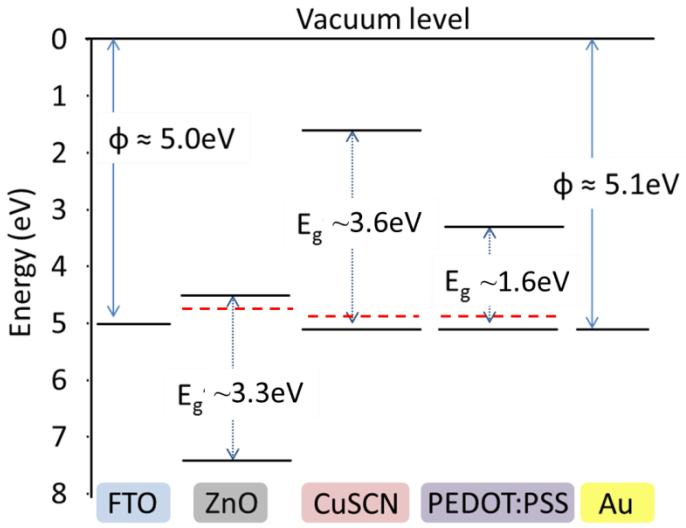

Figure 5.12 An energy-band diagram of the materials used to fabricate the purely-inorganic and hybrid photodiodes, red dashed-lines indicate the E_F.

CuSCN and PEDOT:PSS were chosen for this experiment as their E_V and HOMO level have similar off-sets to the ZnO E_V (Figure 5.12). Under equilibrium the energy-bands will not shift significantly due to the pre-existing alignment of the E_F. Hence, under a small reverse-bias it would be possible for electrons to tunnel from the p-type E_V/HOMO into the ZnO E_C, leading to an increase in leakage current.

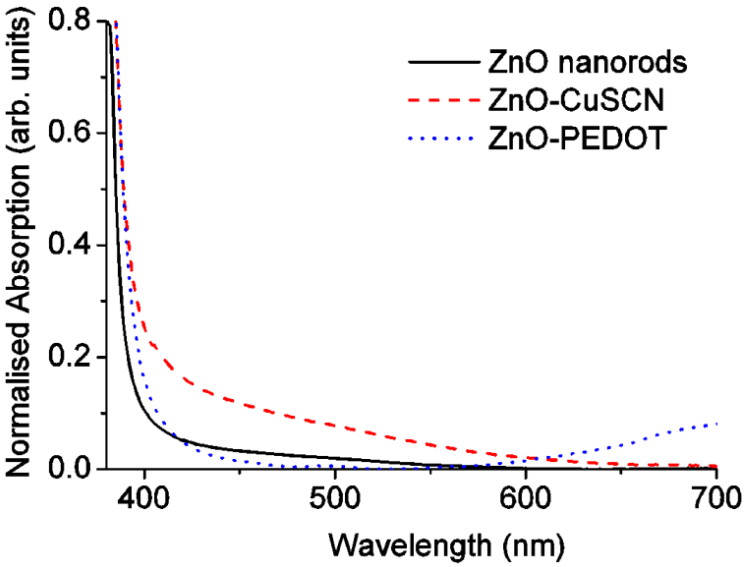

Figure 5.13 Normalised UV-Vis absorption spectra of plain (pH 11) ZnO nanorods, and nanorods coated with CuSCN or PEDOT:PSS.

Analysing the devices using UV-Vis absorption confirms they both function as UV photodiodes, absorbing wavelengths < 400 nm (Figure 5.13). In addition, ZnO-CuSCN was shown to exhibit partial absorption in the visible region up to 600 nm. This can be attributed to interactions at the ZnO-CuSCN interface as both the ZnO and CuSCN separately show the absorption onset in the UV region. This would result in the photodiode exhibiting a weak photoresponse to photos in this energy range. The ZnO-PEDOT diode demonstrates good visible-blindness up to 600 nm where it begins to increase.

5.3.1 Hybrid ZnO-PEDOT:PSS diode

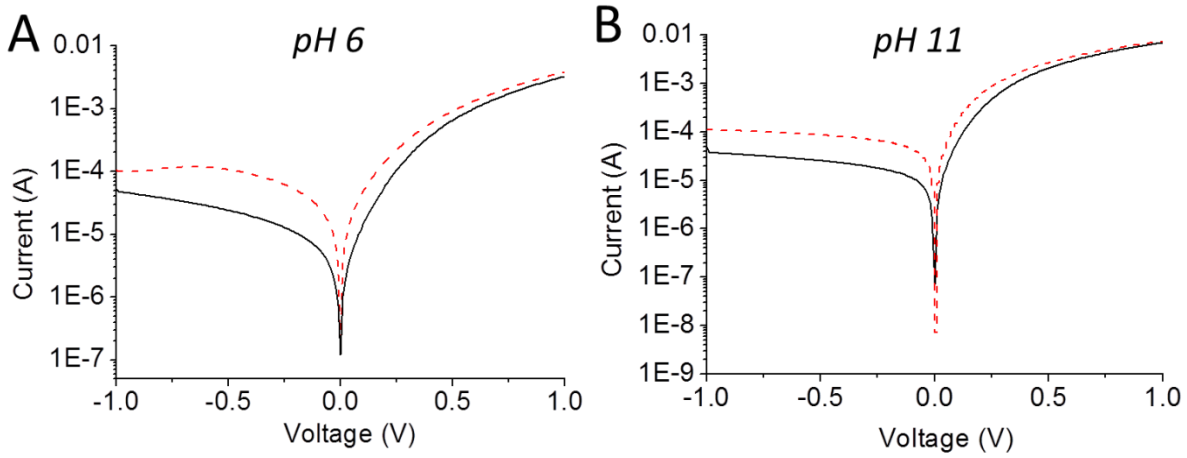

Figure 5.14 Semi-log I-V plot of ZnO-nanorods A) pH 6 and B) pH 11 coated with PEDOT:PSS (undiluted) in dark (solid-line) and AM 1.5 (dashed-line) conditions.

The semi-log I-V plots in Figure 5.14 show the forward and reverse current at ±1 V to be near identical in both dark and illumination conditions. Hence, the pH 6/11 nanorods do not play a significant role in determining the current obtained by this device. This is explained in terms of the conduction pathway through the device structure.

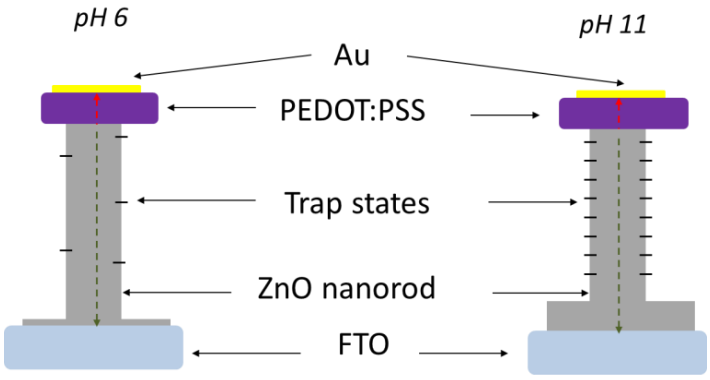

Figure 5.15 Schematic of the electron (green dashed-line) and hole (red dashed-line) pathway through a pH 6/pH 11 ZnO nanorod-PEDOT:PSS diode.

In both devices, the photoexcited electrons transition through the ZnO nanorod to the FTO electrode and the holes to the Au electrode (Figure 5.15). However, holes generated in the ZnO nanorod migrate to the surface due to the upward band bending (see section 2.1.4.4). Here they assist in the release of adsorbed O_2^- ions, or recombine with mobile electrons in the ZnO bulk. It is therefore only photoexcited carriers generated close to the ZnO-PEDOT interface that contribute to the photocurrent generated by the device.

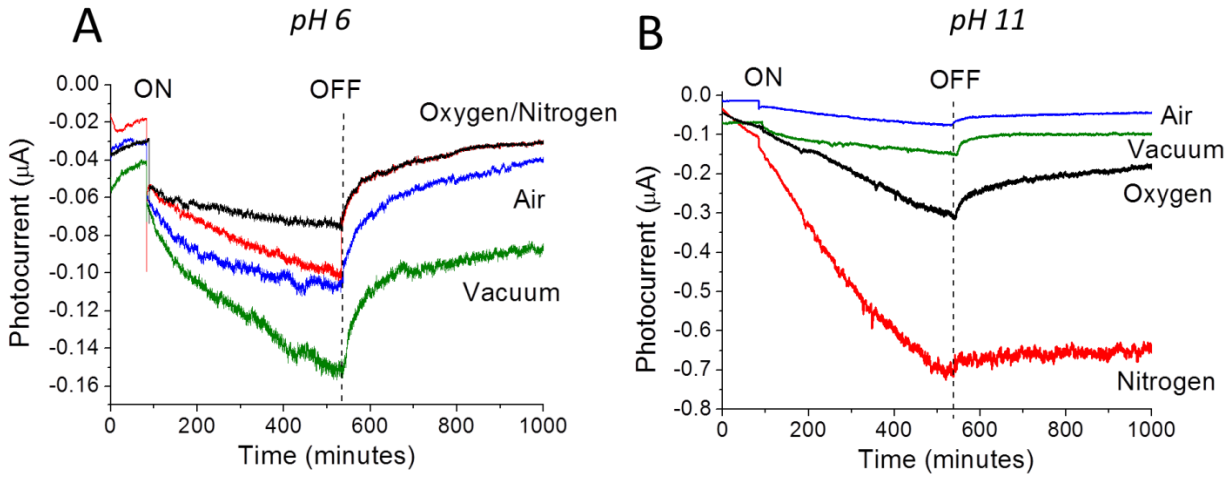

Figure 5.16 Photocurrent measurements of A) pH 6 and B) pH 11 synthesised ZnO nanorods coated with PEDOT:PSS operating at ~0 V and illuminated under 15 mW cm^{-2} 380 nm irradiance for ~ 7.5 h under various gas atmospheres.

The photocurrent exhibited by the hybrid devices was unstable for all atmospheres and failed to reach equilibrium even after several hours of UV illumination (Figure 5.16). Two stages were shown for the photocurrent, firstly a rapid switch-on (~0.1 ms) when the device was first illuminated, and secondly a gradual increase for the duration of illumination. The continual increase in photocurrent was attributed to the exposed nanorod surface that allowed the oxygen adsorbed on the surface to continually photo-desorb and re-adsorb. The current slowly decays once the UV is switched-off; but even after a one-day period in the dark the device did not reach an equilibrium state. Figure 5.16A shows a maximum variance in photocurrent of ~0.1μA, and this is after 7.5 h of illumination. This small difference was linked to the gases having to diffuse through the PEDOT:PSS to access the nanorod surface, and explains the prolonged recovery time which requires oxygen to diffuse through the PEDOT to reabsorb onto the ZnO surface. This is evidenced by the highest photocurrent arising from measurements obtained in vacuum. Similarly with the pH 11 photodiode shown in Figure 5.16B, significant differences between atmospheric conditions was not observed until hours later. A photocurrent of 0.7 μA was reached under nitrogen gas, followed by 0.3 μA in oxygen. This difference in diode behaviours must be related to the exposed pH 11 nanorod surface. Firstly, the pH 11 nanorods are ~8 μm longer than pH 6 rods presenting a larger surface area for gas reactions. Secondly, Chapter 4 demonstrated these nanorods have a large number of surface defects present that may react differently compared to pH 6 rods.

Lastly, it should be noted that these devices did not perform consistently during the experiment. This may be due to redox-reactions in the PEDOT:PSS affecting the material properties over time (see section 2.2.2.1), or prolonged testing under UV illumination causing photo-degradation.

5.3.2 Purely-inorganic ZnO-CuSCN diode

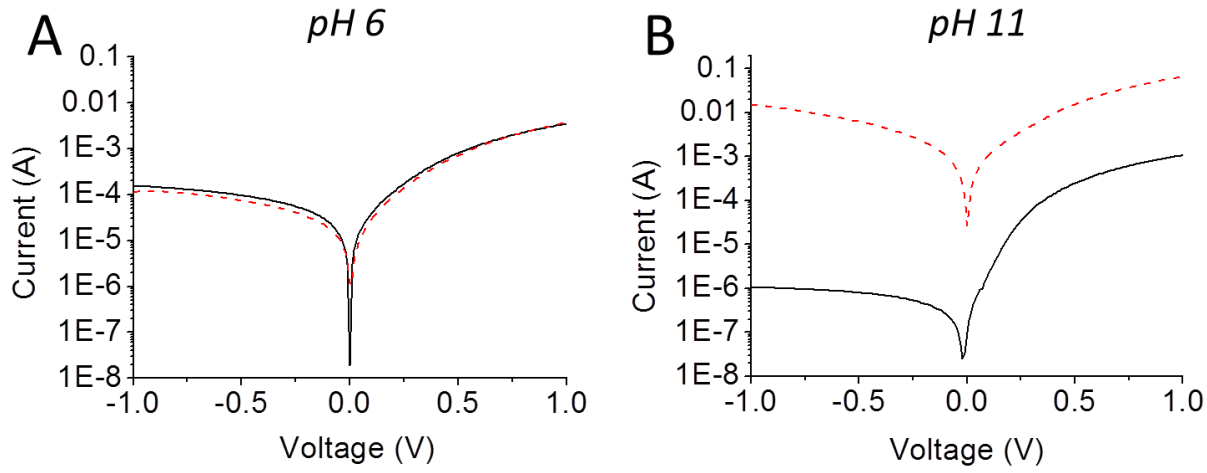

Figure 5.17 Semi-log I-V plot of ZnO-nanorods A) pH 6 and B) pH 11 coated with CuSCN in dark (solid-line) and AM 1.5 (dashed-line) conditions.

The pH 6 photodiode exhibited a minimal response when compared to the pH 11 photodiode, which showed a photosensitivity $>10^4$ at -1 V (Figure 5.17). This indicates the nanorods play a major role in determining the photocurrent response. The high leakage current of the pH 6 diode is attributed to the CuSCN penetrating to the base of the nanorod array and contacting the FTO electrode. Consequently, the conduction pathway effectively by-passes the nanorod and so the current has little dependence on the nanorod resistivity resulting in a low UV response (Figure 5.18). This is avoided in the case of the pH 11 diode due to the fused ZnO layer at the base of the array, forcing carriers to conduct through the ZnO resulting in the lower leakage current of ~1 μA (Figure 5.17B).

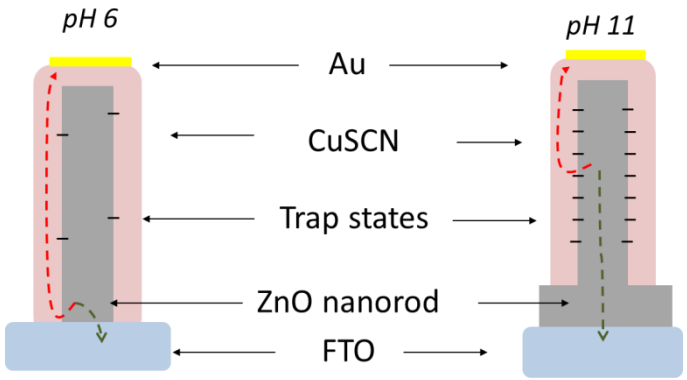

Figure 5.18 A schematic showing the electron (green dashed-line) and hole (red dashed-line) conduction pathway through a pH 6/pH 11 ZnO nanorod-CuSCN diode.

The schematics in Figure 5.18 illustrate the CuSCN coating the entire nanorod. It was expected that this would reduce the atmospheric effect on the photoconductivity since oxygen only photo-desorbs from exposed ZnO surfaces. Figure 5.19 however shows some variance in photocurrent still remains relating to the atmosphere. This may be linked to areas at the base of the ZnO array that have not been coated by the CuSCN and so remain exposed to the atmosphere.

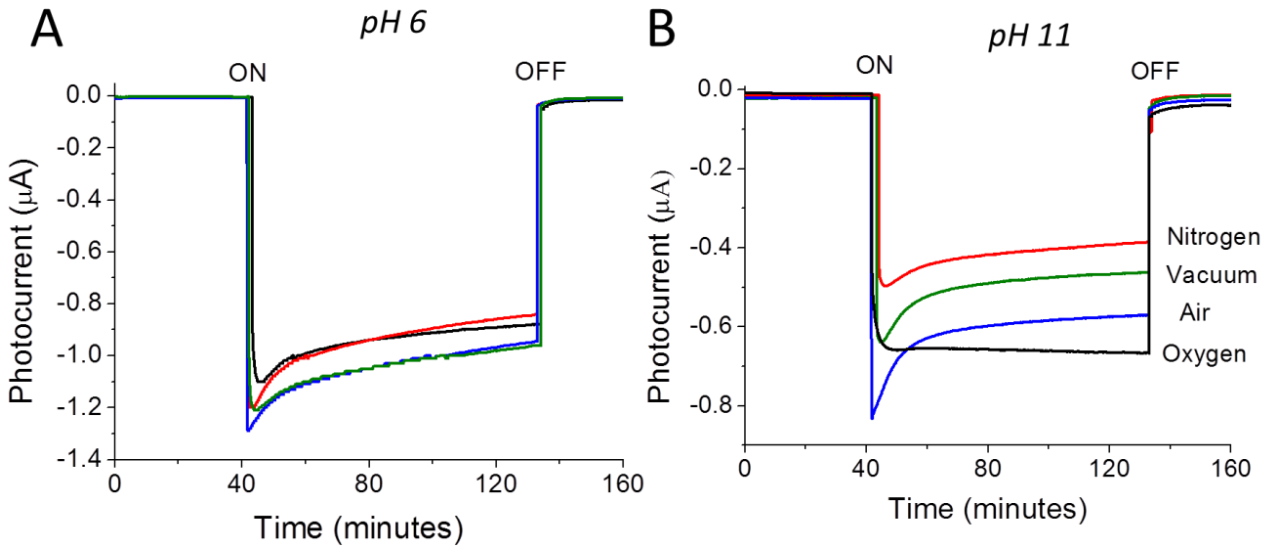

Figure 5.19 Photocurrent measurements of A) pH 6 and B) pH 11 synthesised ZnO nanorods coated with CuSCN, operating at ~0 V and illuminated under 15 mW cm^{-2} 380 nm irradiance for ~100 minutes under various gas atmospheres.

The pH 6 and pH 11 ZnO-CuSCN devices are shown to possess relatively stable photocurrents that exhibit switch-on/off response times < 0.1 ms. The photocurrents are close together for the pH 6 photodiode confirming the atmosphere plays a minimal role in the photocurrent. However, for the pH 11 photodiode where ZnO nanorods remain exposed at the base result in a more discrete response between the atmospheres. Generally the photocurrent was highest in the presence of oxygen, which is expected due to the influence oxygen desorption has on ZnO photoconductivity (Figure 5.19B). With the exception of oxygen in Figure 5.19B, the photocurrent was shown to gradually decrease over time. This is related to excited carriers reaching equilibrium between photoexcited carriers being generated and carrier recombination. Photocurrent of the pH 11 diode is approximately half that of the pH 6 diode and is linked to the increased number of recombination sites at the p-n interface.

5.4 Summary

Chapter 5 demonstrated the difficulties faced with typical impregnation of CuSCN. Alternative routes were proposed, namely spin-coating and spray-coating and these were explored as possible means to improve the process. Of the two processes spray-coating was selected for further analysis due to its reduction in crack formation and smooth surface. SEM analysis shows the spray-deposited CuSCN grain-size was ~40 nm and the particles coated the ZnO nanorod uniformly. The typical problem of 'mud-cracking' in the CuSCN layer was resolved by reducing the quantity of n-PS deposited and facilitating rapid evaporation of the remaining solvent. Optical analysis showed spray-coating provides enhanced controllability to the user allowing (100-700 nm) thin-films of CuSCN to be deposited on substrates with a low roughness factor.

A 6 µm-thick CuSCN film exhibited a conductivity of 0.02 $S.m^{-1}$ and the highest reported hole mobility of 70 $cm^2/V.s$. The ZnO-CuSCN diode (fabricated by the spray-coat technique) had a rectification of 3550 at ±3 V. This is up to ten times greater than those previously reported with a similar structure. By removing the long drying stages used in impregnation and the typical storage time required post-processing, the spray-coat method has reduced the processing time and made it possible to rapidly fabricate effective devices.

Although this technique has numerous advantages, there are also limitations. For example the pore-filling capability requires a direct pathway for the spray; this is because supersaturated CuSCN droplets nucleate on contact with the surface. Therefore, it may be unsuitable for sponge-like porous nanostructures.

Hybrid devices fabricated from spin-coating PEDOT:PSS onto ZnO-nanorods, resulted in the p-type material being suspended above the array, leaving the rods below exposed. This resulted in poor rectifications that were assigned to low interfacial contact and hence poor charge carrier separation.

Both PEDOT:PSS and CuSCN exhibited good absorption in the UV. When combined with n-type ZnO, the hybrid and inorganic heterostructures functioned as a UV photodiodes. The difference in performance was linked to both the device structure and nanorod properties. The hybrid photodiode exhibited photocurrent response in the range of 50-600 nA at 0 V, and the recovery times were dependent on the atmospheric condition. The ZnO-CuSCN photodiode exhibited higher photocurrent (0.4-1.3 µA) as a result of the increased interfacial contact at

the p-n junction. The recovery time of the inorganic diode was <0.1 ms, which is 10^5 times faster than the hybrid device.

In conclusion, the inorganic ZnO-CuSCN heterostructure represents the most promising option for further development in terms of stability, photocurrent intensity, and response times.

6 ZnO-nanorod based photodetectors

This chapter demonstrates the fabrication and performance of self-powered photodetectors using the ZnO nanorods characterised in Chapter 4. Employing ZnO nanorods in optoelectronic devices has the advantages of high surface-to-volume ratio, increased photon scattering, and a direct conductive pathway to the base electrode. Low-temperature aqueous processing was shown to play a significant role in determining the ZnO material properties, which directly affects the overall device performance. Here, the difference between pH 6 and pH 11 grown nanorods was investigated as part of a ZnO-CuSCN heterostructure. This heterostructure exhibits a small photovoltaic effect that allows it to operate as a self-powered UV photodetector near zero-bias. Furthermore, the ability to create photodetectors without high temperature processing will pave the way for flexible photodetectors. These devices were analysed in terms of stability, responsivity, spectral sensitivity, and compared to the best-performing photodetectors in this field

6.1 Self-powered pH 6 ZnO-nanorod/CuSCN photodetector

ZnO nanorods (pH 6) were spray-coated with CuSCN as detailed in experimental section 3.1.4.1. Chapter 5 demonstrated the improved pore-filling, morphology and hole-mobility of the CuSCN layer. The ZnO-CuSCN heterostructure has not previously been highlighted as a potential photodetector, but instead used to sandwich a dye or extremely thin absorber to fabricate DSSCs or PVs [193,276,279]. The importance of self-powered detectors was discussed previously in section 2.3.2.4, and it is shown here that this simple heterostructure that requires no encapsulation or additional processing to compete with those currently leading in this field.

6.1.1 Device structure

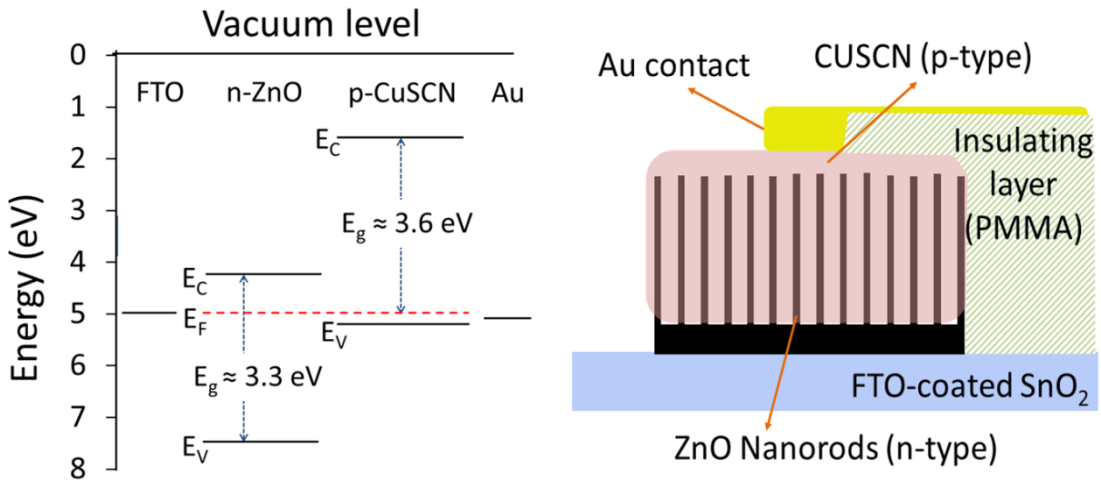

Figure 6.1 Energy band structure of the ZnO-CuSCN device shows the Fermi level alignment of this heterostructure, where E_C, E_V and E_F are the conduction band, valence band and Fermi level, respectively. The schematic opposite shows the complete device structure used for electrical testing.

Device performance is determined by the energy-band structure of the semiconducting materials. The offset between the ZnO E_F and work function of the FTO electrode (ϕ_{FTO}) dictates the open-circuit voltage (V_{OC}) and short-circuit current density (J_{SC}) under UV illumination. At equilibrium the energy-bands shift to accommodate the E_F pinning, however the pre-existing E_F alignment results in a minimal shift. The large E_C offset between the p-type and n-type materials (~2.5 eV) serves as an effective charge carrier separation at zero-bias (Figure 6.1). The wide-bandgap of ZnO and CuSCN demonstrates the suitability of this heterostructure as a UV visible-blind photodetector. The schematic in Figure 6.1 illustrates the completed device structure represented in the energy band diagram.

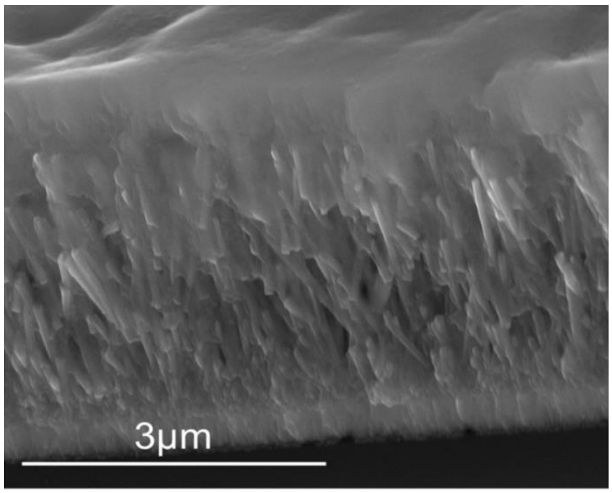

Figure 6.2 SEM micrograph cross-section of pH 6 ZnO-nanorods spray-coated with CuSCN.

The pH 6 nanorods are shown to be 2.5-3 μm long, with the CuSCN layer penetrating through the nanorod array and forming a bulk layer above the nanorods ~500 nm thick (Figure 6.2). The smooth, crack-free CuSCN morphology will assist in lowering the top-contact and series resistance of the device. By improving the pore-filling of the array, the compact CuSCN layer restricts atmospheric oxygen (and other gases) from directly adsorbing onto the ZnO nanorod surface, and simultaneously provides a high interfacial contact between ZnO and CuSCN. Consequently this increased surface area assists in maximising the region where recombination and charge-separation takes place.

6.1.2 Current-voltage measurements

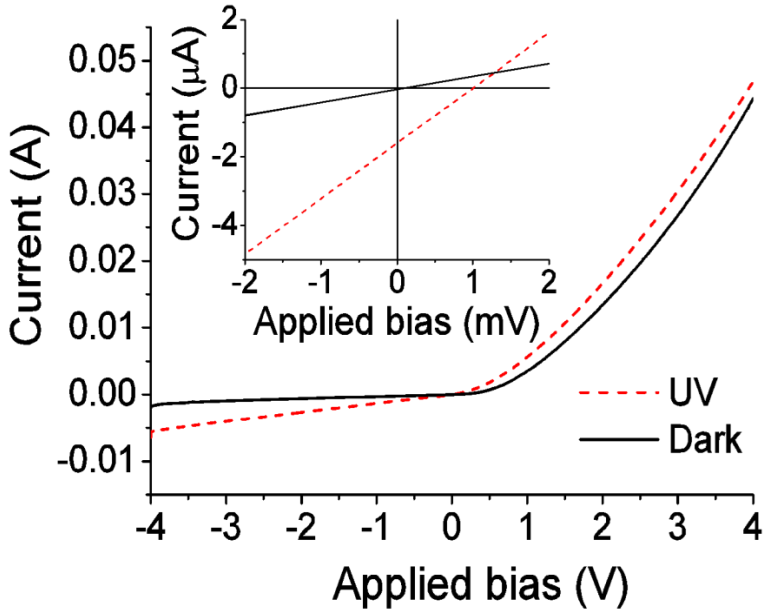

Figure 6.3 I-V plot of pH 6 ZnO-CuSCN device under dark and UV (3.5 mW cm^{-2}) illuminated conditions. Inset shows magnified area at the origin.

A typical *I–V* plot shows the rectifying behaviour of the device, see Figure 6.3. Two significant features were observed for this plot; firstly, the very low turn-on voltage of ~0 V, and secondly, the small, yet measurable, photovoltaic effect under UV illumination. The latter is attributed to the aforementioned well-aligned band structure of the device FTO, ZnO, CuSCN, and Au electron-affinities and Fermi levels are closely co-ordinated) (see Figure 6.1). This allows rapid charge-carrier separation at the interface, preventing photoexcited electrons in ZnO from recombining with holes at the p-n junction. The rectification ratio was measured as 23 at ± 4 V. The leakage current of 2 mA was attributed to the penetration of the CuSCN layer through the nanorod array contacting the FTO electrode creating shorts and reducing the shunt resistance of the device.

The inset of Figure 6.3 shows an enlarged area of the *I–V* origin curve and reveals the limited photovoltaic performance of the device. At an applied field of 0 V, the device would be truly self-powered and give a binary response that would be 0 A for no light, and a measurable current when under illumination. However, the serendipitous nature of the experimental arrangement allows the photocurrent to be measured under a small reverse and forward bias and will be discussed in the following section.

6.1.3 Photocurrent measurements

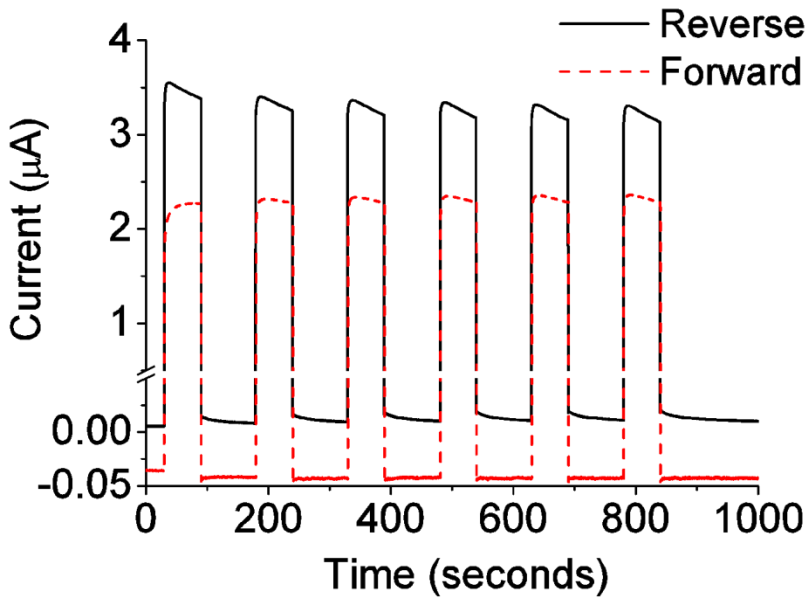

Figure 6.4 ZnO-CuSCN photocurrent stability for forward and reverse bias of 0.1 mV under UV LED irradiance of 3.5 mW cm^{-2} switched on (for 60 s) and off (for 90 s) for six repeat cycles.

Figure 6.4 shows the photocurrent response of the ZnO-CuSCN device at a nominal zero set bias. Six repeat cycles of switching the 3.5 mW cm^{-2} UV source on and off were used to test the repeatability of the device under a small forward and reverse bias of ~0.1 mV. In all cases, the photocurrent was observed to be consistent and repeatable. Interestingly, the photocurrent under forward bias was observed to alternate between negative and positive in relation to the UV source switching off and on. This provides an opportunity to use the device as an on-off binary-response for UV detection that exceeds previously recorded photosensitivity of ~10^5. The binary-response for the ZnO-CuSCN device arises from the photovoltaic behaviour and low turn-on voltage of the diode as the current changes from positive to negative upon illumination. An examination of Figure 6.4 shows that the expected

changes in photocurrent for forward and reverse bias are matched with the performance of the device shown in Figure 6.3 inset.

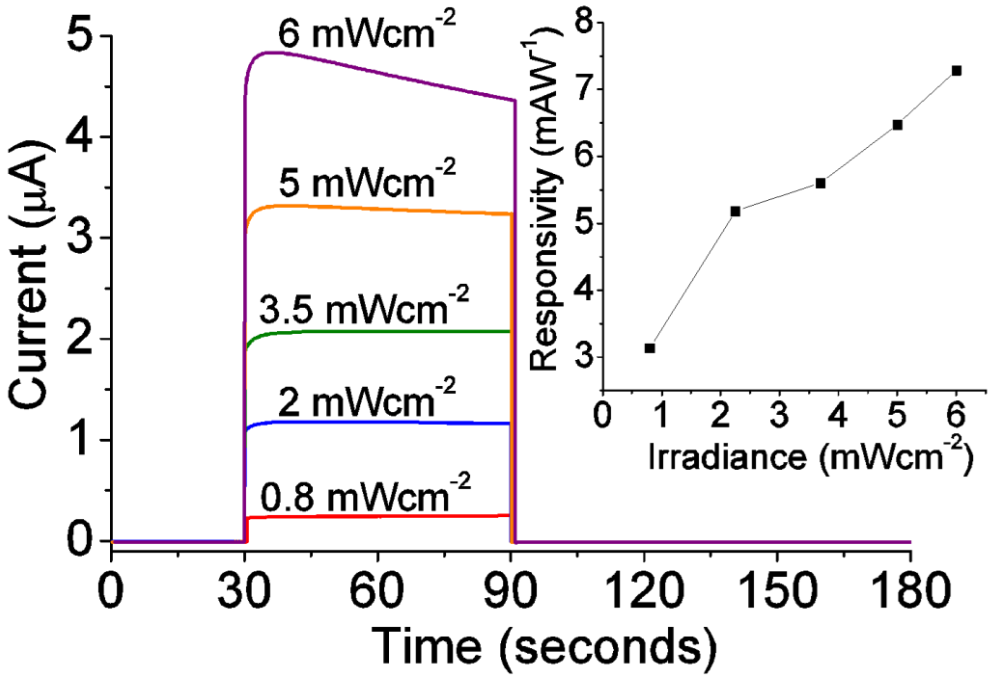

Figure 6.5 Current vs. time plot displaying the photoresponse to varying UV irradiances, inset shows the corresponding responsivity.

The photosensitivity of the ZnO-CuSCN device to 380 nm UV light was tested using a range of irradiances of 0.8–6 mW cm^{-2} (Figure 6.5). This shows a steadily increasing photocurrent response in relation to the irradiance intensity, achieving a photocurrent of 4.5 μA at 6 mW cm^{-2}. This value is the highest currently reported for this low-level of UV irradiance at a near zero-bias. While it was possible to extrapolate a true zero-bias response from these devices, it has not been done, as the exact shape of the *I-V* curve around 0 V is not accurately known. The enhanced photocurrent response is attributed to the nanorod array, which plays an essential role in maximizing the surface area for photon-absorption. Longer and/or thinner nanowires may improve the photocurrent further.

Two critical parameters are used to characterize photodetectors: the responsivity and the photoconductive gain (defined as the number of electrons produced in the external circuit for each absorbed incident photon). The responsivity (R_λ) and photoconductive gain (G) can be expressed as:

$$R_\lambda = \frac{\Delta I}{(A\ x\ P)} \text{ and } G = \left[\frac{\Delta I}{(A\ x\ P\ x\ \eta)}\right].\left(\frac{h\nu}{q}\right)$$

Herein, ΔI is the photocurrent difference between the dark and after 60 s of illumination, A is the electrode contact area (0.1 cm^2), P is the LED irradiance, e is the electron charge, h is Planck's constant, v is the frequency of the incident light, and η is effective photocarrier generation efficiency (assumed to be 0.7 in this work, taking the reflection, scattering, and incomplete absorption, etc. into consideration). The R_λ was shown to increase with illumination intensity up to 0.0075 A W^{-1} with a corresponding gain of ~0.04 for 6 mW cm^{-2} irradiance (inset of Figure 6.5).

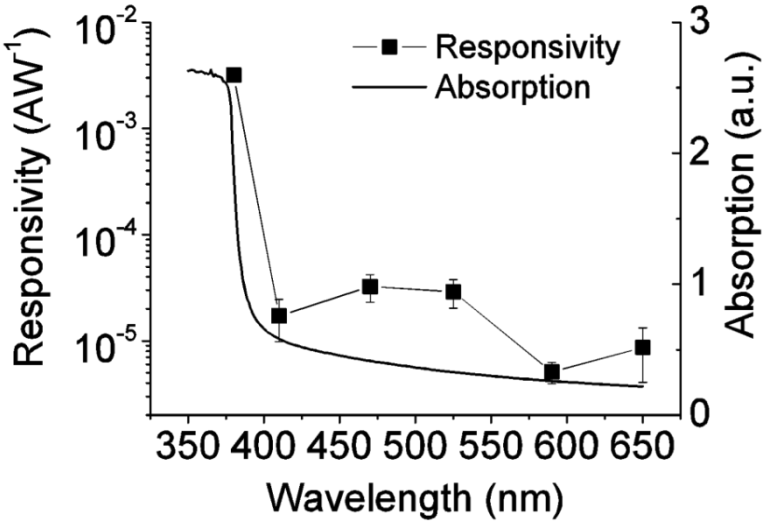

Figure 6.6 Spectral responsivity using 1 mW cm^{-2} irradiance and absorption spectra overlaid for the pH 6-ZnO-CuSCN device.

The UV selectivity of the ZnO-CuSCN device was tested at a nominal zero-bias and was shown to have a minimum UV to visible rejection ratio of ~100 (Figure 6.6). This is attributed to the wide bandgap of both the ZnO (3.3 eV) and the CuSCN (3.6 eV) semiconductors, which restricts the absorbed photons to a minimum energy of 3.3 eV in order to generate photoexcited carriers. This corresponds to the overlaid absorption spectra, which show the absorption edge of the ZnO-CuSCN heterostructure at ~380 nm (~3.3 eV).

It is possible that there is a contribution to the photodetector response from the CuSCN layer. However, this is unlikely to occur for two reasons. Firstly, the threshold for device turn-on is closely aligned with the ZnO band gap at 3.3 eV, and secondly, the CuSCN has a wider bandgap than ZnO and the light enters the device through the ZnO side; the absorption coefficient of ZnO at 3.6 eV is sufficient to absorb light of that energy as it passes through the ZnO before entering the CuSCN. The low-temperature aqueous solution used to synthesize the ZnO nanorods often incorporates unwanted defects in the crystal lattice. As

well as doping it as n-type, it can also introduce deep-level emission states that can reduce the UV–visible rejection ratio.

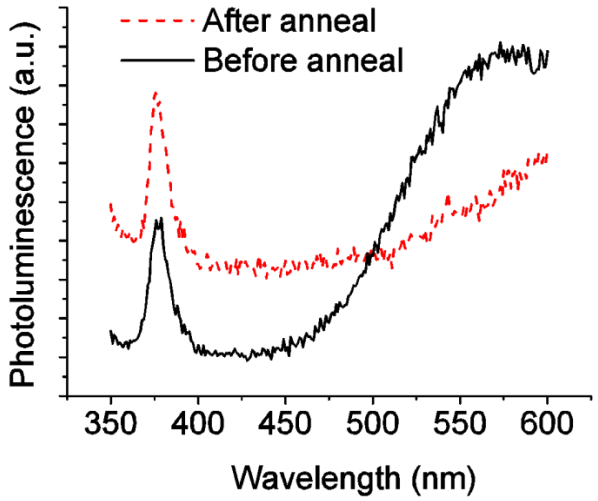

Figure 6.7 Photoluminescence spectra of pH 6 ZnO nanorods, before and after annealing in air.

The photoluminescence spectra of pH 6 ZnO nanorods before and after being annealed in air can be used to indicate the quality of crystal and the presence of defects. Figure 6.7 shows annealing at 400˚C for 1 h significantly reduced the defect-related emission peaking at 570 nm. However, the NBE peak at ~380 nm remains relatively broad and indicates an imperfect crystal lattice structure. This suggests the UV–visible rejection ratio could be increased by reducing the incorporation of deep-level defects in ZnO.

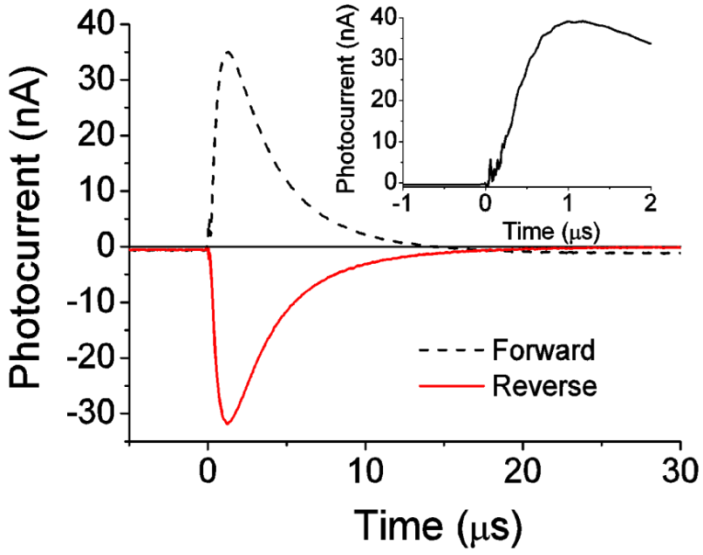

Figure 6.8 Fast transient photocurrent waveforms in response to a 355 nm, 5 ns pulse with an excitation energy of *I* = 0.3 μJ/pulse, with the enlarged rise response shown inset.

The photocurrent rise and decay time was measured with a 355 nm, 5 ns-pulse laser under forward and reverse bias. The rise time (τ_r) and the decay time (τ_d) were measured as ~500 ns and ~6.7 μs, respectively for both cases (see Figure 6.8). These values are at least 40 times faster than those previously reposted for self-powered photodetectors. In addition, the binary-response time in the forward-bias case (defined as the time for the photocurrent to switch from positive to negative) was measured as $\tau_r \sim 4$ ns and $\tau_d \sim 13$ μs. This rapid response time approaches the resolution of the oscilloscope and exceeds the response times for both Schottky and p-n-junction ZnO-based photodetectors.

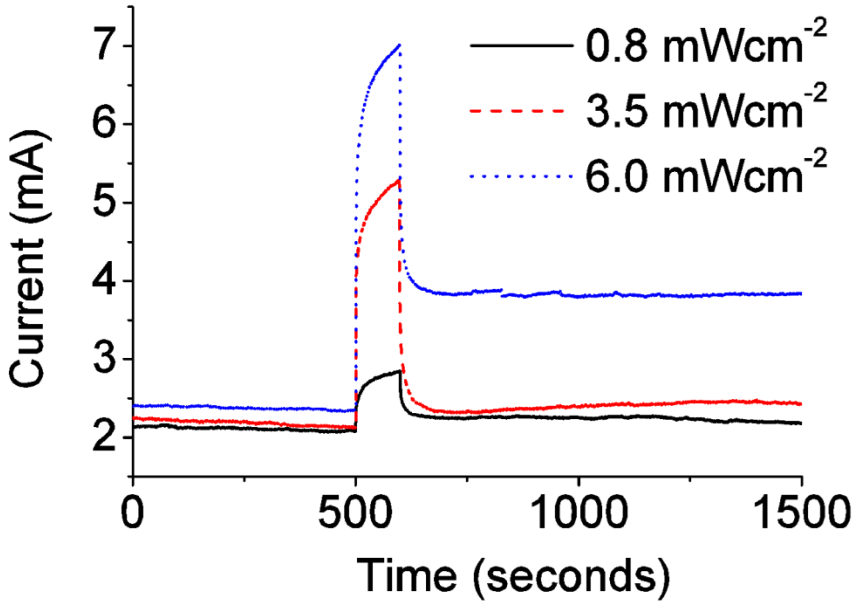

Figure 6.9 Photocurrent response of the ZnO-/CuSCN device under an applied field of -5 V for three UV (380 nm) irradiances.

To test the ZnO-CuSCN device in comparison with other ZnO p-n-photodetectors, it was tested under a −5 V applied bias for three UV irradiances (0.8, 3.5, and 6.0 mW cm^{-2}). Once again, it was shown that the photocurrent response correlates to increasing illumination intensity (Figure 6.9). A longer illumination period increases the quantity of accumulated photo-generated carriers and directly correlates to an increase in decay time of the device. From Figure 6.9, the responsivities (and gains) were calculated to be 9.5 (35), 8.4 (40), and 7.7 (47) A W^{-1} (greater than unity) for irradiances of 0.8, 3.5, and 6.0 mW cm^{-2}, respectively.

Finally, it should be noted that this ZnO-CuSCN device does not require ZnO-nanorod surfaces to be specially treated with absorbing polymers or encapsulated to prevent degradation. This device was exposed and tested in atmospheric conditions over a period of

six months and showed no sign of reduced performance. This represents a very significant paradigm shift in performance over previous devices of this type.

6.2 Self-powered pH 11 ZnO-nanorod/CuSCN photodetector

The detailed characterisation of pH 11 nanorods conducted in Chapter 4 showed the anneal atmospheres significantly influenced the ZnO properties. The effect on device performance was demonstrated by fabricating heterostructures from each of the pH 11 nanorods: as-grown, annealed in air, oxygen, and nitrogen. CuSCN was spray-deposited as with the previous self-powered photodetector.

6.2.1 Current-voltage measurements

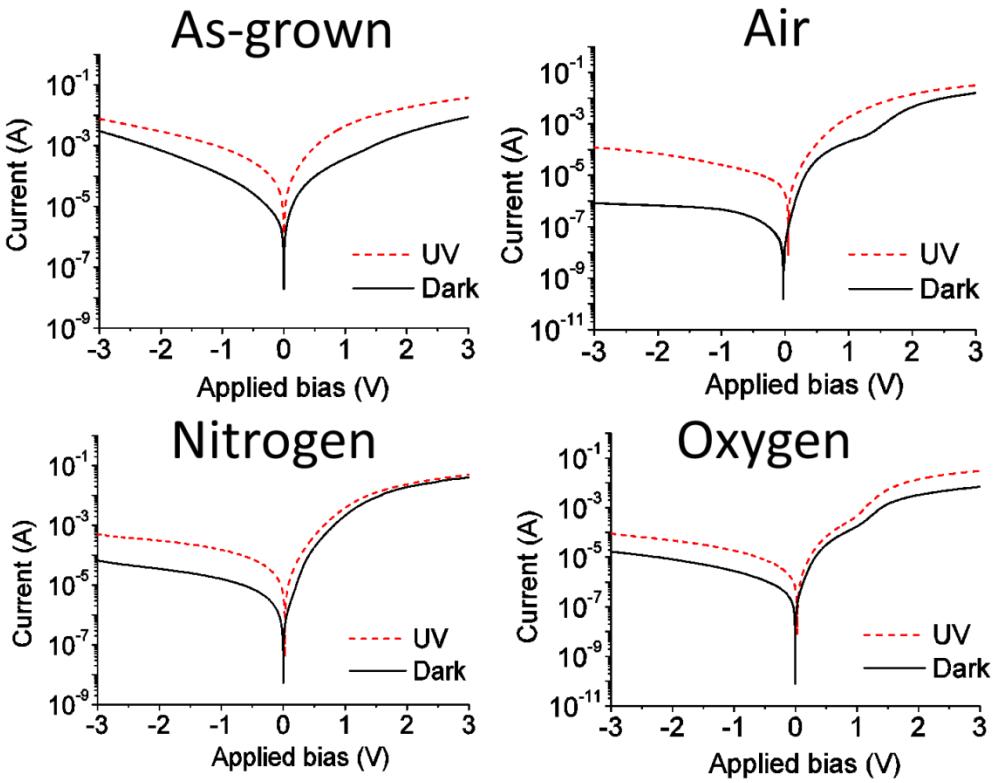

Figure 6.10 Semi-log current-voltage plots of ZnO nanorods as-grown, annealed in air, nitrogen or oxygen, and coated with CuSCN. Each plot shows the performance under dark and UV illuminated conditions.

The semi-log I-V plots for the ZnO-CuSCN p-n-heterostructure demonstrates photosensitivity was highest under the reverse-bias (Figure 6.10). This is because under

reverse-bias the only contribution to the dark current arises from minority carriers, whereas under forward-bias the main contribution comes from majority carriers. The rectifications obtained from Figure 6.10 are presented in Table 6-1.

Table 6-1 Rectification ratios extrapolated from the semi-log I-V plots in Figure 6.10.

ZnO sample	Reverse Current (±3V)		Forward current (±3V)		Rectification at ± 3V	
	Dark	UV	Dark	UV	Dark	UV
Air	0.8 μA	0.12 mA	17.2 mA	32.0 mA	21500	270
Nitrogen	67.6 μA	0.50 mA	40.5 mA	50.3 mA	600	100
Oxygen	16.4 μA	0.09 mA	7.0 mA	30.5 mA	440	340
As-grown	3.0 mA	7.52 mA	8.7 mA	37.0 mA	3	5

The maximum rectification of 21500 was obtained at ±3 V for air-annealed ZnO. This is ~100 times greater than previously reported ZnO-CuSCN diodes [182,190] and 35-50 times the rectification obtained for nitrogen/oxygen annealed ZnO. The lower rectifications for oxygen and nitrogen are linked to the higher larger leakage current in the device. This arises from multiple factors such as: diffusion current, space-charge generated current, band-to-band tunnelling current, and thermionic emission current. In this case, structural and point defects play a major role as trap states and recombination sites, which lead to recombination driven current in dark conditions and result in a higher leakage current. The presence of these defects has been clearly demonstrated using SEM, TEM, PL, and Raman spectroscopy (see section 4.5). The high quantity of trap states (V_{Zn}^{2-}) formed during the oxygen-anneal, and the thin-layer of amorphous material coating the nitrogen-annealed ZnO is the cause of high leakage current observed. Poor diode behaviour exhibited by the as-grown sample (Figure 6.10) suggests the nanorods are more intrinsic than n-type and is attributed to the regions of amorphous material consisting of trapped precursors throughout the lattice.

Nitrogen-annealed ZnO obtained the highest current under UV (50.3 mA) for the measured devices. This gives evidence to support the formation of shallow donors from unreacted precursors during the reducing atmosphere anneal (see section 2.1.3.2.2).

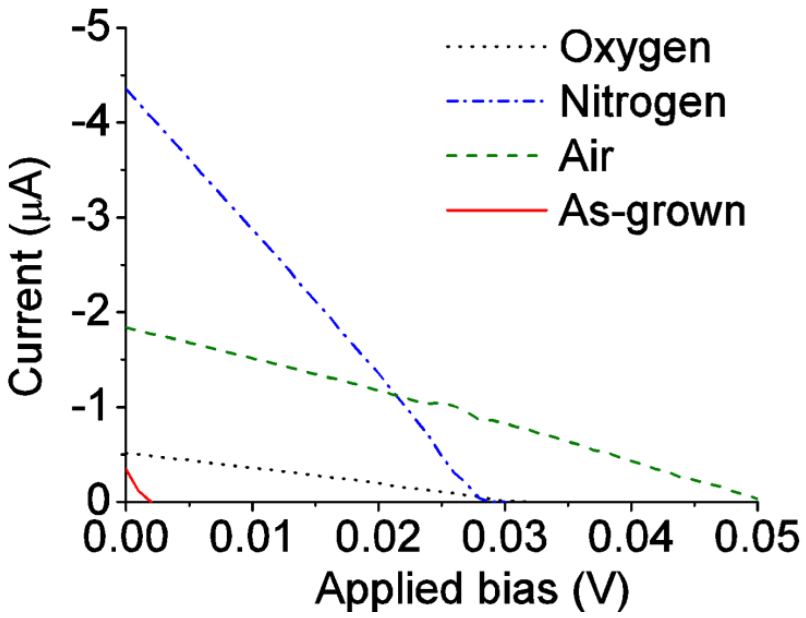

Figure 6.11 An enlarged current-voltage plot displaying the photovoltaic behaviour for each device under (380 nm 0.8 mW cm^{-2}) UV illumination.

Figure 6.11 proves the photovoltaic effect was exhibited by each of the ZnO-CuSCN diodes under UV illumination. It is shown that the air-annealed sample has the highest photovoltage and the nitrogen-annealed sample has the highest photocurrent. The photovoltage generated by the UV illumination is dependent on the in-built bias between the ZnO E_F and ϕ_{FTO} away from the junction. Nitrogen- and oxygen-annealed ZnO have a similar photovoltage, which indicates very similar E_F. Air-annealed ZnO has a higher photovoltage of 0.05 V, and suggests a larger difference between E_F that ϕ_{FTO}. This may be attributed to the fewer inconsistencies in the crytal lattice when compared to oxygen and nitrogen-annealed samples. The as-grown sample shows a very weak photovoltaic effect compared to the annealed samples. Figure 6.10 shows the as-grown sample exhibits a similar forward current to the annealed samples (37.0 mA), which signifies a similar carrier concentration. It therefore indicates rapid recombination is the cause, which is expected due to presence of amorphous material.

6.2.2 Photocurrent measurements

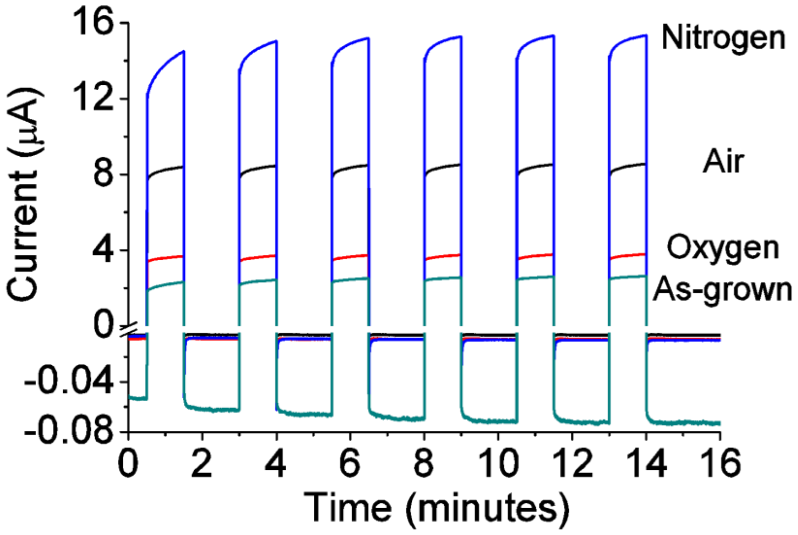

Figure 6.12 Photocurrent stability under (380 nm, 3.5 mW cm^{-2}) UV irradiance turned on (for 60 s) and off (for 90 s) six times.

Figure 6.12 demonstrates the reliability of the devices with consistent and stable photocurrent after switching the UV light on and off six times over a period of 15 minutes. Although the source meter was set to 0 V, a small dark current of -4 nA was detected indicating a small applied bias. When operating as a true self-powered photodetector there would be no voltage source so the dark current would be zero. Extrapolating the photocurrent to true zero-bias would actually increase the photocurrent by ~100%.

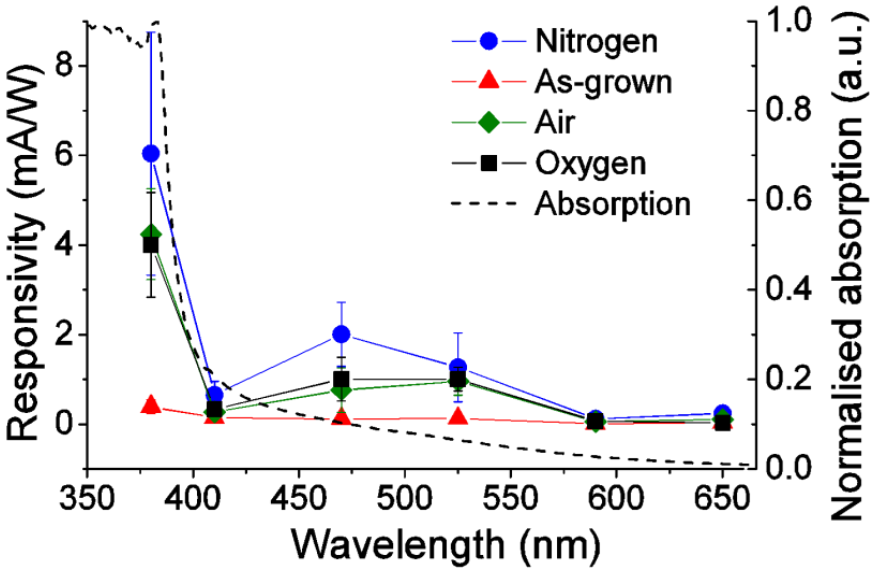

Figure 6.13 Spectral responsivity (for 0.8 mW cm^{-2} irradiance) and the corresponding absorption spectra of the device.

This photodetector is sensitive to specific ranges of UV 3.1-3.25 eV (380-400 nm) and blue-green 2.4 eV (475-525 nm) light. Using the expressions given previously:

$$R_\lambda = \frac{\Delta I}{(A\ x\ P)}\ ,$$

where ΔI is the difference between illuminated and dark current, A is the contact area (0.1 cm^2) and P is the LED irradiance. Device responsivity peaks in the UV-region (380 nm), corresponding closely to the absorption peak for the ZnO-CuSCN heterostructure (Figure 6.13). The weak responsivity peak around 475-525 nm (Figure 6.13) corresponds to the weak absorption slope in the UV-Vis spectra (Figure 4.17). For high intensity illuminations the trap states will become saturated and limit the promotion of carriers for visible wavelengths. This would reduce the responsivity to the visible spectra while maintaining a good UV response. The maximum responsivity was calculated to be 0.05 A W^{-1} for 380 nm, 6 mW cm^{-2} irradiance at near-zero bias.

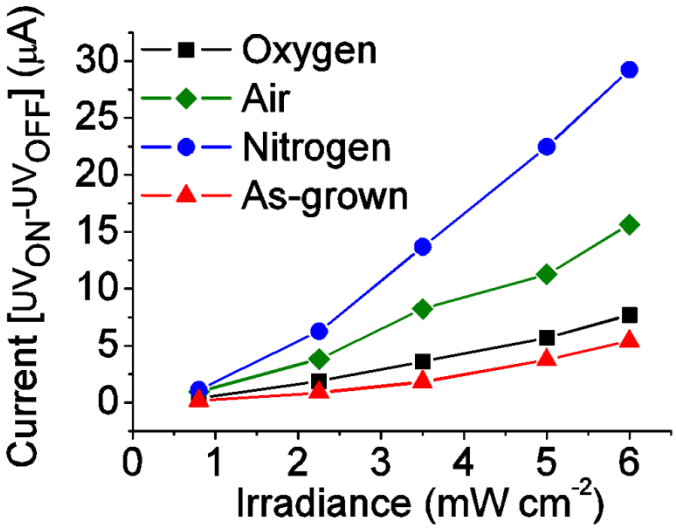

Figure 6.14 Photocurrent response for the ZnO-nanorod/CuSCN photodetector under increasing UV irradiances for near zero–bias (~0.1 mV).

The photocurrent response of all devices increased with UV irradiances from 0.8 to 6.0 mW cm^{-2} and showed no sign of saturation or reduction (Figure 6.14). This suggests the photocurrent would continue to increase for higher irradiances. The nitrogen-annealed sample exhibited the highest photocurrent of ~30 µA under 6 mW cm^{-2} UV irradiance. This is six times greater than the as-grown/oxygen-annealed ZnO devices reported here, and at least twice the highest currently reported by Deng et al, who tested using 8 W illumination [259].

6.2.3 Device mechanisms

As reviewed in section 2.1.4, defects have a significant impact on semiconductor behaviour, both optically and electrically. Surface defects however, influence the band-bending near the nanorod surface, for example in the case of photoconductivity (section 2.1.4.4). For pH 11 nanorods the synthesis and anneal process lead to the introduction of unintentional N-doping and other point defects (see section 2.1.3.2.2).

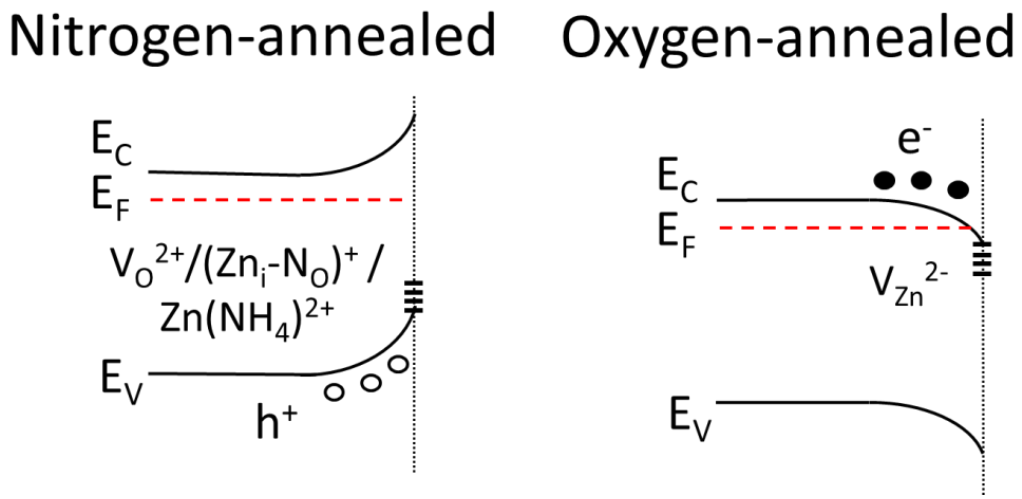

Figure 6.15 Schematics showing the band-bending at the ZnO interface for nitrogen- and oxygen-annealed nanorods.

Here, it is shown that band-bending differs for the nitrogen- and oxygen-annealed nanorods. The reducing atmosphere of the nitrogen anneal favours oxygen vacancies at the surface, or crystalline N-related defects, both of which are donor states and allow holes to accumulate at the nanorod surface resulting in upward band-bending (Figure 6.15). In the case of oxygen-annealed ZnO, it was concluded that the high oxygen partial pressure favoured zinc vacancies forming near the nanorod surface. These doubly-charged zinc vacancies (V_{Zn}^{2-}) act as electron trap states and lead to downward band-bending at the ZnO interface (Figure 6.15). When operating at near zero-bias, the band-bending at the electrode/p-n-junction interface is critical for charge carrier separation.

It is important to note that while the Keithley 2400 was used to measure the current by setting the source voltage equal to zero, the instrument always assumes that it is measuring a current from its internal source. In this case, a positive current will flow out of its terminals and a negative current will flow in to them (see Keithley 2400 manual ref. [280]). Hence, while the source meter it is set to zero, it is in fact applying a small negative-bias.

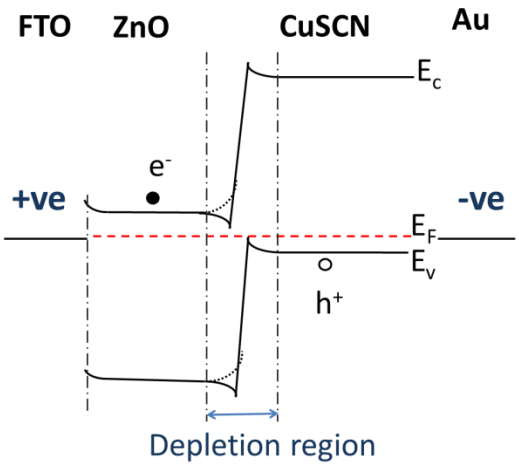

Figure 6.16 An energy band-diagram of the ZnO-CuSCN diode operating near zero-bias in dark conditions. Dotted-line (nitrogen) and solid-line (oxygen) at the interface represent the band-bending.

In the dark at zero-bias, the ZnO-CuSCN was in equilibrium with minimal current being generated (Figure 6.16).

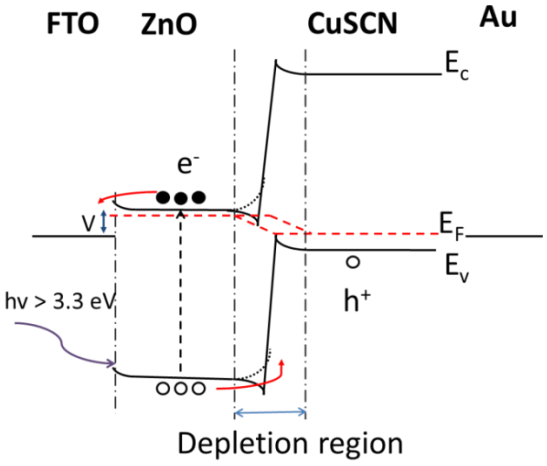

Figure 6.17 Energy band diagram under UV illuminated conditions for the ZnO-CuSCN device. Dotted-line (nitrogen) and solid-line (oxygen) at the interface represent the band-bending.

Upon UV illumination, electrons are photoexcited into the ZnO E_C, which raises the ZnO E_F above that of the ϕ_{FTO} (see Figure 6.17). As a result the mobile electrons experience a drift potential attracting them to the FTO electrode, where they recombine and generate the observed photocurrent. The concentration of photoexcited carriers determines the photocurrent intensity. The difference in photocurrent response between the samples can be explained by the thermally induced defects. In the oxygen-annealed samples, V_{Zn}^{2-} act as electron trap states at the nanorod surface, and it is at this ZnO-CuSCN interface that the

majority of carriers are photoexcited. When the electrons recombine with trap states, the carrier mobility is reduced and charge separation is hindered, thus reducing the photocurrent response. The high photocurrent measured for nitrogen-annealed ZnO, may be attributed to either, the N-related donor defects formed during the reducing nitrogen-anneal, or fewer V_{Zn}^{2-} trap states present. As the air-annealed sample lies between these two extremes it follows that it would have an intermediate response, which correlates with the DLE in Figure 4.20. The as-grown sample exhibits the lowest response of the fabricated devices due to the unreacted Zn-precursors trapped throughout the nanorod structure. These act as recombination sites that decrease both carrier mobility and concentration, and consequently have a negative effect on the device performance. However, the photocurrent of ~5 µA at 6 mW cm^{-2} irradiance is comparable to those self-powered devices fabricated at higher temperatures [252,254,255,281,282]. This demonstrates the potential for flexible devices using as-produced ZnO material synthesised at temperatures <100˚C.

6.2.4 Photovoltage response

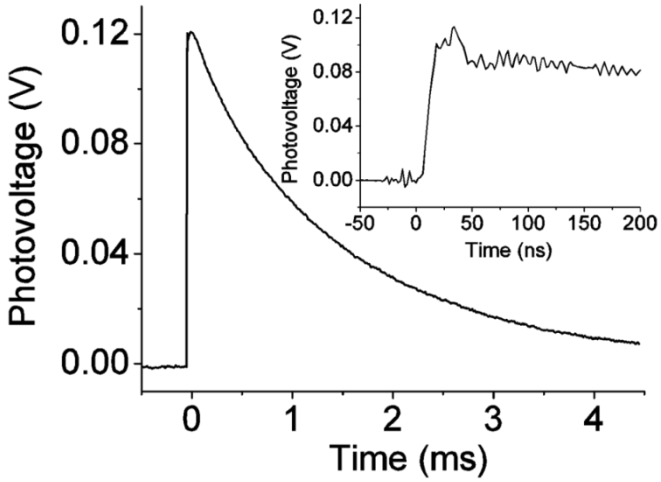

Figure 6.18 Fast transient photovoltage waveform in response to a 532 nm 5 ns-pulse with excitation energy of 0.1 mJ/pulse and enlarged rise time (inset).

Response times were tested using a 532 nm pulsed laser that excited electrons via the 2.4 eV trap states to the ZnO E_C. The device exhibited a rapid τ_r of ~25 ns (inset Figure 6.18) and τ_f of ~4 ms. The prolonged τ_f is linked to intermediary trap states that prevent direct band-to-band transition as shown by the diminished NBE and prominent DLE of the PL spectra (see Figure 4.20). Interestingly the ZnO-CuSCN photodetector showed almost no response to the 3.5 eV (355 nm) pulsed laser. A device fabricated using pH 6 synthesised ZnO-nanorods

shows a good photocurrent response to 355 nm pulse during the same experiment (Figure 6.8). The nanorods grown at pH 11 (14 μm) reported here are much longer than those grown at pH 6 (2-3 μm), and additionally have a dense, compact layer at the base (closest to the FTO) approximately 4 μm thick. The absorption coefficient of ZnO at 355 nm is very high as it is well above the main band-edge absorption onset at ~385 nm. Hence, when illuminated through the glass-FTO, as in the photo-response measurements, the majority of 355 nm photons will be absorbed close to the FTO. Due to the thick compact layer in the pH 11 grown rods this absorption occurs well away from the junction, whereas for the pH 6 grown rods, which lack this thick layer, photons are absorbed closer to the junction. Due to internal recombination, only carriers excited near the junction region contribute to the photocurrent in the photodetector. Therefore, 355 nm excitation does not create a significant photocurrent response in the pH 11 rods, whereas 532 nm laser and 380 nm illumination that penetrate much further through the ZnO, do.

6.3 Summary

Self-powered, inexpensive ZnO-nanorod based photodetectors were developed using pH 6 and pH 11 aqueous grown nanorods. The pH 6-ZnO based photodetector exhibited a rapid binary-response of ~4 ns and minimum decay time of 6.7 μs. Four photodetectors were fabricated using pH 11-nanorods that had been annealed in air, nitrogen, oxygen, and as-grown. The results showed that pH 11 photodetectors were sensitive in the UV and visible wavelengths with a maximum photocurrent response of 30μA (at 6 mW cm^{-2} irradiance) for nitrogen-annealed nanorods. The performance characteristics were assigned to the high interfacial area provided by the nanorod array, good pore-filling of the CuSCN hole-collecting material, and thermally induced donor defects.

The ZnO-CuSCN photodetectors have enhanced stability compared to others of a similar design without the requirement of a polymeric encapsulation layer; this is due to the impregnation of p-type CuSCN into the ZnO nanostructure. The behaviour of the device has been attributed to the pre-existing Fermi level alignment of the ZnO and CuSCN semiconductors, which results in a low turn-on of ~0 V and photovoltaic behaviour. These properties make the ZnO-CuSCN UV photodetector suitable for nanoscale applications that require rapid response times and self-sufficient functionality. Finally, these devices show that it is possible to produce a self-powered flexible photodetector using a simple and inexpensive fabrication process.

7 Conclusions and future work

7.1 Conclusions

7.1.1 Background and aims

This project consists of two major elements: firstly, the fabrication and characterisation of materials, and secondly, the design and development of UV photodetectors. The primary purpose of this project was to develop a low-temperature processing method that was facile and inexpensive, for the fabrication of optoelectronic devices. Reasons for choosing ZnO nanorods as the n-type material was discussed in Chapter 2. It highlighted the numerous production methods of ZnO nanostructures, good optical transparency to visible wavelengths due to its 3.34eV bandgap, and the chemical stability that is beneficial for longevity. In addition, the literature review emphasises the effect low-temperature processing has on ZnO properties, primarily focusing on the unavoidable structural and point defect incorporation during growth. Understanding which defects give rise to particular characteristics originates from the desire to manipulate material properties to our advantage. By enhancing or inhibiting particular defects it would be possible to influence the conductivity (n- or p-type), optical properties, and surface reactivity. Consequently, investigating the effect of processing (pH, precursor concentration, seed layer, temperature, duration, etc.) on these properties is critical to improving our understanding. Thermal annealing nullifies the benefit of low-temperature processing for flexible substrates, but it assists in the removal of unwanted defects from the crystal lattice. The identification of point defects in ZnO has long been a controversial subject, whether related to the unintentional n-type behaviour of ZnO or the optical luminescence typically emitted by deep-level emission defects. Currently it is impossible to directly pin-point the defects responsible for these side-effects. Although multiple characterisation techniques exist (PAS, PL, Raman, XPS, EXAFS), none provide the ability to single-out the defect responsible. Hence, it remains that multiple analysis techniques are used to infer possible defects and the selection is narrowed by theoretical calculations of the defect formation energies.

EXAFS obtained in optically-detected mode is a recently developed high-energy X-ray scattering technique that provides information relating to the crystal structure surrounding the

absorbing atom. In optically-detected mode, specific wavelengths are collected that relate to the luminescing regions in the crystal structure. Hence, site specific information surrounding the defects responsible for this emission can be deduced. As of yet, a high-quality EXAFS spectra in optically-detected mode has not be obtained, preventing a detailed analysis of the structure.

Selecting a p-type material for the fabrication of the device was not as simple as for the n-type. Firstly, there was no need for the p-type layer to be nanostructured, and secondly there was the option of using an inorganic or organic hole collector for the task. As interest in purely organic electronics grows (primarily for the benefit of device flexibility), it was deemed worth-while testing the differences in performance between the two options. Hence, a hybrid ZnO-PEDOT:PSS diode and an inorganic ZnO-CuSCN diode were fabricated. CuSCN was chosen for its good optical transparency, chemical stability, and reasonable conductivity (1.4 S/m). PEDOT:PSS has a similar hole conductivity to that of CuSCN, its HOMO is close to the E_V of CuSCN, and also has good optical transparency as a thin film. A side aspect of this project was the development of CuSCN deposition. It was demonstrated in Chapter 2 that previous methods (electrodeposition, SILAR, impregnation) were lacking in either pore-filling capability or suitable morphology. Hence, it was desirable to optimise the CuSCN coating method before analysing/comparing the device performance.

UV photodetectors are essential for a wide range of applications (chemical/biological analysis, optical communications, flame detection, etc.) and so research into its development is on-going. Recently the developmental focus for UV photodetectors is its size and portability. With a numerous possible structures for photodetectors (MSM, p-n-/p-i-n, FET, MIS, Schottky), it should be noted that almost all of these require an applied bias to achieve reasonable responsivity. Although photodetector may be on the nanoscale, the power needed to generate the large electric field required sizable components, which reduces the functionality of these nanoscale devices. Consequently, there has been interest in developing photodetectors that operate without an external bias, and so are deemed “self-powered”. The most common route to achieving this goal is the photovoltaic effect, and there is evidence that shows nanoscale fuel cells can be used to generate the required power [255].

In conclusion the aims of the project were set out as:

- Investigate the influence processing and thermal annealing has on the morphological, optical, and conductive properties on ZnO nanorods.

- Obtain EXAFS high-quality spectra of ZnO in optically-detected mode.
- Improve deposition of CuSCN p-type material.
- Compare purely-inorganic and hybrid (inorganic-organic) ZnO-based photodiodes using p-type CuSCN and PEDOT:PSS.
- Develop self-powered UV photodetectors and demonstrate the impact of processing on device performance.

7.1.2 Project progression

A number of experimental stages were needed to achieve the goals set in this project. These are outlined below and followed by a more detailed summary:

- Synthesise ZnO nanorods using an aqueous chemical solution and vary the growth conditions (pH, precursor concentration, duration, substrate etc.) to study the effects on ZnO properties.
- Characterise the ZnO nanorods using various techniques and interpret the data to demonstrate changes in the material's properties.
- Collect EXAFS of ZnO nanorods and interpret data to determine the quality of data. High-quality data could then be further analysed to distinguish between two regions with different PL emission.
- Test spin-coating and spray-coating of CuSCN onto ZnO nanorods. Demonstrate the difference in material properties comparing with the commonly-used impregnation technique.
- Fabricate photodiodes by spin-coating PEDOT:PSS or spray-coating CuSCN onto ZnO nanorods. Test the devices as photodiodes under UV illumination and monitor the effect of atmospheric conditions on device performance.
- Operate ZnO-CuSCN diodes at near-zero bias to confirm they function as self-powered UV photodetectors. Use pH 6 and pH 11 grown nanorods to demonstrate the effect materials processing can have on device performance.

ZnO nanorod growth and characterisation

The aqueous growth method was investigated using various precursor concentrations in attempt to control the morphology. As a result, ZnO nanorods were synthesised using an alkaline (pH 11) solution consisting of ammonia, HMT and zinc nitrate. These pH 11 nanorods demonstrated interesting material properties when thermally annealed in oxygen,

air, and nitrogen atmospheres; this warranted further investigation and so the project focus was shifted to accommodate this. A comparison was then made between these pH 11 grown nanorods and pH 6 ZnO nanorods grown using a solution consisting equimolar concentrations of HMT and zinc nitrate.

Detailed characterisation was required in order to determine the presence of defects and how they may affect the ZnO properties. The morphology was analysed using SEM, XRD provided the crystal structure and texture, PL and UV-Vis spectroscopy was conducted to ascertain the optical properties, and Hall Effect measurements obtained the conductivity. Raman spectroscopy probed the surface of the nanorods, whereas TEM analysis was able to penetrate the bulk and display varying contrasts across the nanorod length.

EXAFS analysis at the Diamond Light Source synchrotron was performed on ZnO nanorods that exhibited high-intensity optical luminescence. The spectrum was obtained in both transmission and optically-detected modes for two wavelength emissions (500 nm and 660 nm). Differences between the two wavelengths indicate this technique can successfully distinguish between two emission regions in the lattice. Data analysis provided estimations of the atomic bond lengths, the number of nearest neighbouring atoms, and the lattice disorder.

P-type deposition and device fabrication

Two of ways to improve the CuSCN deposition were explored: spin-coating while using a heat lamp to evaporate the solvent, and depositing a mist onto a heated sample using a pneumatic spray gun. As the spray-deposition showed the most promise, it was further developed using various CuSCN solution concentrations, droplet-sizes, drying intervals, and number of layers. To demonstrate the effectiveness the spray-deposition, it was directly compared with the most commonly used impregnation technique.

To fabricate a hybrid device, PEDOT:PSS was spin-coated onto ZnO nanorods. The polymer was found to suspend on the nanorod tips and attempts were made to improve the pore-filling. The PEDOT:PSS was diluted 1:5 and 1:10 vol.% in acetone. However, this led to the PSS coating the PEDOT being removed and an increase in PEDOT grain size. Hence, this only served to have the opposite effect – decreasing the nanorod penetration. Consequently, undiluted PEDOT:PSS was used for further experimentation.

Edges and sides of FTO-substrate that are not used for the based electrode were coated with an insulating layer of PMMA to prevent short-circuits from occurring. The device was completed when an Au top-electrode was a sputtered onto the p-type material and PMMA. It was found that by depositing the Au on PMMA it provides a good contact site for the measuring cables to be attached without damaging the active area of the device.

The photocurrent response to a UV LED over time was compared for both hybrid (ZnO-PEDOT:PSS) and purely-inorganic (ZnO-CuSCN) photodiodes. The differences in p-type morphology and device stability under long testing periods of illumination are demonstrated. The purely inorganic devices exhibited the better performance both in terms of response time and photocurrent intensity and so were selected to be investigated further.

UV photodetectors

The ZnO-CuSCN devices were shown to exhibit a photovoltaic effect that may be used to generate a photocurrent response at zero-bias, thus functioning as a self-powered photodetector. To investigate the effect of processing on the device performance the photodetectors were fabricated from pH 6 and pH 11 nanorods. The responsivity, spectral sensitivity, stability, and response times were all closely examined. Significant differences between the photodetectors were observed which highlighted the important role defects play in the device performance.

7.1.3 Completion of objectives

The extent to which the objectives of the project set out in section 7.1.1 were met is discussed below.

Effect of processing on material properties

ZnO nanorods synthesised using a pH 11 solution was confirmed to be nitrogen-doped during the synthesis process using Raman spectroscopy. The nanorod morphology, crystallography, and optical properties were shown to be sensitive to the thermal anneal atmosphere used. This was assigned to Zn-precursors trapped in the lattice and on the surface during growth that either decompose or form new ZnO depending on the anneal conditions. Post-annealing the pH 11 nanorods exhibited a green luminescence under UV excitation. Compiling data form multiple analysis techniques and first principle calculations attributed the emission was attributed to zinc vacancies. As a comparison and to prove the aqueous chemical growth can

be performed correctly, pH 6 grown nanorods were used. This equimolar (pH 6) method is commonly used and extensively analysed, and so provides a suitable basis for comparison.

EXAFS analysis

The deep-level emission of the (pH 11) ZnO nanorods provided a unique opportunity to test an unproven technique using EXAFS analysis. The successful capture of high-quality EXAFS data in optically-detected mode meant it was possible to analysis the crystal structure for two regions relating to 500 nm and 660 nm emission. Differences in peak-width and position signified the technique can be used to successfully distinguish between different structures. It was established that 660 nm emission originates from the nanorod surface, the 500 nm emission was related to disorder on Zn-sites.

Improved CuSCN deposition

The ZnO-CuSCN diode fabricated using spray-deposited CuSCN had a rectification of 3550 at ±3 V. This is up to ten times greater than those previously reported with a similar structure and 290% better when compared to the similar device fabricated using the CuSCN impregnation method. A 6 µm-thick CuSCN film exhibited a conductivity of 0.02 $S.m^{-1}$ and the highest reported hole mobility of 70 $cm^2/V.s$. By removing the long drying stages used in impregnation and the typical storage time required post-processing, the spray-coat method has reduced the processing time and made it possible to rapidly fabricate effective devices.

Hybrid/Inorganic photodetector comparison

The hybrid and purely-inorganic photodiodes were directly compared. Both PEDOT and CuSCN show good absorption in the UV and when combined with n-type ZnO, allowing them to function as a UV photodiodes. The difference in performance was linked to both the device structure and nanorod properties. The hybrid photodiode exhibited photocurrent response in the range of 50-600 nA at 0 V, and the recovery times were dependent on the measurement conditions sometimes requiring a day in dark conditions before it neared its equilibrium state. The ZnO-CuSCN photodiode exhibited a higher photocurrent (0.4-1.3 µA) as a result of the increased interfacial contact at the p-n junction. The recovery time of the ZnO-CuSCN diode was measured to be <0.1 ms, which is 10^5 times faster than that of the hybrid device.

Self-powered Photodetectors

Self-powered photodetectors fabricated using the ZnO-CuSCN heterostructure were shown to exhibit a rapid binary-response of ~4 ns and decay time of 6.7 µs for pH 6 nanorods. The photocurrent response reached ~5 µA for 6 mW cm^{-2} UV irradiance and demonstrated a minimum UV to visible rejection ratio of ~100.

Four photodetectors were fabricated using pH 11 grown nanorods: as-grown ZnO, and post-annealing in air, nitrogen, and oxygen. The results showed that pH 11 photodetectors were sensitive in the UV and visible wavelengths with a maximum photocurrent response of 30µA (at 6 mW cm^{-2} irradiance) for nitrogen-annealed nanorods. The rise time was measured as ~25 ns with a decay time of ~4 ms.

The performance characteristics of both pH 6 and pH 11 were assigned to the high interfacial area provided by the nanorod array, good pore-filling of the CuSCN hole-collecting material. In the case of the nitrogen-annealed ZnO, the improved performance was linked to thermally induced donor defects. The self-powered characteristic of the device has been attributed to ZnO photoconductivity, pre-existing Fermi level alignment of the ZnO and CuSCN semiconductors that results in a low turn-on of ~0 V, and the photovoltaic behaviour. These properties make the ZnO-CuSCN UV photodetector suitable for nanoscale applications that require rapid response times and self-sufficient functionality.

7.2 Future work

This section provides suggestions of possible future work that could be undertaken in order to improve upon the results obtained in this thesis, or add new information to support the work already presented.

Defect analysis

Questions remain regarding the green luminescence observed post-annealing pH 11 nanorods in various atmospheres. Although the analysis presented in this thesis strongly indicates zinc vacancies were responsible, other possibilities such as copper substituted on Zn sites (Cu_{Zn}) remain. It would therefore be beneficial if further analysis was conducted to confirm the emission source. For example, annealing the samples in a hydrogen atmosphere saturate the doubly charge zinc vacancy (V_{Zn}^{2-}) which would serve to quench the green emission. PAS could be used to identify the concentration of V_{Zn}^{2-} present in each of the annealed ZnO

samples, in order to support the prediction that addition zinc vacancies were formed during the high oxygen partial pressure anneal.

It would be of interest to investigate the effect of anneal duration on the ZnO properties. In addition, by varying the anneal temperature it may be possible to determine at what temperature the green emission initiates and also when it begins to decrease, thereby providing further information regarding the stability of the defect responsible for the green emission. The colouration of the ZnO samples also warrants further investigation, whether annealing in hydrogen or zinc vapour returns the yellow, pink, or brown sample to its original cream colour may help to identify the defects responsible.

The data obtained for the EXAFS analysis was extensive and only a small portion was analysed to demonstrate the technique was successful. By performing detailed analysis of the X-ray Absorption Near Edge Structure (XANES) it would be possible to take into account the all the scattering pathways rather than the single-scatter analysed using EXAFS. This would provide a more detailed and accurate level of analysis for the crystal structure.

Improved device structure

The ZnO morphology was shown to play a significant role in the device performance, both in terms of increased interfacial contact and optical transmission. It would be of interest to determine the optimal length and diameter for the diffusion of charge carriers in the pH 11 nanorods to the junction interface. This would reduce recombination in the nanorod bulk and consequently lead to an increase in photocurrent response. The photocurrent could also be improved by using nanotubes in place of nanorods, which would increase the interfacial contact at the junction.

The CuSCN layer could be improved by using a modified CuSCN solution as reported in ref. [179], which has proven to exhibit increased hole concentration and conductivity. The increased hole concentration with improved hole mobility demonstrated by the spray-deposition may result in a superior CuSCN film that has higher conductivity than previously reported. This could be used to fabricate the ZnO-CuSCN heterostructure and would serve to improve the carrier separation at the junction interface.

The ZnO-PEDOT:PSS photodiode did not perform to the same stand as the inorganic photodiode, and it was mainly attributed to the exposed ZnO nanorods. It would therefore be of interest to demonstrate how the device performed if it was encapsulated minimised thereby

minimising surface reactions below the PEDOT layer. The same test could be conducted on an encapsulated ZnO-CuSCN photodiode. This would demonstrate whether the ambient atmosphere had a significant impact on device performance.

As-grown pH 11 ZnO nanorods were reported to exhibit a photoresponse on the same scale as previously reported devices that required high-temperature annealing. Consequently, this makes it a suitable option for flexible substrates. However, this was not proved in this thesis and it would be of significant interest to demonstrate this possibility.

References

[1] S. Das, S. Ghosh, *Dalton transactions* **2013**, *42*, 1645–56.

[2] K. L. Chopra, S. Major, D. K. Pandya, *Thin Solid Films* **1983**, *102*, 1–46.

[3] D. Banerjee, J. Y. Lao, D. Z. Wang, J. Y. Huang, Z. F. Ren, D. Steeves, B. Kimball, M. Sennett, *Applied Physics Letters* **2003**, *83*, 2061.

[4] M. H. Huang, S. Mao, H. Feick, H. Yan, Y. Wu, H. Kind, E. Weber, R. Russo, P. Yang, *Science* **2001**, *292*, 1897–1899.

[5] K. Govender, D. S. Boyle, P. O'Brien, D. Binks, D. West, D. Coleman, *Advanced Materials* **2002**, *14*, 1221.

[6] S. Liang, H. Sheng, Y. Liu, Z. Huo, Y. Lu, H. Shen, *Journal of Crystal Growth* **2001**, *225*, 110–113.

[7] E. Monroy, F. Omnes, F. Calle, *Semiconductor Science and Technology* **2003**, *18*, R33–R51.

[8] C. Soci, A. Zhang, B. Xiang, S. A. Dayeh, D. P. R. Aplin, J. Park, X. Y. Bao, Y. H. Lo, D. Wang, *Nano Letters* **2007**, *7*, 1003–1009.

[9] H. Kind, H. Yan, B. Messer, M. Law, P. Yang, *Advanced Materials* **2002**, *14*, 158–160.

[10] S. T. Tan, J. L. Zhao, S. Iwan, X. W. Sun, X. H. Tang, J. D. Ye, M. Bosman, L. J. Tang, G. Q. Lo, K. L. Teo, *IEEETransactions on Electron Devices* **2010**, *57*, 129–133.

[11] J. S. Park, B. R. Lee, J. M. Lee, J. S. Kim, S. O. Kim, M. H. Song, *Applied Physics Letters* **2010**, *96*.

[12] S. F. Chichibu, T. Ohmori, N. Shibata, T. Koyama, T. Onuma, *Journal of Physics and Chemistry of Solids* **2005**, *66*, 1868–1871.

[13] Y. W. Heo, L. C. Tien, D. P. Norton, B. S. Kang, F. R. Gila, P. B, S. J. Pearton, *Applied Physics Letters* **2004**, *85*, 2002–2004.

[14] T. Miyata, T. Minami, *Smart Structures and Materials 1999: Smart Materials Technologies* **1999**, *3675*, 150–158 348.

[15] J. X. Wang, X. W. Sun, Y. Yang, H. Huang, Y. C. Lee, O. K. Tan, L. Vayssieres, *Nanotechnology* **2006**, *17*, 4995–4998.

[16] T. Gao, T. H. Wang, *Applied Physics a-Materials Science & Processing* **2005**, *80*, 1451–1454.

[17] Q. Wan, Q. H. Li, Y. J. Chen, T. H. Wang, X. L. He, J. P. Li, C. L. Lin, *Applied Physics Letters* **2004**, *84*, 3654.

[18] M. H. Huang, Y. Y. Wu, H. Feick, N. Tran, E. Weber, P. D. Yang, *Advanced Materials* **2001**, *13*, 113–116.

[19] R. S. Wagner, W. C. Ellis, *Applied Physics Letters* **1964**, *4*, 89.

[20] J. Jie, G. Wang, Y. Chen, X. Han, Q. Wang, B. Xu, J. G. Hou, *Applied Physics Letters* **2005**, *86*, 1–3.

[21] R. Hauschild, H. Lange, H. Priller, C. Klingshirn, R. Kling, A. Waag, H. J. Fan, M. Zacharias, H. Kalt, *Physica Status Solidi B-Basic Solid State Physics* **2006**, *243*, 853–857.

[22] A. S. B. A. C. Mofor A. Elshaer, D. Fuhrmann, F. Bertram, A. Hangleiter, J. Christen, A. Waag, *physica status solidi (c)* **2006**, *3*, 1046–1050.

[23] P. Yang, H. Yan, S. Mao, R. Russo, J. Johnson, R. Saykally, N. Morris, J. Pham, R. He, H.-J. Choi, *Advanced Functional Materials* **2002**, *12*, 323.

[24] C. J. Summers, Z. L. Wang, *Nano Letters* **2004**, *4*, 423–426.

[25] J. Song, X. Wang, E. Riedo, Z. L. Wang, *The journal of physical chemistry. B* **2005**, *109*, 9869–72.

[26] N. S. Ramgir, D. J. Late, A. B. Bhise, M. A. More, I. S. Mulla, D. S. Joag, K. Vijayamohanan, *The journal of physical chemistry. B* **2006**, *110*, 18236–42.

[27] W. I. Park, D. H. Kim, S. W. Jung, G. C. Yi, *Applied Physics Letters* **2002**, *80*, 4232–4234.

[28] W. Lee, M.-C. Jeong, J.-M. Myoung, *Nanotechnology* **2004**, *15*, 254–259.

[29] J.-J. Wu, S.-C. Liu, *Advanced Materials* **2002**, *14*, 215–218.

[30] W. I. Park, G. C. Yi, M. Y. Kim, S. J. Pennycook, *Advanced Materials* **2002**, *14*, 1841–1843.

[31] F. Weiss, M. Audier, A. Bartasyte, D. Bellet, C. Girardot, C. Jimenez, J. Kreisel, S. Pignard, M. Salaun, C. Ternon, *Pure and Applied Chemistry* **2009**, *81*, 1523–1534.

[32] M. Kawakami, A. B. Hartanto, Y. Nakata, T. Okada, *Japanese Journal of Applied Physics Part 2-Letters* **2003**, *42*, L33–L35.

[33] T. Okada, K. Kawashima, M. Ueda, *Applied Physics a-Materials Science & Processing* **2005**, *81*, 907–910.

[34] B. D. Yao, Y. F. Chan, N. Wang, *Applied Physics Letters* **2002**, *81*, 757.

[35] J. Zhang, Y. Yang, B. Xu, F. Jiang, J. Li, *Journal of Crystal Growth* **2005**, *280*, 509–515.

[36] Z. W. Pan, S. M. Mahurin, S. Dai, D. H. Lowndes, *Nano letters* **2005**, *5*, 723–7.

[37] J. Cembrero, A. Elmanouni, B. Hartiti, M. Mollar, B. Mari, *Thin Solid Films* **2004**, *451-52*, 198–202.

[38] B. Marí, M. Mollar, A. Mechkour, B. Hartiti, M. Perales, J. Cembrero, *Microelectronics Journal* **2004**, *35*, 79–82.

[39] R. Konenkamp, K. Boedecker, M. C. Lux-Steiner, M. Poschenrieder, F. Zenia, C. Levy-Clement, S. Wagner, *Applied Physics Letters* **2000**, *77*, 2575–2577.

[40] T. Pauporte, D. Lincot, *Applied Physics Letters* **1999**, *75*, 3817–3819.

[41] R. Marotti, *Solar Energy Materials and Solar Cells* **2004**, *82*, 85–103.

[42] M. H. Wong, A. Berenov, X. Qi, M. J. Kappers, Z. H. Barber, B. Illy, Z. Lockman, M. P. Ryan, J. L. MacManus-Driscoll, *Nanotechnology* **2003**, *14*, 968–973.

[43] M. A. Vergés, C. J. Serna, *J. Chem. Soc., Faraday Trans.* **1990**, *86*, 959–963.

[44] L. Vayssieres, K. Keis, S. E. Lindquist, A. Hagfeldt, *Journal of Physical Chemistry B* **2001**, *105*, 3350–3352.

[45] L. W. Ji, S. M. Peng, J. S. Wu, W. S. Shih, C. Z. Wu, I. T. Tang, *Journal of Physics and Chemistry of Solids* **2009**, *70*, 1359–1362.

[46] P. K. Giri, S. Dhara, R. Chakraborty, *Materials Chemistry and Physics* **2010**, *122*, 18–22.

[47] Q. Li, V. Kumar, Y. Li, H. Zhang, T. J. Marks, R. P. H. Chang, *Chemistry of Materials* **2005**, *17*, 1001–1006.

[48] A. Sugunan, H. C. Warad, M. Boman, J. Dutta, *Journal of Sol-Gel Science and Technology* **2006**, *39*, 49–56.

[49] D. S. Boyle, K. Govender, P. O'Brien, *Chemical Communications* **2002**, *1*, 80–81.

[50] L. E. Greene, B. D. Yuhas, M. Law, D. Zitoun, P. Yang, *Inorganic Chemistry* **2006**, *45*, 7535–7543.

[51] M. N. R. Ashfold, R. P. Doherty, N. G. Ndifor-Angwafor, D. J. Riley, Y. Sun, *Thin Solid Films* **2007**, *515*, 8679–8683.

[52] K. M. McPeak, T. P. Le, N. G. Britton, Z. S. Nickolov, Y. A. Elabd, J. B. Baxter, *Langmuir : the ACS journal of surfaces and colloids* **2011**, *27*, 3672–7.

[53] J. G. Strom, H. W. Jun, *Journal of Pharmaceutical Sciences* **1980**, *69*, 1261–1263.

[54] Y. Tak, K. Yong, *The Journal of Physical Chemistry B* **2005**, *109*, 19263–19269.

[55] J. Zhang, *Chemistry of Materials* **2002**, *14*, 4172–4177.

[56] J. P. Liu, X. T. Huang, Y. Y. Li, Q. Zhong, L. Ren, *Materials Letters* **2006**, *60*, 1354–1359.

[57] K. Govender, D. S. Boyle, P. B. Kenway, P. O'Brien, *Journal of Materials Chemistry* **2004**, *14*, 2575–2591.

[58] H. Zhang, D. Yang, X. Y. Ma, Y. J. Ji, J. Xu, D. L. Que, *Nanotechnology* **2004**, *15*, 622–626.

[59] Y. P. Sheng, Y. Jiang, X. Z. Lan, C. Wang, S. Y. Li, X. M. Liu, H. H. Zhong, *Journal of Nanomaterials* **2011**, *2011*, 12.

[60] L. E. Greene, M. Law, D. H. Tan, M. Montano, J. Goldberger, G. Somorjai, P. D. Yang, *Nano Letters* **2005**, *5*, 1231–1236.

[61] M. Law, L. E. Greene, J. C. Johnson, R. Saykally, P. Yang, *Nature Materials* **2005**, *4*, 455–459.

[62] L. E. Greene, M. Law, J. Goldberger, F. K. Johnson, C. Justin, Y. Zhang, R. J. Saykally, P. Yang, *Angewandte Chemie International Edition* **2003**, *42*, 3031–3034.

[63] D. Li, Y. H. Leung, A. B. Djurisic, Z. T. Liu, M. H. Xie, S. L. Shi, S. J. Xu, W. K. Chan, *Applied Physics Letters* **2004**, *85*, 1601–1603.

[64] R. Gedye, F. Smith, K. Westaway, H. Ali, L. Baldisera, L. Laberge, J. Rousell, *Tetrahedron Letters* **1986**, *27*, 279–282.

[65] M.-G. Ma, Y.-J. Zhu, G.-F. Cheng, Y.-H. Huang, *Materials Letters* **2008**, *62*, 507–510.

[66] C. Min, X. Shen, W. Sheng, *Applied Physics A* **2009**, *96*, 799–803.

[67] S. M. Mahpeykar, J. Koohsorkhi, H. Ghafoori-Fard, *Nanotechnology* **2012**, *23*, 165602.

[68] A. Janotti, C. G. Van de Walle, *Physical Review B* **2007**, *76*, 045501.

[69] A. Pöppl, G. Völkel, *physica status solidi (a)* **1990**, *121*, 195–204.

[70] K. Vanheusden, C. H. Seager, W. L. Warren, D. R. Tallant, J. A. Voigt, *Applied Physics Letters* **1996**, *68*, 403–405.

[71] L. E. Halliburton, N. C. Giles, N. Y. Garces, M. Luo, C. C. Xu, L. H. Bai, L. A. Boatner, *Applied Physics Letters* **2005**, *87*, 172108.

[72] N. Ohashi, T. Nakata, T. Sekiguchi, H. Hosono, M. Mizuguchi, T. Tsurumi, J. Tanaka, H. Haneda, *Japanese Journal of Applied Physics* **1999**, *38*, L113–L115.

[73] L. J. Brillson, H. L. Mosbacker, M. J. Hetzer, Y. Strzhemechny, G. H. Jessen, D. C. Look, G. Cantwell, J. Zhang, J. J. Song, *Applied Physics Letters* **2007**, *90*.

[74] J. C. Simpson, J. F. Cordaro, *Journal of Applied Physics* **1988**, *63*, 1781.

[75] J. C. Simpson, J. F. Cordaro, *Journal of Applied Physics* **1990**, *67*, 6760.

[76] R. A. Winston, J. F. Cordaro, *Journal of Applied Physics* **1990**, *68*, 6495.

[77] J. Zhong, *Journal of The Electrochemical Society* **1993**, *140*, 3644.

[78] R. de la Cruz, R. Pareja, R. González, L. Boatner, Y. Chen, *Physical Review B* **1992**, *45*, 6581–6586.

[79] T. K. Gupta, W. D. Straub, M. S. Ramanachalam, J. P. Schaffer, A. Rohatgi, *Journal of Applied Physics* **1989**, *66*, 6132.

[80] F. A. Selim, M. H. Weber, D. Solodovnikov, K. G. Lynn, *Physical Review Letters* **2007**, *99*, DOI 10.1103/PhysRevLett.99.085502.

[81] S. Lany, A. Zunger, *Physical Review Letters* **2007**, *98*, 045501.

[82] A. Kohan, G. Ceder, D. Morgan, C. Van de Walle, *Physical Review B* **2000**, *61*, 15019–15027.

[83] P. Erhart, A. Klein, K. Albe, *Physical Review B* **2005**, *72*, 085213.

[84] F. Oba, S. R. Nishitani, S. Isotani, H. Adachi, I. Tanaka, *Journal of Applied Physics* **2001**, *90*, 824.

[85] T. Paudel, W. Lambrecht, *Physical Review B* **2008**, *77*, 205202.

[86] S. Zhang, S.-H. Wei, A. Zunger, *Physical Review B* **2001**, *63*, 075205.

[87] A. Janotti, C. G. Van de Walle, *Applied Physics Letters* **2005**, *87*, 122102.

[88] A. Janotti, C. G. Van de Walle, *Reports on Progress in Physics* **2009**, *72*, 126501.

[89] E. Mollwo, *NUCLEAR PHYSICS A HADRONS AND NUCLEI* **1954**, *138*, 478–488.

[90] D. G. Thomas, J. J. Lander, *The Journal of Chemical Physics* **1956**, *25*, 1136.

[91] C. G. Van de Walle, *Physical Review Letters* **2000**, *85*, 1012–1015.

[92] C. G. Van de Walle, J. Neugebauer, *Nature* **2003**, *423*, 626–628.

[93] A. Janotti, C. G. Van de Walle, *Nature Materials* **2007**, *6*, 44–47.

[94] F. A. Kröger, *The Chemistry of Imperfect Crystals*, North-Holland, Amsterdam, **1974**.

[95] G. A. Shi, M. Stavola, S. J. Pearton, M. Thieme, E. V Lavrov, J. Weber, *Physical Review B* **2005**, *72*, 8.

[96] S. J. Jokela, M. D. McCluskey, *Physical Review B* **2005**, *72*, 113201.

[97] A. Janotti, C. G. Van de Walle, *Nature materials* **2007**, *6*, 44–7.

[98] Y. B. Zhang, G. K. L. Goh, K. F. Ooi, S. Tripathy, *Journal of Applied Physics* **2010**, *108*, 083716.

[99] G. A. Shi, M. Stavola, S. J. Pearton, M. Thieme, E. V Lavrov, J. Weber, *Physical Review B* **2005**, *72*, 8.

[100] B. K. Meyer, H. Alves, D. M. Hofmann, W. Kriegseis, D. Forster, F. Bertram, J. Christen, A. Hoffmann, M. Strassburg, M. Dworzak, U. Haboeck, A. V Rodina, *Physica Status Solidi B-Basic Research* **2004**, *241*, 231–260.

[101] Y. M. Strzhemechny, H. L. Mosbacker, D. C. Look, D. C. Reynolds, C. W. Litton, N. Y. Garces, N. C. Giles, L. E. Halliburton, S. Niki, L. J. Brillson, *Applied Physics Letters* **2004**, *84*, 2545–2547.

[103] L. Wang, B. Lin, L. Zhou, Y. X. Shang, G. N. Panin, D. Fu, *Materials Letters* **2012**, *85*, 171–174.

[104] L. Liu, J. Xu, D. Wang, M. Jiang, S. Wang, B. Li, Z. Zhang, D. Zhao, C.-X. Shan, B. Yao, D. Shen, *Physical Review Letters* **2012**, *108*, 215501.

[105] K. Iwata, P. Fons, A. Yamada, K. Matsubara, S. Niki, *Journal of Crystal Growth* **2000**, *209*, 526–531.

[106] C. C. Lin, S. Y. Chen, S. Y. Cheng, H. Y. Lee, *Applied Physics Letters* **2004**, *84*, 5040–5042.

[107] S. J. Jiao, Z. Z. Zhang, Y. M. Lu, D. Z. Shen, B. Yao, J. Y. Zhang, B. H. Li, D. X. Zhao, X. W. Fan, Z. K. Tang, *Applied Physics Letters* **2006**, *88*, 031911.

[108] D. C. Look, *Semiconductor Science and Technology* **2005**, *20*, S55–S61.

[109] C. Y. Zhang, X. M. Li, X. D. Gao, J. L. Zhao, K. S. Wan, J. M. Bian, *Chemical Physics Letters* **2006**, *420*, 448–452.

[110] J.-L. Zhao, X.-M. Li, J.-M. Bian, W.-D. Yu, C.-Y. Zhang, *Journal of Crystal Growth* **2005**, *280*, 495–501.

[111] N. Y. Garces, N. C. Giles, L. E. Halliburton, G. Cantwell, D. B. Eason, D. C. Reynolds, D. C. Look, *Applied Physics Letters* **2002**, *80*, 1334–1336.

[112] M. A. Myers, M. T. Myers, M. J. General, J. H. Lee, L. Shao, H. Wang, *Applied Physics Letters* **2012**, *101*, 112101.

[113] X. M. Dai, S. J. Xu, C. C. Ling, G. Brauer, W. Anwand, W. Skorupa, *Journal of Applied Physics* **2012**, *112*, 046102.

[114] P. Li, S. Deng, G. Liu, K. Hou, *Chemical Physics Letters* **2012**, *543*, 92–95.

[115] J. L. Lyons, A. Janotti, C. G. Van de Walle, *Applied Physics Letters* **2009**, *95*, 252105.

[116] E. C. Lee, Y. S. Kim, Y. G. Jin, K. J. Chang, *Physical Review B* **2001**, *64*, 085120.

[117] A. Kaschner, U. Haboeck, M. Strassburg, G. Kaczmarczyk, A. Hoffmann, C. Thomsen, A. Zeuner, H. R. Alves, D. M. Hofmann, B. K. Meyer, *Applied Physics Letters* **2002**, *80*, 1909–1911.

[118] A. B. Djurišić, A. M. C. Ng, X. Y. Chen, *Progress in Quantum Electronics* **2010**, *34*, 191–259.

[119] B. X. Lin, Z. X. Fu, Y. B. Jia, *Applied Physics Letters* **2001**, *79*, 943–945.

[120] P. S. Xu, Y. M. Sun, C. S. Shi, F. Q. Xu, H. B. Pan, *Nuclear Instruments and Methods in Physics Research Section B: Beam Interactions with Materials and Atoms* **2003**, *199*, 286–290.

[121] J. Hu, B. C. Pan, *The Journal of chemical physics* **2008**, *129*, 154706.

[122] E. T. N.H. Nickel, *Zinc Oxide—A Material for Micro- and Optoelectronic Applications*, Springer, Dodrecht, The Netherlands, **2005**.

[123] S. A. . Lima, F. . Sigoli, M. Jafelicci Jr, M. . Davolos, *International Journal of Inorganic Materials* **2001**, *3*, 749–754.

[124] F. Oba, A. Togo, I. Tanaka, J. Paier, G. Kresse, *Physical Review B* **2008**, *77*, 245202.

[125] Y. Sun, H. Wang, *Physica B: Condensed Matter* **2003**, *325*, 157–163.

[126] P. Erhart, K. Albe, A. Klein, *Physical Review B* **2006**, *73*, 205203.

[127] J. Kramer, *Journal of Applied Physics* **1976**, *47*, 1719.

[128] C. Ton-That, L. Weston, M. Phillips, *Physical Review B* **2012**, *86*, 115205.

[129] K. H. Tam, C. K. Cheung, Y. H. Leung, A. B. Djurisic, C. C. Ling, C. D. Beling, S. Fung, W. M. Kwok, W. K. Chan, D. L. Phillips, L. Ding, W. K. Ge, *Journal of Physical Chemistry B* **2006**, *110*, 20865–20871.

[130] N. Y. Garces, L. Wang, L. Bai, N. C. Giles, L. E. Halliburton, G. Cantwell, *Applied Physics Letters* **2002**, *81*, 622–624.

[131] R. Kuhnert, R. Helbig, *Journal of Luminescence* **1981**, *26*, 203–206.

[132] L. E. Halliburton, N. Y. Garces, L. Wang, L. Bai, N. C. Giles, G. Cantwell, *Applied Physics Letters* **2002**, *81*, 622–624.

[133] R. Dingle, *Physical Review Letters* **1969**, *23*, 579–581.

[134] R. E. Dietz, H. Kamimura, M. D. Sturge, A. Yariv, *Physical Review* **1963**, *132*, 1559–1569.

[135] J. Iqbal, B. Q. Wang, X. F. Liu, D. P. Yu, B. He, R. H. Yu, *New Journal of Physics* **2009**, *11*, 063009.

[136] T. M. Borseth, B. G. Svensson, A. Y. Kuznetsov, P. Klason, Q. X. Zhao, M. Willander, *Applied Physics Letters* **2006**, *89*, 262112.

[137] H. Morkoç, Ü. Özgür, *Zinc Oxide: Fundamentals, Materials and Device Technology*, **2009**.

[138] H. Q. Wang, G. Z. Wang, L. C. Jia, C. J. Tang, G. H. Li, *Journal of Physics D-Applied Physics* **2007**, *40*, 6549–6553.

[139] S. A. Studenikin, N. Golego, M. Cocivera, *Journal of Applied Physics* **1998**, *84*, 2287–2294.

[140] L. E. Greene, M. Law, J. Goldberger, F. Kim, J. C. Johnson, Y. F. Zhang, R. J. Saykally, P. D. Yang, *Angewandte Chemie-International Edition* **2003**, *42*, 3031–3034.

[141] M. Li, G. Xing, L. F. N. A. Qune, G. Xing, T. Wu, C. H. A. Huan, X. Zhang, T. C. Sum, *Physical chemistry chemical physics : PCCP* **2012**, *14*, 3075–82.

[142] D. C. Reynolds, D. C. Look, B. Jogai, H. Morkoç, *Solid State Communications* **1997**, *101*, 643–646.

[143] D. C. Reynolds, D. C. Look, B. Jogai, J. E. Van Nostrand, R. Jones, J. Jenny, *Solid State Communications* **1998**, *106*, 701–704.

[144] Q. X. Zhao, P. Klason, M. Willander, H. M. Zhong, W. Lu, J. H. Yang, *Applied Physics Letters* **2005**, *87*, 211912.

[145] Z. Q. Chen, S. Yamamoto, M. Maekawa, A. Kawasuso, X. L. Yuan, T. Sekiguchi, *Journal of Applied Physics* **2003**, *94*, 4807–4812.

[146] K. Knutsen, A. Galeckas, A. Zubiaga, F. Tuomisto, G. Farlow, B. Svensson, A. Kuznetsov, *Physical Review B* **2012**, *86*, 121203.

[147] Y.-J. Lin, C.-L. Tsai, Y.-M. Lu, C.-J. Liu, *Journal of Applied Physics* **2006**, *99*, 093501.

[148] X. L. Wu, G. G. Siu, C. L. Fu, H. C. Ong, *Applied Physics Letters* **2001**, *78*, 2285–2287.

[149] M. Wang, E. W. Shin, J. S. Chung, S. H. Hur, E. J. Kim, S. H. Hahn, K. K. Koo, *Journal of Materials Science* **2010**, *45*, 4111–4114.

[150] H. Zhou, H. Alves, D. M. Hofmann, W. Kriegseis, B. K. Meyer, G. Kaczmarczyk, A. Hoffmann, *Applied Physics Letters* **2002**, *80*, 210–212.

[151] U. Ozgur, Y. I. Alivov, C. Liu, A. Teke, M. A. Reshchikov, S. Dogan, V. Avrutin, S. J. Cho, H. Morkoc, *Journal of Applied Physics* **2005**, *98*, 041301.

[152] M. H. Weber, N. S. Parmar, K. A. Jones, K. G. Lynn, *Journal of Electronic Materials* **2010**, *39*, 573–576.

[153] K. Grasza, E. Lusakowska, P. Skupinski, K. Kopalko, J. Bak-Misiuk, A. Mycielski, *Physica Status Solidi B-Basic Solid State Physics* **2007**, *244*, 1468–1472.

[154] H. H. Kung, *Transition Metal Oxides: Surface Chemistry and Catalysis*, Elsevier, Amsterdam, Oxford, New York, Tokyo, **1989**.

[155] Q. H. Li, T. Gao, Y. G. Wang, T. H. Wang, *Applied Physics Letters* **2005**, *86*, 123117.

[156] L. Soderholm, G. K. Liu, M. R. Antonio, F. W. Lytle, *The Journal of Chemical Physics* **1998**, *109*, 6745.

[157] N. H. Tran, A. J. Hartmann, R. N. Lamb, *Journal of Physical Chemistry B* **1999**, *103*, 4264–4268.

[158] S. Gautam, S. Kumar, P. Thakur, K. H. Chae, B. H. Koo, C. G. Lee, *Journal of Physics D: Applied Physics* **2009**, *42*, 175406.

[159] W. Mu, L. L. Kerr, N. Leyarovska, *Chemical Physics Letters* **2009**, *469*, 318–320.

[160] L. Armelao, F. Heigl, A. Jurgensen, R. I. R. Blyth, T. Regier, X.-T. Zhou, T. K. Sham, *Journal of Physical Chemistry C* **2007**, *111*, 10194–10200.

[161] L. S. Kau, K. O. Hodgson, E. I. Solomon, *Journal of the American Chemical Society* **1989**, *111*, 7103–7109.

[162] R. A. Rosenberg, G. K. Shenoy, L. C. Tien, D. Norton, S. Pearton, X. H. Sun, T. K. Sham, *Applied Physics Letters* **2006**, *89*, 093118.

[163] S. Larcheri, C. Armellini, F. Rocca, A. Kuzmin, R. Kalendarev, G. Dalba, R. Graziola, J. Purans, D. Pailharey, F. Jandard, *Superlattices and Microstructures* **2006**, *39*, 267–274.

[164] A. Array, H. Kawazoe, M. Yasukawa, H. Hyodo, M. Kurita, H. Yanagi, *Nature* **1997**, *389*, 939 – 942.

[165] L. Cattin, B. A. Reguig, A. Khelil, M. Morsli, K. Benchouk, J. C. Bernède, *Applied Surface Science* **2008**, *254*, 5814–5821.

[166] M. Cavas, R. K. Gupta, A. A. Al-Ghamdi, O. A. Al-Hartomy, F. El-Tantawy, F. Yakuphanoglu, *Journal of Sol-Gel Science and Technology* **2012**, *64*, 219–223.

[167] A. Konno, T. Kitagawa, H. Kida, G. R. Asoka Kumara, K. Tennakone, *Current Applied Physics* **2005**, *5*, 149–151.

[168] V. P. S. Perera, K. Tennakone, *Solar Energy Materials and Solar Cells* **2003**, *79*, 249–255.

[169] K. Tennakone, G. Kumara, A. Kumarasinghe, K. W. Sirimanne, P, *Semiconductor Science and Technology* **1995**, *10*, 1689–1693.

[170] A. Konno, E. V. A. Premalal, G. R. R. A. Kumara, R. M. G. Rajapakse, M. Shimomura, K. Murakami, *Chemical Communications* **2010**, *46*, 3360–3362.

[171] R. Tena-Zaera, A. Katty, S. Bastide, C. Levy-Clement, B. O'Regan, V. Munoz-Sanjose, *Thin Solid Films* **2005**, *483*, 372–377.

[172] B. O'Regan, F. Lenzmann, R. Muis, J. Wienke, *Chemistry of Materials* **2002**, *14*, 5023–5029.

[173] V. P. S. Perera, M. K. I. Senevirathna, P. K. D. D. P. Pitigala, K. Tennakone, *Solar Energy Materials and Solar Cells* **2005**, *86*, 443–450.

[174] J. E. Jaffe, T. C. Kaspar, T. C. Droubay, T. Varga, M. E. Bowden, G. J. Exarhos, *Journal of Physical Chemistry C* **2010**, *114*, 9111–9117.

[175] D. L. Smith, V. I. Saunders, *Acta Crystallographica Section B-Structural Science* **1982**, *38*, 907–909.

[176] D. L. Smith, V. I. Saunders, *Acta Crystallographica Section B-Structural Science* **1981**, *37*, 1807–1812.

[177] M. Kabesova, M. Dunajjurco, M. Serator, J. Gazo, J. Garaj, *Inorganica Chimica Acta* **1976**, *17*, 161–165.

[178] K. Tennakone, A. H. Jayatissa, C. A. N. Fernando, S. Wickramanayake, S. Punchihewa, L. K. Weerasena, W. D. R. Premasiri, *Physica Status Solidi (a)* **1987**, *103*, 491–497.

[179] E. V. . Premalal, N. Dematage, G. R. R. A. Kumara, R. M. G. Rajapakse, M. Shimomura, K. Murakami, A. Konno, *Journal of Power Sources* **2012**, *203*, 288–296.

[180] W. Wu, S. Cui, C. Yang, G. Hu, H. Wu, *Electrochemistry Communications* **2009**, *11*, 1736–1739.

[181] Y. Ni, Z. Jin, K. Yu, Y. Fu, T. Liu, T. Wang, *Electrochimica Acta* **2008**, *53*, 6048–6054.

[182] Q. B. Zhang, H. H. Guo, Z. F. Feng, L. L. Lin, J. Z. Zhou, Z. H. Lin, *Electrochimica Acta* **2010**, *55*, 4889–4894.

[183] W. B. Wu, Z. G. Jin, G. D. Hu, S. J. Bu, *Electrochimica Acta* **2007**, *52*, 4804–4808.

[184] T. Dittrich, D. Kieven, M. Rusu, A. Belaidi, J. Tornow, K. Schwarzburg, M. Lux-Steiner, *Applied Physics Letters* **2008**, *93*, 053113.

[185] G. R. R. A. Kumara, A. Konno, G. K. R. Senadeera, P. V. V Jayaweera, D. B. R. A. De Silva, K. Tennakone, *Solar Energy Materials and Solar Cells* **2001**, *69*, 195–199.

[186] C. Lévy-Clément, R. Tena-Zaera, M. A. Ryan, A. Katty, G. Hodes, *Advanced Materials* **2005**, *17*, 1512–1515.

[187] A. Belaidi, T. Dittrich, D. Kieven, J. Tornow, K. Schwarzburg, M. Kunst, N. Allsop, M. C. Lux-Steiner, S. Gavrilov, *Solar Energy Materials and Solar Cells* **2009**, *93*, 1033–1036.

[188] X.-D. Gao, X.-M. Li, W.-D. Yu, J.-J. Qiu, X.-Y. Gan, *Thin Solid Films* **2008**, *517*, 554–559.

[189] B. R. Sankapal, E. Goncalves, A. Ennaoui, M. C. Lux-Steiner, *Thin Solid Films* **2004**, *451--452*, 128–132.

[190] W. B. Wu, S. G. Cui, C. H. Yang, G. D. Hu, H. T. Wu, *Electrochemistry Communications* **2009**, *11*, 1736–1739.

[191] B. Postels, A. Kasprzak, T. Buergel, A. Bakin, E. Schlenker, H. H. Wehmann, A. Waag, *Journal of the Korean Physical Society* **2008**, *53*, 115–118.

[192] Y. Selk, M. Minnermann, T. Oekermann, M. Wark, J. Caro, *Journal of Applied Electrochemistry* **2011**, *41*, 445–452.

[193] U. V Desai, C. K. Xu, J. M. Wu, D. Gao, *Nanotechnology* **2012**, *23*, 205401.

[194] B. C. O'Regan, F. Lenzmann, *The Journal of Physical Chemistry B* **2004**, *108*, 4342–4350.

[195] A. J. Breeze, Z. Schlesinger, S. A. Carter, H. Tillmann, H.-H. Hörhold, *Solar Energy Materials and Solar Cells* **2004**, *83*, 263–271.

[196] T. Kietzke, H.-H. Hörhold, D. Neher, *Chemistry of Materials* **2005**, *17*, 6532–6537.

[197] C.-C. Cheng, Y.-L. Chu, P.-H. Huang, Y.-C. Yen, C.-W. Chu, A. C.-M. Yang, F.-H. Ko, J.-K. Chen, F.-C. Chang, *Journal of Materials Chemistry* **2012**, *22*, 18127.

[198] S. Kirchmeyer, K. Reuter, *Journal of Materials Chemistry* **2005**, *15*, 2077–2088.

[199] S. Y. Shao, F. M. Liu, Z. Y. Xie, L. X. Wang, *Journal of Physical Chemistry C* **2010**, *114*, 9161–9166.

[200] N. Sakai, G. K. Prasad, Y. Ebina, K. Takada, T. Sasaki, *Chemistry of Materials* **2006**, *18*, 3596–3598.

[201] Y. Q. Qi, P. Chen, T. J. Wang, X. J. Hu, S. Y. Zhou, *Macromolecular Rapid Communications* **2006**, *27*, 356–360.

[202] A. G. Bayer, *European Patent 440 957*, **1991**.

[203] A. Gevaert, *European Patent 564 911*, **1993**.

[204] F. Jonas, W. Krafft, B. Muys, *Macromolecular Symposia* **1995**, *100*, 169–173.

[205] G. Heywang, F. Jonas, *Advanced Materials* **1992**, *4*, 116–118.

[206] S. Möller, C. Perlov, W. Jackson, C. Taussig, S. R. Forrest, *Nature* **2003**, *426*, 166–9.

[207] S. H. Kim, S. H. Park, K. Il Lee, S. M. Kim, J. W. Cho, *35th Ieee Photovoltaic Specialists Conference* **2010**, - 3760.

[208] Z.-H. Feng, et al., *Chinese Physics B* **2010**, *19*, 38601.

[209] I. Mora-Seró, J. Bisquert, F. Fabregat-Santiago, G. Garcia-Belmonte, G. Zoppi, K. Durose, Y. Proskuryakov, I. Oja, A. Belaidi, T. Dittrich, R. Tena-Zaera, A. Katty, C. Lévy-Clément, V. Barrioz, S. J. C. Irvine, *Nano Letters* **2006**, *6*, 640–650.

[210] C. S. Rout, C. N. R. Rao, *Nanotechnology* **2008**, *19*, 285203.

[211] J. Liu, Y. H. Ahn, J. Y. Park, K. H. Koh, S. Lee, *Nanotechnology* **2009**, *20*, 445203.

[212] A. Zainelabdin, S. Zaman, G. Amin, O. Nur, M. Willander, *Nanoscale Research Letters* **2010**, *5*, 1442–1448.

[213] A. El-Shaer, A. Dev, J. P. Richters, S. R. Waldvogel, J. Waltermann, W. Schade, T. Voss, *Physica Status Solidi B-Basic Solid State Physics* **2010**, *247*, 1564–1567.

[214] J. Wang, F. Gao, N. C. Greenham, *Applied Physics Letters* **2010**, *97*, 053301.

[215] J. Briscoe, M. Stewart, M. Vopson, M. Cain, P. M. Weaver, S. Dunn, *Advanced Energy Materials* **2012**, *2*, 1261–1268.

[216] J. Briscoe, E. Bilotti, S. Dunn, *Applied Physics Letters* **2012**, *101*, 093902.

[217] E. Park, O. seok Kwon, S. joo Park, J. seop Lee, S. You, J. Jang, *Journal of Materials Chemistry* **2012**, *22*, 1521.

[218] R. D. Ladhe, K. V. Gurav, S. M. Pawar, J. H. Kim, B. R. Sankapal, *Journal of Alloys and Compounds* **2012**, *515*, 80–85.

[219] C. M. Hangarter, S. C. Hernandez, X. He, N. Chartuprayoon, Y. H. Choa, N. V Myung, *The Analyst* **2011**, *136*, 2350–8.

[220] L. Canfield, J. Kerner, R. Korde, *Journal of the Optical Society of America. B, Optical physics* **1989**, *28*, 3940 – 3943.

[221] H. Morkoc, S. Strite, G. Gao, M. Lin, B. Sverdlov, *Journal of applied physics* **1994**, *76*, 1363 – 1398.

[222] M. Caria, L. Barberini, S. Cadeddu, A. Giannattasio, A. Lai, A. Rusani, A. Sesselego, *Nuclear Instruments and Methods in Physics Research Section A: Accelerators, Spectrometers, Detectors and Associated Equipment* **2001**, *466*, 115–118.

[223] M. Iwami, *Nuclear Instruments and Methods in Physics Research Section A: Accelerators, Spectrometers, Detectors and Associated Equipment* **2001**, *466*, 406–411.

[224] J.-F. Hochedez, J. Alvarez, F. D. Auret, P. Bergonzo, M.-C. Castex, A. Deneuville, J. M. Defise, B. Fleck, P. Gibart, S. A. Goodman, O. Hainaut, J.-P. Kleider, P. Lemaire, J. Manca, E. Monroy, E. Muñoz, P. Muret, M. Nesladek, F. Omnes, E. Pace, J. L. Pau, V. Ralchenko, J. Roggen, U. Schühle, C. Van Hoof, *Diamond and Related Materials* **2002**, *11*, 427–432.

[225] J. Hiscock, A. T. Collins, *Diamond and Related Materials* **1999**, *8*, 1753–1758.

[226] S. Salvatori, F. Scotti, G. Conte, M. C. Rossi, *Electronics Letters* **1999**, *35*, 1768.

[227] E. Munoz Merino, E. Monroy, F. Calle, M. A. Sanchez, E. Calleja, F. Omnes, P. J. L. Gibart, F. Jaque, I. Aguirre de Carcer, in *Photodetectors: Materials and Devices IV*, **1999**, pp. 200–210.

[228] A. Array, M. Razeghi, P. Kung, D. Walker, E. Monroy, M. Hamilton, *THE JOURNAL OF THE KOREAN PHYSICAL SOCIETY* **1999**, *34*, S234 –S243.

[229] B. Monemar, G. Pozina, *Progress in Quantum Electronics* **2000**, *24*, 239–290.

[230] H. Fabricius, T. Skettrup, P. Bisgaard, *Applied optics* **1986**, *25*, 2764.

[231] Y. Takahashi, M. Kanamori, A. Kondoh, H. Minoura, Y. Ohya, *Japanese Journal of Applied Physics Part 1-Regular Papers Short Notes & Review Papers* **1994**, *33*, 6611–6615.

[232] D. H. Zhang, *Journal of Physics D: Applied Physics* **1995**, *28*, 1273–1277.

[233] D. H. Zhang, *Materials Chemistry and Physics* **1996**, *45*, 248–252.

[234] L. Wu, F. Song, X. Fang, Z.-X. Guo, S. Liang, *Nanotechnology* **2010**, *21*, 475502.

[235] Y. Hu, Y. Liu, W. Li, M. Gao, X. Liang, Q. Li, L.-M. Peng, *Advanced Functional Materials* **2009**, *19*, 2380–2387.

[236] Y. H. Leung, Z. B. He, L. B. Luo, C. H. A. Tsang, N. B. Wong, W. J. Zhang, S. T. Lee, *Applied Physics Letters* **2010**, *96*, 053102.

[237] Z. Wang, X. Zhan, Y. Wang, S. Muhammad, Y. Huang, J. He, *Nanoscale* **2012**, *4*, 2678–84.

[238] S. S. Shinde, K. Y. Rajpure, *Journal of Alloys and Compounds* **2012**, *522*, 118–122.

[239] R. R. Prabhakar, N. Mathews, K. B. Jinesh, K. R. G. Karthik, S. S. Pramana, B. Varghese, C. H. Sow, S. Mhaisalkar, *Journal of Materials Chemistry* **2012**, *22*, 9678–9683.

[240] Y. B. Li, F. Della Valle, M. Simonnet, I. Yamada, J. J. Delaunay, *Nanotechnology* **2009**, *20*, 045501.

[241] S. Bai, W. W. Wu, Y. Qin, N. Y. Cui, D. J. Bayerl, X. D. Wang, *Advanced Functional Materials* **2011**, *21*, 4464–4469.

[242] Y. Liu, C. R. Gorla, S. Liang, N. Emanetoglu, Y. Lu, H. Shen, M. Wraback, *Journal of Electronic Materials* **2000**, *29*, 69–74.

[243] Z. Bi, X. Yang, J. Zhang, X. Bian, D. Wang, X. Zhang, X. Hou, *Journal of Electronic Materials* **2008**, *38*, 609–612.

[244] L. J. Mandalapu, F. Xiu, Z. Yang, J. L. Liu, *Solid-State Electronics* **2007**, *51*, 1014–1017.

[245] J. Sun, F.-J. Liu, H.-Q. Huang, J.-W. Zhao, Z.-F. Hu, X.-Q. Zhang, Y.-S. Wang, *Applied Surface Science* **2010**, *257*, 921–924.

[246] Y. S. Choi, J. Y. Lee, S. Im, S. J. Lee, *Journal of Vacuum Science & Technology B* **2002**, *20*, 2384–2387.

[247] H. Ohta, M. Hirano, K. Nakahara, H. Maruta, T. Tanabe, M. Kamiya, T. Kamiya, H. Hosono, *Applied Physics Letters* **2003**, *83*, 1029–1031.

[248] L. A. Kosyachenko, G. V. Lashkarev, V. M. Sklyarchuk, A. I. Ievtushenko, O. F. Sklyarchuk, V. I. Lazorenko, A. Ulyashin, *physica status solidi (a)* **2010**, *207*, 1972–1977.

[249] H. Zhu, C. X. Shan, L. K. Wang, J. Zheng, J. Y. Zhang, B. Yao, D. Z. Shen, *The Journal of Physical Chemistry C* **2010**, *114*, 7169–7172.

[250] Y. Q. Bie, Z. M. Liao, H. Z. Zhang, G. R. Li, Y. Ye, Y. B. Zhou, J. Xu, Z. X. Qin, L. Dai, D. P. Yu, *Advanced Materials* **2011**, *23*, 649–653.

[251] H. D. Cho, A. S. Zakirov, S. U. Yuldashev, C. W. Ahn, Y. K. Yeo, T. W. Kang, *Nanotechnology* **2012**, *23*.

[252] Z. Y. Zhan, L. X. Zheng, Y. Z. Pan, G. Z. Sun, L. Li, *Journal of Materials Chemistry* **2012**, *22*, 2589–2595.

[253] L. Mandal, M. Deo, A. Yengantiwar, A. Banpurkar, J. Jog, S. Ogale, *Advanced Materials* **2012**, *24*, 3686–3691.

[254] W. Jin, Y. Ye, L. Gan, B. Yu, P. Wu, Y. Dai, H. Meng, X. Guo, L. Dai, *Journal of Materials Chemistry* **2012**, *22*, 2863.

[255] Q. Yang, Y. Liu, Z. T. Li, Z. Y. Yang, X. Wang, Z. L. Wang, *Angewandte Chemie-International Edition* **2012**, *51*, 6443–6446.

[256] Y. Zhou, C. Ahyi, C.-C. Tin, J. Williams, M. Park, D.-J. Kim, A.-J. Cheng, D. Wang, A. Hanser, E. A. Preble, N. M. Williams, K. Evans, *Applied Physics Letters* **2007**, *90*, 121118.

[257] D. Wu, Y. Jiang, Y. Zhang, Y. Yu, Z. Zhu, X. Lan, F. Li, C. Wu, L. Wang, L. Luo, *Journal of Materials Chemistry* **2012**, *22*, 23272.

[258] H. Zhu, C. X. Shan, B. Yao, B. H. Li, J. Y. Zhang, D. X. Zhao, D. Z. Shen, X. W. Fan, *Journal of Physical Chemistry C* **2008**, *112*, 20546–20548.

[259] S. X. Yang, J. Gong, Y. L. Deng, *Journal of Materials Chemistry* **2012**, *22*, 13899–13902.

[260] A. L. Ankudinov, J. J. Rehr, S. D. Conradson, *Physical Review B* **1998**, *58*, 7565–7576.

[261] G. Amin, M. H. Asif, A. Zainelabdin, S. Zaman, O. Nur, M. Willander, *Journal of Nanomaterials* **2011**, *2011*, 269692.

[262] J. Joo, B. Y. Chow, M. Prakash, E. S. Boyden, J. M. Jacobson, *Nature materials* **2011**, *10*, 596–601.

[263] L. Lin, H. Watanabe, M. Fuji, T. Endo, S. Yamashita, M. Takahashi, *Journal of the American Ceramic Society* **2009**, *92*, S165–S167.

[264] G. A. Carlsson, C. A. Carlsson, *The International Journal of Applied Radiation and Isotopes* **1982**, *33*, 953–965.

[265] C. F. Klingshirn, B. K. Meyer, A. Waag, A. Hoffmann, J. Geurts, *Springer Series in Materials Science 120* **2010**, DOI 10.1007/978-3-642-10577-7.

[266] A. F. Kohan, G. Ceder, D. Morgan, C. G. Van de Walle, *Physical Review B* **2000**, *61*, 15019–15027.

[267] D. Look, G. Farlow, P. Reunchan, S. Limpijumnong, S. Zhang, K. Nordlund, *Physical Review Letters* **2005**, *95*, 225502–.

[268] K. Vanheusden, W. L. Warren, C. H. Seager, D. R. Tallant, J. A. Voigt, B. E. Gnade, *Journal of Applied Physics* **1996**, *79*, 7983–7990.

[269] C. Patterson, *Physical Review B* **2006**, *74*, 144432.

[270] M. D. McCluskey, S. J. Jokela, *Journal of Applied Physics* **2009**, *106*, 071101.

[271] A. B. Djurišić, Y. H. Leung, K. H. Tam, Y. F. Hsu, L. Ding, W. K. Ge, Y. C. Zhong, K. S. Wong, W. K. Chan, H. L. Tam, K. W. Cheah, W. M. Kwok, D. L. Phillips, *Nanotechnology* **2007**, *18*, 095702.

[272] S.-W. Han, H.-J. Yoo, S. J. An, J. Yoo, G.-C. Yi, *Applied Physics Letters* **2005**, *86*, 021917.

[273] S.-H. Park, S.-Y. Seo, S.-H. Kim, S.-W. Han, *Applied Physics Letters* **2006**, *88*, 251903.

[274] E.-S. Jeong, H.-J. Yu, S.-W. Han, S. J. An, J. Yoo, Y.-J. Kim, and Gyu-Chul Yi, *Journal of Korean Physical Society* **2008**, *53*, 461–465.

[275] Z. H. Wu, Y. X. Zhou, X. Y. Zhang, S. Q. Wei, D. L. Chen, *Applied Physics Letters* **2004**, *84*, 4442–4444.

[276] I. Mora-Sero, S. Gimenez, F. Fabregat-Santiago, E. Azaceta, R. Tena-Zaera, J. Bisquert, *Physical Chemistry Chemical Physics* **2011**, *13*, 7131–7138.

[277] B. O'Regan, D. T. Schwartz, S. M. Zakeeruddin, M. Gratzel, *Advanced Materials* **2000**, *12*, 1263.

[278] E. Azaceta, S. Chavhan, P. Rossi, M. Paderi, S. Fantini, M. Ungureanu, O. Miguel, H.-J. Grande, R. Tena-Zaera, *Electrochimica Acta* **2012**, *71*, 39–43.

[279] J. Briscoe, D. E. Gallardo, S. Hatch, V. Lesnyak, N. Gaponik, S. Dunn, *Journal of Materials Chemistry* **2011**, *21*, 2517–2523.

[280] Keithley 2400 User's Manual (http://www.keithley.co.uk/data?asset=12843)

[281] X. Li, C. Gao, H. Duan, B. Lu, Y. Wang, L. Chen, Z. Zhang, X. Pan, E. Xie, *Small* **2012**, DOI 10.1002/smll.201202408.

[282] S. M. Hatch, J. Briscoe, S. Dunn, *Advanced Materials* **2013**, *25*, 867–871.